

ABSTRACT

Topology Optimization of Weakly Coupled Thermomechanical Systems for Additive Manufacturing

Jackson S. Ramsey, M.S.M.E.

Mentor: Douglas E. Smith, Ph.D.

Topology optimization is a design optimization method that generates structures with complex geometries that are ideally suited for additive manufacturing. Most additively manufactured structures have anisotropic material properties, especially those composed of fiber-filled polymers. In addition, residual thermal stresses arise from nonisothermal cooling processes during manufacturing. This thesis presents a new topology optimization-based approach that incorporates both material anisotropy and weakly coupled thermomechanical loading into the design computations. Here, design derivatives are evaluated using the adjoint variable method specifically for the weakly coupled thermomechanical system. Two separate update schemes, the optimality criterion-based update scheme and the globally convergent method of moving asymptotes, minimize the compliance or strain energy within the design space over material density and anisotropic orientation. The relative performance of the objective functions and update schemes are compared to determine how to best optimize these structures.

Topology Optimization of Weakly Coupled Thermomechanical Systems for Additive
Manufacturing

by

Jackson S. Ramsey, B.S.M.E.

A Thesis

Approved by the Department of Mechanical Engineering

Paul Ro, Ph.D., Chairperson

Submitted to the Graduate Faculty of
Baylor University in Partial Fulfillment of the
Requirements for the Degree
of
Master of Science in Mechanical Engineering

Approved by the Thesis Committee

Douglas E. Smith, Ph.D., Chairperson

David A. Jack, Ph.D.

Enrique P. Blair, Ph.D.

Accepted by the Graduate School

December 2019

J. Larry Lyon, Ph.D., Dean

Copyright © 2019 by Jackson S. Ramsey

All rights reserved

TABLE OF CONTENTS

LIST OF FIGURES	vi
LIST OF TABLES	ix
ACKNOWLEDGMENTS	x
DEDICATION	xi
CHAPTER ONE	1
Introduction	1
1.1 Additive Manufacturing and Topology Optimization	1
1.2 Objective	2
1.3 Overview of Contents	3
CHAPTER TWO	6
Literature Review	6
2.1 Introduction	6
2.2 Topology Optimization	19
2.3 Topology Optimization for Additively Manufactured Structures	34
CHAPTER THREE	37
Methods	37
3.1 Design Space and Optimization Function	37
3.2 Design Sensitivity via the Adjoint Method	51
3.3 Optimality Criteria Method	54
3.4 The Globally Convergent Method of Moving Asymptotes	55
3.5 Issues with the Density Method	59
3.6 Anisotropic Material Model	64
3.7 Weakly Coupled Thermomechanical Systems	70
3.8 Strain Energy Optimization	78
CHAPTER FOUR	83
Results	83
4.1 Overview	83
4.2 Problem Setup	84
4.3 Weakly Coupled Orthotropic Thermomechanical System	93
4.4 Comparison of Performance	100
4.5 Effects of Increased Thermal Loading	104
4.6 Convergence Issues	109
CHAPTER FIVE	120

Conclusions.....	120
5.1 Summary of Progress.....	120
5.2 Production of Structures	122
5.3 Future Work.....	123
APPENDIX	128
Code Used.....	128
BIBLIOGRAPHY.....	142

LIST OF FIGURES

Figure 2.1: Powder Bed Fusion Process	7
Figure 2.2: Trends in Metal AM Sales.....	8
Figure 2.3: Diagram of Fused-Filament Fabrication Process	10
Figure 2.4: Possible Bead Deposition Patterns	11
Figure 2.5: Tensile Strength of Various Print Patterns for ABS Plastic Compared to Injection Molded Parts	12
Figure 2.6: Image of Beads of FFF-Produced Part in a 0-90 Orientation with Air Gaps Exaggerated.....	13
Figure 2.7: Diagram of Common Warping Due to Thermal Stresses.....	14
Figure 2.8: Image of Cracking Due to Thermal stress in a Titanium Powder-Bed Fusion Part	14
Figure 2.9: Big-Area Additive Manufacturing Printer at Oak Ridge National..... Laboratory	15
Figure 2.10: Comparison of Energy Intensity of Various Manufacturing Methods.....	16
Figure 2.11: Tensile Strength and Modulus of Parts with Varying Carbon Fiber Content and Manufacturing Method	18
Figure 2.12: Heat Fin Optimized for Thermal Compliance.....	26
Figure 2.13: Optimized Print Direction	31
Figure 2.14: Discrete Material Optimization for Composite Lamina.....	33
Figure 2.15: Continuous Fiber Angle Optimization	33
Figure 3.1: Example Two-Dimensional Design Domain	44
Figure 3.2: Density Visualization	47
Figure 3.3: Checkerboarding in Cantilever Beam	60

Figure 3.4: Different Initial Density Distributions and Resulting Final Structures	63
Figure 3.5: Example Element Orientations	69
Figure 4.1: Design Domain of MBB Beam	84
Figure 4.2: Final Topology of Isotropic MBB Beam Under Pure Mechanical Loading ... by OC Method	86
Figure 4.3: Convergence History of Compliance Optimization of Isotropic..... Mechanical MBB Beam Using OC Method	87
Figure 4.4: Final Topology of Isotropic MBB Beam Under Pure Mechanical Loading ... by GCMMA Method	88
Figure 4.5: Convergence History of Compliance Optimization of Isotropic..... Mechanical MBB Beam Using GCMMA Method	89
Figure 4.6: Final Topology of Anisotropic MBB Beam Under Pure Mechanical..... Loading by OC Method	90
Figure 4.7: Convergence History of Compliance Optimization of Anisotropic	91
Mechanical MBB Beam Using OC Method	
Figure 4.8: Final Topology of Anisotropic MBB Beam Under Pure Mechanical..... Loading by GCMMA Method	92
Figure 4.9: Convergence History of Compliance Optimization of Anisotropic	92
Mechanical MBB Beam Using GCMMA Method	
Figure 4.10: Final Topology of Orthotropic Weakly Coupled Model, Compliance	94
Optimized with the Optimality Criteria Method	
Figure 4.10b: Region of Fractional Density Present in Figure 4.10	95
Figure 4.11: Compliance Convergence History of Orthotropic Weakly Coupled..... Model, Optimality Criterion Method	95
Figure 4.12: Final Topology of Orthotropic Weakly Coupled Model, Strain Energy..... Optimized via the Optimality Criteria Method	96
Figure 4.13: Strain Energy Convergence History of Orthotropic Weakly Coupled..... Model, Optimality Criterion Method	97
Figure 4.14: Final Topology of Orthotropic Weakly Coupled Model, Compliance	98
Optimized via the GCMMA Method	

Figure 4.15: Compliance Convergence History of Orthotropic Weakly Coupled.....98 Model, GCMMA Method	98
Figure 4.16: Final Topology of Orthotropic Weakly Coupled Model, Strain Energy.....99 Optimized via the GCMMA Method	99
Figure 4.17: Strain Energy Convergence of Orthotropic Weakly Coupled Model,100 GCMMA Method	100
Figure 4.18: Final Topology of Isotropic Compliance Optimization via the OC101 Method	101
Figure 4.19: Final Topology of Isotropic Compliance Optimization via the GCMMA..102 Method	102
Figure 4.20: Final Topology of Isotropic Strain Energy Optimization via the OC102 Method	102
Figure 4.21: Final Topology of Isotropic Strain Energy Optimization via the GCMMA Method103	103
Figure 4. 22a: Final Strain Energy – Optimized Topologies as Thermal Loading.. 104-105 Increases. Thermal Load Values are 0 W , 10 W , 30 W , and 50 W	104-105
Figure 4.22b: Final Compliance – Minimized Topologies as Thermal Loading.....106 Increases. Thermal Load Values are 0 W , 10 W , 30 W , and 50 W	106
Figure 4.23: Final Topologies for Various Sensitivity-Shifting Functions. The111 Graphs in a-d Correspond with Shifting Functions 1-4 Respectively	111
Figure 4.24: Final Topologies for Various Thermal Penalty Values, $p_m = 3$ 113-114 The Graphs in a-e Correspond with $p_{th} = 1$ to $p_{th} = 5$ Respectively	113-114
Figure 4. 25: Converged Topologies for $r_{min} \in \{1,2,5,10,20\}$ Pixels, Respectively,.....118 from Top to Bottom	118
Figure 4.26: Final Topologies for Increasing Mesh Refinement119	119
Figure 5.1: Proof-of-Concept Part Production Process.....122	122

LIST OF TABLES

Table 4.1: Constants for GCMMA Algorithm.....	87
Table 4.2: Optimization Performance.....	100
Table 4.3: Optimization Performance for Isotropic Material	103
Table 4.4: Performance of Compliance and Strain Energy-Optimized Structures	107
Table 4.5: Thermal Contribution to Compliance in Various Tests.....	108

ACKNOWLEDGMENTS

I am thankful for the guidance of my advisor Dr. Douglas E. Smith, the assistance of Dr. Jack, and the support of my fellow graduate students in the completion of this work.

DEDICATION

To my wife Hannah

whose love and support were integral to my perseverance in graduate school

CHAPTER ONE

Introduction

1.1 Additive Manufacturing and Topology Optimization

The recent development of additive manufacturing has redefined what is possible to create. In its early years the technology was used primarily to accelerate the prototyping process, but as the technology has matured it is increasingly being used for end-use parts. The incredible amount of design freedom allows for extremely lightweight, complex, and strong parts to be produced. However, design methods have not yet caught up to the near-arbitrary complexity allowed in additively manufactured structures.

Topology optimization is a group of structural optimization methods that seek to determine the best placement of material by optimizing an important response of the structure under consideration. The structures produced often mimic natural designs like plant root or spiderweb structures. The resultant structures are complex enough that, until the development of additive manufacturing, design solutions were often difficult or impossible to manufacture without significant design alteration in post-processing. Thus, topology-optimized parts have often been presented in research as computational models without producing physical parts for testing.

Additive manufacturing and topology optimization are two technologies that complement each other. Topology optimization is a design method that fully utilizes the possibilities in a design space and is not constrained by traditional design and manufacturing procedures. Additive manufacturing is a viable approach capable of

producing these parts. Uniting these technologies will allow for ideal parts to be created for objectives such as stiffness, lightweighting, thermal efficiency, and many other parameters. In order to develop a topology optimization approach that fully models the additive manufacturing process, several advancements must be made from the current state of the art methods.

1.2 Objective

The existing body of work on topology optimization addresses some of the factors present in additive manufacturing, however, many factors appear among various research publications which do not capture the full complexity needed to model and optimize an additively manufactured structure. For example, topology optimization under thermal loading has been considered, but prior work either assumes that the temperature field is given, or thermal loading is considered separate from the mechanical loading. Further, to the best of our knowledge, no transient thermal loading has been considered for optimization, which would be necessary to represent the cooling process in many of the common additive manufacturing methods such as fused-filament fabrication and selective laser sintering. In addition, the material properties in additively manufactured parts are often highly anisotropic and vary throughout the part, with the material properties dependent on the method of material deposition or extrusion. Topology optimization for anisotropic materials has been performed, but the models have been limited to systems including only mechanical loading.

This work seeks to model additive manufacturing in topology optimization by unifying several works that model partial elements of the additive manufacturing process and to advance the work one step closer to fully capturing the additive manufacturing

method. The research presented here considers weakly coupled thermomechanical systems, where a design-dependent temperature field generates thermal stresses that influence the mechanical equilibrium, is defined with a material that is orthotropic in both the thermal and mechanical analyses and is spatially varying. Two topology optimization algorithms are considered where we optimize the material density and orientation, and the relative performance of the algorithms is assessed. Two objective functions are considered for stiffness minimization, as in weakly coupled thermomechanical systems a stiffness inverse can be formulated as compliance or strain energy. The results presented here show the viability of optimizing in the model considered and offer recommendations for future work to more accurately optimize the structure of additively manufactured parts.

1.3 Overview of Contents

The current state of the additive manufacturing industry and research is discussed, along with an overview of different structural optimization methods, in Chapter two. The need for a new design approach is explained by examining many common additive manufacturing processes and noting the effect that the production process has on the performance of the part. Existing topology optimization methods are presented to provide an outline of currently available methods, their capabilities and existing applications, and their respective strengths and weaknesses.

Following this overview, the model used for the optimization problem considered in this thesis is developed in Chapter three. First, compliance optimization of a mechanical system is presented. Compliance minimization is commonly used and has been well-established in the literature. Conduction heat transfer in structures is then

introduced, and the coupling between thermal and mechanical analyses is explored. Anisotropic material behavior is also considered, and an additional set of design variables is introduced to capture the orientation of the material's preferred direction. The design sensitivities are determined for this system, and both the optimality criterion and globally convergent method of moving asymptotes are discussed as possible optimization methods. Additionally, another objective function, strain energy, is proposed as an alternate objective function as it also behaves as a stiffness inverse.

In Chapter four the optimizations are conducted for a sample design domain. Several optimizations are performed for using either compliance or strain energy as the objective function, and the performance of the two optimization algorithms described above is considered. A series of tests with increasing thermal loading is performed to determine how the thermal effects affect the final topology for each objective function.

Optimal results obtained with each of the objective functions mentioned above are compared and recommendations on which one is best suited to the problem posed here are made. Optimizations with varying amounts of thermal loading are discussed, which offers insight into how various objective functions affect the resultant structures. Also, the optimization algorithms are compared in a similar manner to determine which are more effective at optimizing the structures. Their relative advantages are discussed and design problems in which each would perform well are determined.

Chapter five then summarizes the conclusions of this research and recommends future steps. While no physical testing of parts is done in this work, Chapter five outlines the necessary limitations of physically testing the material model used in this work and a

means of producing proof-of-concept parts. The limitations of the method used here and future work to improve it are given.

CHAPTER TWO

Literature Review

2.1 Introduction

The development of additive manufacturing has opened new design possibilities. The research presented in this thesis focuses specifically on additive manufacturing, as the rapid development of the method has already drastically affected manufacturing and will continue to do so as the technique matures.

2.1.1 Overview and History

For most of its history, additive manufacturing (AM) has been used as a rapid prototyping method. It encompasses a family of techniques based on the CNC machining systems developed beginning in the 1960s [1]. Typical computer-aided machining involves beginning with a block of material larger than the desired part and then removing material with a drill bit, water jet, laser, or similar cutting tool to reach the desired shape. Additive manufacturing, in contrast, builds a part by adding material during the design process. Less material is generally used in AM compared to traditional processes because there is minimal material removal. In addition, there is greater design freedom in AM because the material at each point in the part can be individually placed.

The AM method began with stereolithography printing in 1987 that solidified liquid polymer into a specific pattern by using directed ultraviolet radiation. Since then, AM has expanded to seven main techniques, which include binder jetting, direct energy deposition, material extrusion, material jetting, powder bed fusion, sheet lamination, and

vat photopolymerization [2]. While the first AM technique was a form of vat photopolymerization, material extrusion has become widespread as a cost-effective and efficient AM method. One variety, known as Fused-Filament Fabrication (FFF) or Fused Deposition Modeling (FDM), employs thermoplastic filament that is melted in an extruder and deposited with a CNC-type gantry system. FDM has been popularized in desktop printers that are inexpensive enough for hobbyists and students. Fused-filament fabricated parts have traditionally been poorly suited to high-precision or high-loading applications but are often used in the prototyping process. Recent developments such as short carbon fiber inclusions to form a polymer composite and large-area printers are challenging the limitations of FDM by drastically increasing the strength and size of AM parts [3]. Figure 2.1 illustrates another AM method, powder bed fusion.

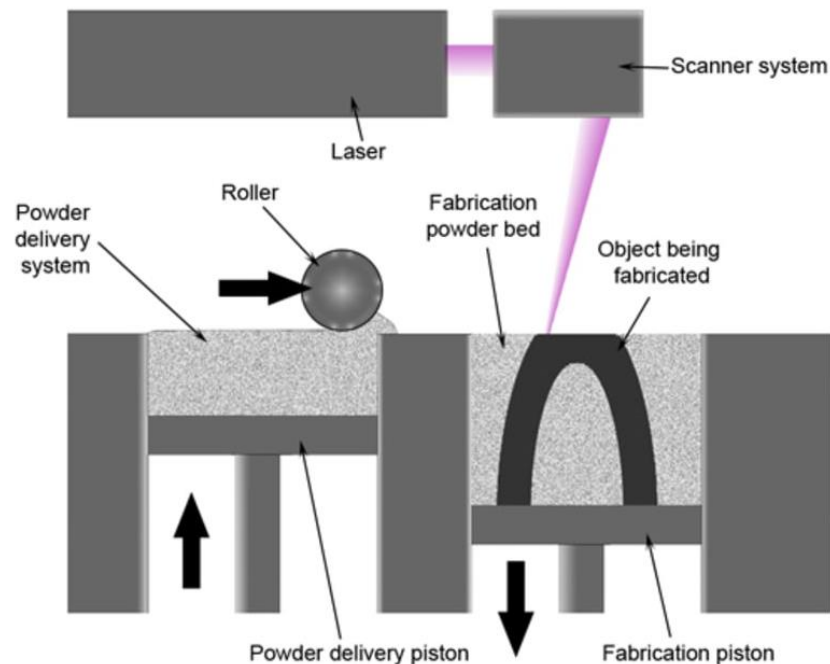


Figure 2.1: Powder Bed Fusion Process [4]

Powder bed fusion methods, such as selective laser sintering, can produce parts with extremely high geometric precision using high-performance materials such as steel and titanium. Metal AM systems can be significantly more expensive, but their parts are well-suited for end-use applications in industries like aerospace where high strength-to-weight ratios are required. Metal AM devices have experienced exponential growth in sales as they are increasingly adopted for production in industry [5], as seen in Figure 2.2.

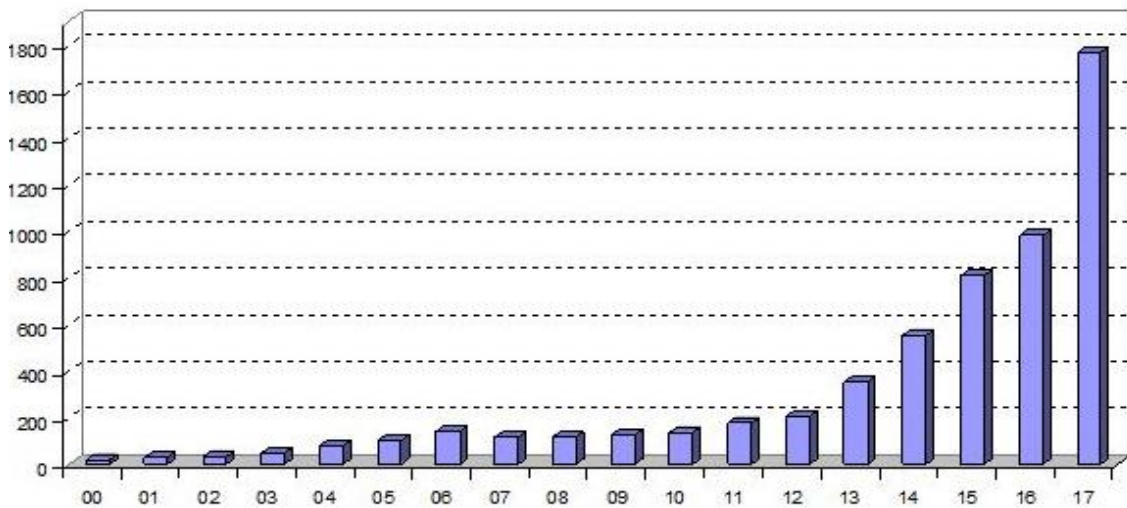


Figure 2.2: Trends in Metal AM Sales [5]

The significant increase in sales visible in Figure 2.2 is likely due to widespread awareness of the benefits of AM described above, namely fast affordable production of arbitrarily complex geometries for parts that are mechanically strong and geometrically precise enough for production.

The research in this thesis is primarily aimed at fused-deposition modeling where high temperature material is deposited, and the resulting material properties are anisotropic. While much of the AM influence on the topology optimization approach presented here is driven by FDM, the design approach in the following chapters is not

limited to FDM and may well serve the design of parts produced with other AM technologies. For example, many aspects of the findings apply to selective laser sintering and other techniques. Current literature is somewhat limited with respect to the best way to use AM systems, as AM methods are just now becoming common industry. The work here seeks to advance our understanding of AM systems and offer recommendations on how to optimize part performance.

2.1.2 Fused Filament Fabrication

The most common fused-filament fabrication technique usually consists of a desktop-sized device containing a polymer extrusion system mounted on a three-dimensional gantry system. Material is supplied as a filament of thermoplastic polymer or polymer composite to an extruder that deposits material based on a given toolpath. The extruder forces the polymer filament through a heater to melt it and then deposits it onto a build platform through a nozzle. A standard FDM system has three axes of mobility, allowing material to be placed at any coordinate within the build volume to form the part. Some FDM systems allow the extruder to move in all three axes and fix the build platform. Other FDM devices allow the extruder to move only in directions parallel to the build plane and have the build plate raise and lower. Many permutations exist, but the build platform and extruder must have at least three axes of movement combined. Figure 2.3 shows one such system.

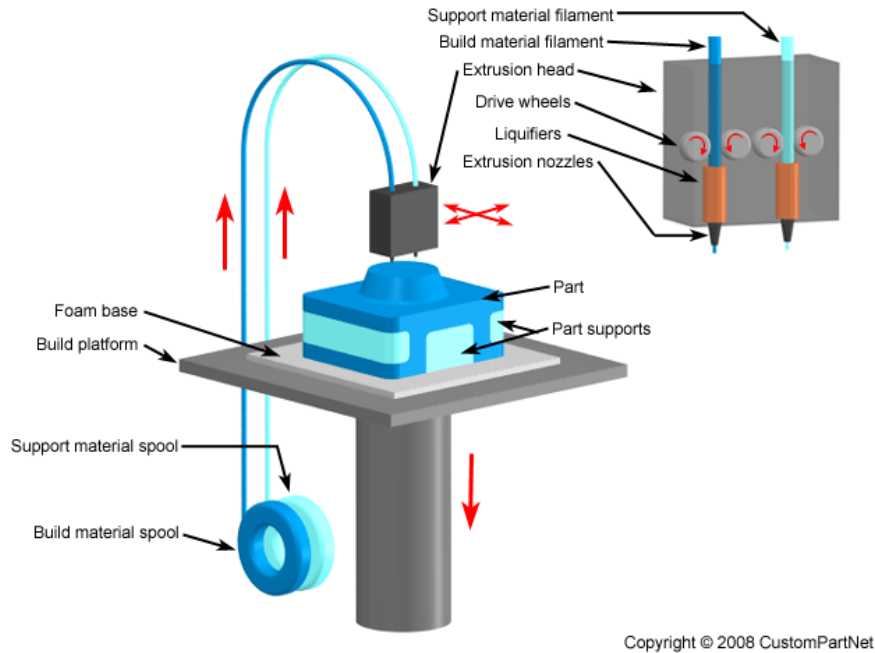


Figure 2.3: Diagram of Fused-Filament Fabrication Process [6]

The polymer is deposited in a molten state and allowed to cool to form a solid structure. In some cases, a support structure is needed underneath the printed part as it cools so that it does not collapse. Support can be made by extruding support patterns that are designed to support the main structure as it cools and then be removed once extrusion is complete. Some systems contain multiple extruders that deposit different material and can use a secondary material exclusively for the support, as pictured above. This can be a water-soluble polymer, allowing for easy removal of the supports without risking damage to the rest of the part.

2.1.2.1 Performance of additively manufactured structures. The polymer in fused-filament fabrication is deposited in a series of beads that make up the part. The beads are placed side-by-side, and both air gaps between the beads and reduced polymer bonding between the beads can weaken the part. The direction the beads are extruded can thus

affect the structural response of the part. Figure 2.4 shows different bead extrusion patterns.

The closeness of the beads also affects inter-bead bonding. A part can be made less dense by spacing the beads further apart and allowing air gaps at the expense of part strength. The tradeoff between density and strength and the ability to vary the bead spacing arbitrarily allows for much greater design freedom than in traditional manufacturing methods like injection molding, but parts with no bead spacing are still weaker than parts produced via injection molding and other means. Figure 2.5 shows how the strength of an extruded part varies with toolpath orientation.

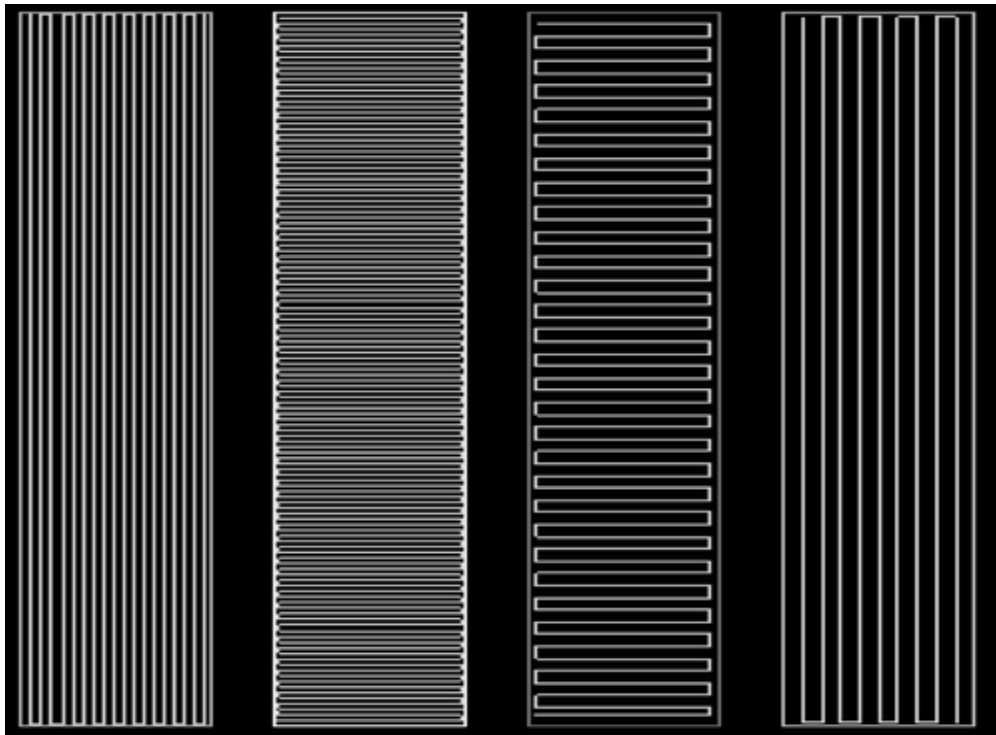


Figure 2.4: Possible Bead Deposition Patterns [7]

The bead direction can be changed with each layer to generate infill patterns that create parts with toolpath-dependent mechanical and thermal properties. The data

obtained from [7] in Figure 2.5 shows the tensile strength for various bead orientation patterns and compares these values to the tensile strength of an injection molded part. There is high variance in the strength of the AM part based on the orientation of the beads, but all AM parts perform worse than the injection molded part. Tensile strength ranged between 65-72% of the injection molded part, and compressive strength was 80-90% of the injection molded part.

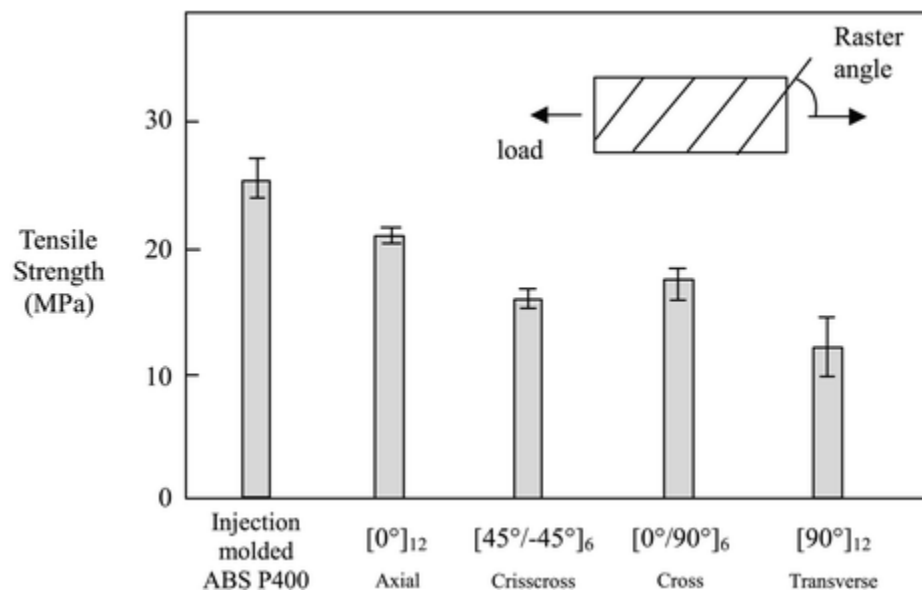


Figure 2.5: Tensile Strength of Various Print Patterns for ABS Plastic Compared to Injection Molded Parts [7]

2.1.2.2 Manufacturing challenges: anisotropy. The anisotropy noted above is problematic beyond the AM parts' failure to perform as well as an injection molded part. Polymer chains tend to align in the direction of the bead [3], which increases the bead's stiffness and tensile strength in that direction. In addition, air gaps between adjacent beads weaken the part's strength in the directions perpendicular to the bead, and if beads cool below the polymer's glass transition temperature, they form weaker bonds to

adjacent beads. Layers are usually dispensed sequentially, so the weaker bonding occurs most between successive layers. Thus, parts produced by fused-filament fabrication are often strongest and stiffest in the direction of the beads, weaker and more compliant in the direction parallel to the build plate and perpendicular to the beads, and weakest and least stiff in the direction perpendicular to build plane. Figure 2.6 shows the air gaps between beads in a printed part that exaggerates the gaps for visibility.

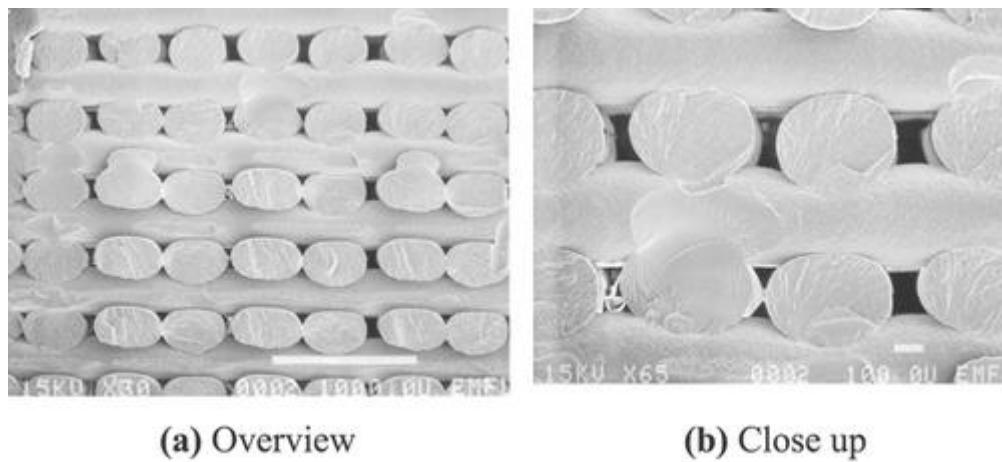


Figure 2.6: Image of Beads of FFF-Produced Part in a 0-90 Orientation with Air Gaps Exaggerated [8]

2.1.2.3 Manufacturing challenges: thermal stresses. Additionally, as the deposited polymer cools from melt to the environment temperature, it contracts based on its coefficient of thermal expansion. The cooling process can generate thermal stresses within the part that cause deformation or premature failure of the part. In small-scale fused-filament fabrication, the thermal deformation commonly causes the corners of a print to peel upward, as depicted in Figure 2.7.

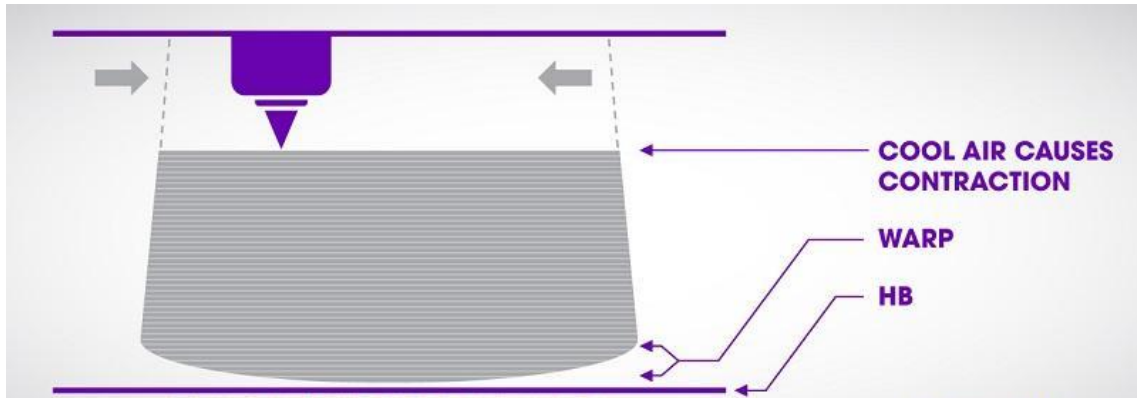


Figure 2.7: Diagram of Common Warping Due to Thermal Stresses [9]

Thermal stress is present in other AM methods as well. Most metal AM methods involve the melting of the metal involved, and as metals have higher melting temperatures than polymers, parts produced with methods like powder-bed fusion can experience extremely high thermal stresses. Such stress is sufficient to crack the part in some cases, as seen in Figure 2.8. Methods that involve a polymer curing or a material drying have analogous stresses as the material contracts due to curing or drying stresses.



Figure 2.8: Image of Cracking Due to Thermal stress in a Titanium Powder-Bed Fusion Part [4]

The thermal stresses present in parts produced using smaller FDM systems can be lessened by using a heated build plate and insulating the print volume to provide for slower cooling. However, researchers have recently developed large FDM printers, and the thermal effects in those systems are more challenging to mitigate.

2.1.2.4 Big area additive manufacturing. Oak Ridge National Laboratory partnered with Cincinnati, Inc. (Cincinnati, OH, USA) to create a large-scale polymer deposition system with a build volume of 20' x 8' x 6'. The large-scale extruder and print setup is shown in Figure 2.9. The large scale printer shown in Figure 2.9 has been used to produce polymer composite parts such as an excavator cab, molds for fiberglass boat hulls, molds for wind turbine blades, a submarine hull, and the chassis and shell of a Shelby Cobra [10]. The capability to rapidly produce large structures has opened an entirely new set of applications for FDM.

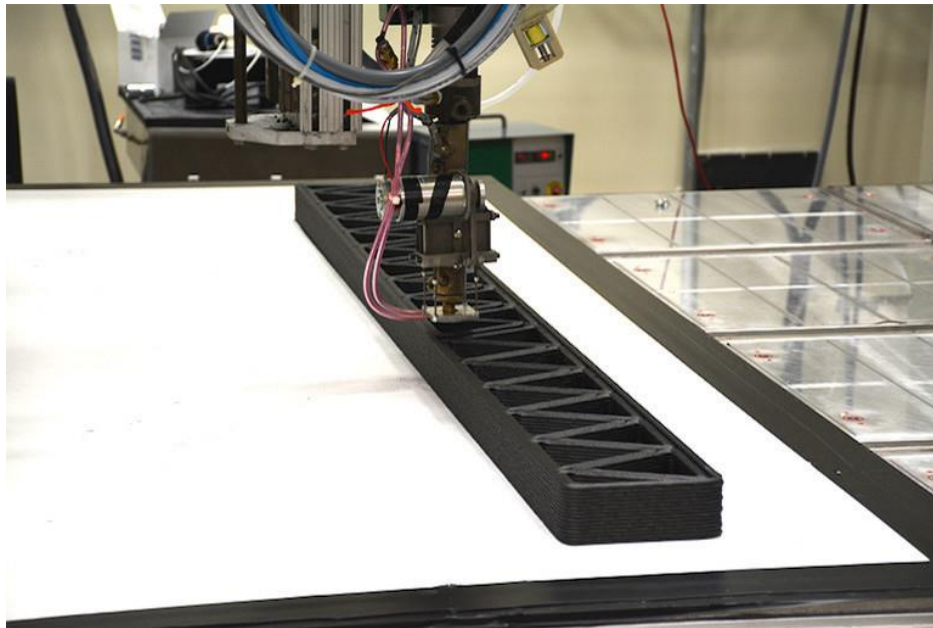


Figure 2.9: Big-Area Additive Manufacturing Printer at Oak Ridge National Laboratory [11]

The large-scale polymer deposition printer uses carbon fiber-filled plastic pellets, which are melted and deposited with a single-screw extruder instead of the filament system used by small scale FFF devices. The screw extrusion method allows for a much higher print rate. The deposited material is also stiff enough that it can be used to build tooling in hours that traditionally can take weeks to manufacture [11]. There is opportunity to produce large, high-strength parts with large-scale polymer deposition much more quickly and more cost-effectively than traditional methods. Figure 2.10 compares the energy necessary for big-area additive manufacturing to other forms of manufacturing.

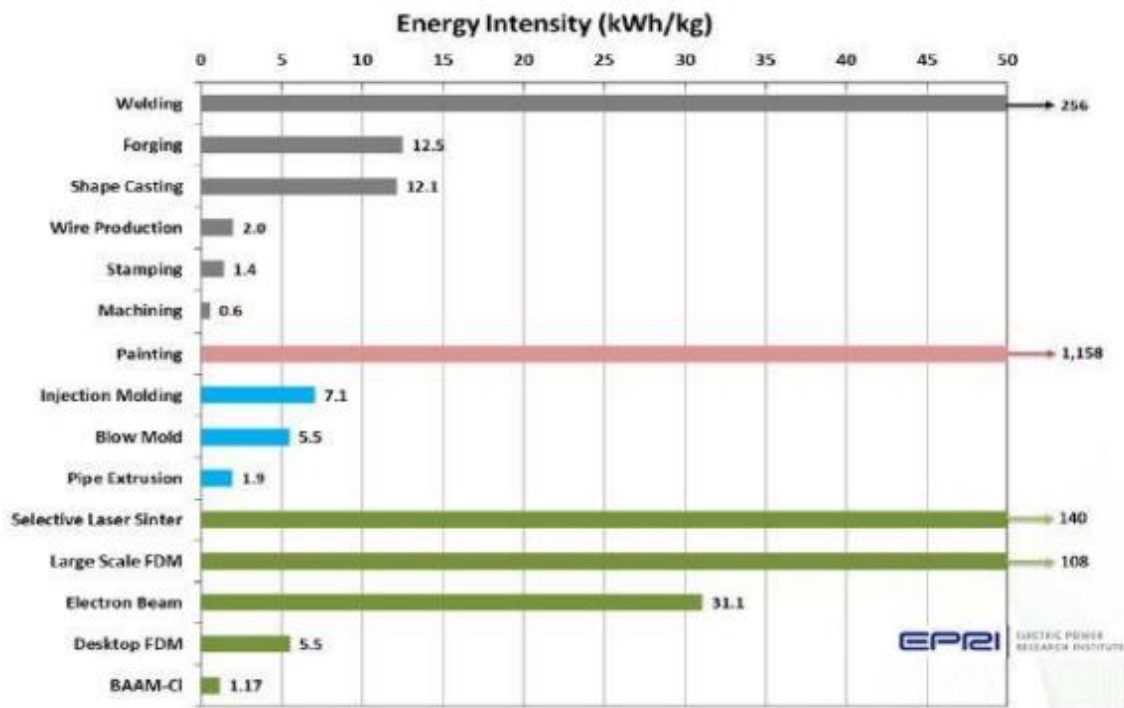


Figure 2.10: Comparison of Energy Intensity of Various Manufacturing Methods [12]

In the comparison above, Oak Ridge National Laboratory [12] compared the energy necessary to produce parts with different manufacturing methods and found big-area additive manufacturing to be the second most energy efficient.

The thermal stresses experienced during printing can have more severe effects as the size of the print increases. For example, the first print of the Shelby Cobra failed due to cracks that resulted from the thermal stresses [11], and research at Oak Ridge National Laboratory has been done to model the thermal behavior during manufacturing in an attempt to minimize the thermal stress [13], [14]. A cooling model has been proposed by Compton et. al. [14] for one-dimensional cooling of large-scale polymer deposition but modeling two- or three-dimensional cooling has not yet been done.

2.1.2.5 Fiber reinforcement. One method to decrease the effect of thermal stresses while improving mechanical performance is to add other materials to the polymer. Several types of materials have been considered to form a polymer composite for AM, including elastomers like titanium dioxide, plant fibers, and carbon and glass fibers [15]. The carbon fibers show the highest increase in material strength and stiffness [15], where the length of the fiber and the fiber volume fraction affect the performance of the part. Figure 2.11 from [16] shows how material properties change as the amount of fiber added increases.

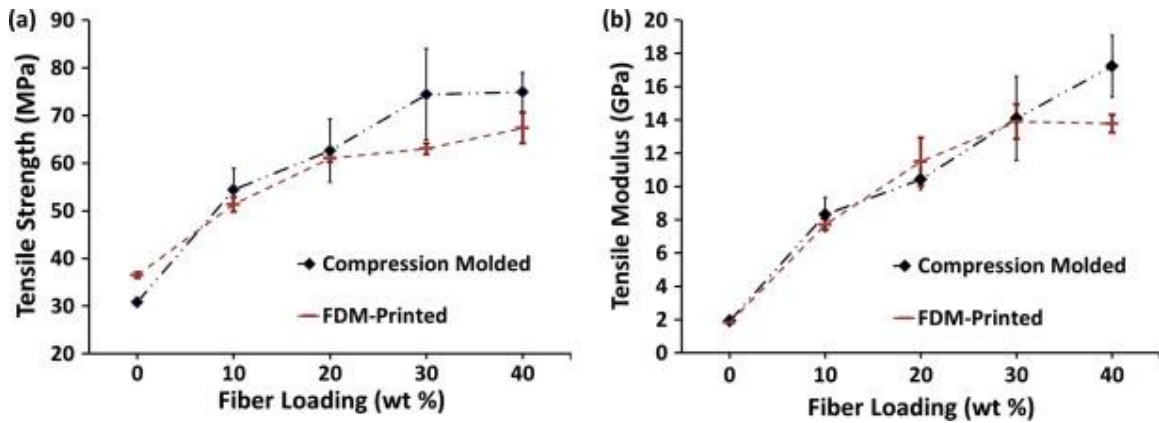


Figure 2.11: Tensile Strength and Modulus of Parts with Varying Carbon Fiber Content and Manufacturing Method [16]

Results of a parametric study of print parameters in [16] determined that increased carbon fiber weight percentage can significantly increase tensile strength and modulus. The strength of AM-produced carbon fiber-reinforced acrylonitrile butadiene styrene (ABS) can approach that of aerospace-grade aluminum [17]. Another study found an increase of 115% in tensile strength and a 700% increase in modulus in the direction of print [16] for carbon fiber-reinforced ABS parts compared to pure ABS parts. Longer fibers tend to increase the strength and stiffness parameters more than short fibers [18], but the fibers are broken and shortened by the extrusion process, limiting the effect that fiber inclusions can have on the final part properties. Continuous carbon fibers typically perform better than short chopped fibers, with one study finding an increase in the elastic modulus by a factor of 40 for continuous carbon fiber-reinforced nylon [19].

Short chopped carbon fibers tend to align in the direction of extrusion, increasing material strength, stiffness, and thermal conductivity and decreasing the coefficient of thermal expansion primarily in that direction [16]. Modeling of the extrusion process indicates that 60-66% of short chopped fibers are aligned in the extrusion direction [20],

and continuous fibers are completely aligned. The alignment increases the material anisotropy present in FDM parts. Some research in ABS with short glass fibers indicates that printed parts, while still stronger in the extrusion direction than pure ABS parts, are weaker perpendicular to the beads than pure ABS [21]. It is worth noting that the reduced die swell that results from using short carbon fiber-filled polymer can decrease the void between beads, which in general can increase bonding between beads.

In summary, high-strength high-volume parts can be created for a variety of new application using fiber-reinforced thermoplastics in big-area polymer composite deposition printers. Parts produced with such printers experience significant thermal stresses and anisotropy due to the manufacturing process, which need to be considered in part design. We next examine the steps that have been made to consider those factors in topology optimization algorithms.

2.2 Topology Optimization

2.2.1 Overview and History

Topology optimization is a form of structural optimization that determines the geometric layout of a part having a maximum or minimum performance measure such as stiffness. Several performance measures have been optimized, topology optimization has been performed using various general methods such as sequential linear programming and methods specifically designed for topology optimization, such as the homogenization method and the optimality criterion-based update scheme.

The first topology optimization method is often credited to Bendsoe and Kikuchi for their 1988 paper. The homogenization method maximized the stiffness of a two-

dimensional part under a fixed volume constraint. Other techniques were developed to solve the structural compliance minimization problem, such as the optimality criterion method [22] and the method of moving asymptotes [23]. Each of these methods have been applied to the basic structural compliance problem and have also been used in structures with multiple loading conditions, to optimize the performance of heat sinks, optimize the fundamental frequency of vibration, and create compliant mechanisms. Topology optimization has been used to develop parts with multiphase materials, anisotropic material properties, and piezoelectric properties. Bendsoe and Sigmund give numerous examples of these applications of topology optimization and more [24].

2.2.2 Compliance Optimization Methods

Minimizing the compliance of a structure was the first problem solved by topology optimization [25], and as compliance is analogous to the inverse of stiffness, it is extremely useful in maximizing the stiffness of a part. Each of the aforementioned methods used for topology optimization of other parameters were used to optimize compliance first, and compliance optimization is the most well-developed application [24].

Compliance minimization generates structures that are extremely stiff and lightweight, which is particularly useful in the aerospace and automotive industries as reductions in weight can affect the fuel efficiency of vehicles. Many commercial finite element programs include a topology optimization routine to minimize compliance, such as Ansys, Solidworks, and Abaqus [26]. The final topologies are typically geometrically complex, and while this presents manufacturing challenges, the designs are being used in production.

The algorithms used for topology optimization differ in formulation. Some include heuristic steps that are tailored specifically to compliance optimization, and other methods are more rigorously defined and easily applicable to other objective functions.

2.2.2.1 Homogenization approach. The homogenization method was the first method used for topology optimization, and while simpler methods have since been created, the groundwork of topology optimization was laid with this method. In the two-dimensional homogenization method, a design space is defined and discretized into finite elements where it is common to use identically sized square elements. Each square element is modeled with a rectangular void, with the side lengths defined by design variables. The topology optimization consists of resizing these voids to minimize the compliance of the structure. Successive work considered triangular voids, and allowed the rectangles to be rotated as a function of design [27], which made it possible to consider anisotropic materials. The method was expanded to shell structures [28], and three-dimensional structures [29].

The approach of considering the void shape within each element defines the microstructure of the part, and the final topologies are mesh-like structures. It was assumed that the void in an element represents an entire region of microscale voids instead of a single large void, which leads to difficulties in manufacturing the parts. Producing the actual parts has been done by creating large-scale cells with the same shape as the microscopic voids derived from the model [30], but this only approximates the model's design. New methods were considered to generate structures that could be manufactured without requiring such an approximation step.

2.2.2.2 Density penalization and the optimality criterion approach. Instead of treating each element as having a single void that could be individually designed, the density penalization method considers a design domain discretized into elements, which are also used for the finite element analysis [31]. Each element is assigned a density that varies between 0 and 1, where a density of 0 implies that the element is void and a density of 1 implies that the element is full of material. Fractional values for densities are permitted but are penalized in a way that encourages the densities to trend toward the upper or lower bounds. This method of design parametrization is used with the optimality criterion approach and the method of moving asymptotes [23]. In addition, element densities have been parameterized by higher level functions such as that found in the level-set approach [32]. The density method of topology optimization is further developed in Chapter three below.

The optimality criterion method is often used as a basis for topology optimization that solves a compliance minimization problem with a constraint on the amount of material used [22]. A constraint on volume provides an upper bound on the amount of material used, and the update scheme uses the Lagrange multiplier in a heuristic gradient-based approach that preserves the volume fraction constraint as an equality at every step. While the optimality criteria method used in topology optimization involves a heuristic parameter, it typically exhibits monotonic convergence to a final design where the densities approach either solid or void.

The optimality criterion approach has been applied in a concise Matlab code by Sigmund that is freely available and solves the two-dimensional topology optimization problem for planar structures [22]. The code used herein originated with that code. Other

versions of the code exist and have been applied to three-dimensional structures [33]. Similar formulations can be used to optimize thermal problems such as the effectiveness of a heat fin, indicating that the method, while heuristic, can be applied to more than just mechanical compliance minimization.

2.2.2.3 The method of moving asymptotes. While the optimality criterion method works well for compliance minimization, its common application to compliance minimization topology optimization must be extended when other objective functions are considered. The OC method must itself be modified to allow it to apply to more general models. The method of moving asymptotes is a general optimization scheme which has been applied to topology optimization [23]. When applied to topology optimization, the method of moving asymptotes utilizes the same density penalization method to parametrize the design of the structure but updates the densities in a gradient-based approach similar to sequential linear programming. One version of the method of moving asymptotes, the globally convergent method of moving asymptotes (GCMMA) was developed by Dr. Krister Svanberg [23], available as a Matlab code on request for research purposes. It has been shown to apply to many different optimization functions [34]. Unfortunately, the GCMMA algorithm can be more computationally expensive as it may require several function evaluations for each optimization iteration. In recent years it has replaced the optimality criterion approach in many topology optimization applications due to its versatility [23]. The GCMMA method is considered in Section 3 and its performance is compared to the optimality criterion method.

2.2.2.4 Bidirectional evolutionary structural optimization. The evolutionary structural optimization approaches take a simpler approach by basing the update method only on local objective function values, instead of computing the gradient. In standard applications of evolutionary structural optimization approaches, element densities are defined as above but are only permitted to hold discrete values of 0 or 1[35]. In Evolutionary Structural Optimization (ESO), the structure starts with all densities equal to 1 and successively removes the material from elements based on each element's contribution to the objective function [35]. The first use of ESO showed that it generates structures similar to the ones that the homogenization method produces, but it does not require a gradient, which drastically decreases the computational burden [35]. Adding a bidirectional aspect allows material to be added as well as subtracted, improving the ability to avoid local minima [36]. Applications are mostly in structural stiffness optimization, but BESO has been used to minimize the maximum Von Mises stress [36] and optimize the performance of compliant mechanisms [37]. BESO has been applied to commercial finite element codes as well [26].

2.2.2.5 Level set approach. The level-set approach defines the structure by creating a scalar function over the design domain where the structure is defined as regions where the function is negative [32]. The level-set function is continuous, such that the boundary of a two-dimensional structure is defined along the curve where the level-set function is equal to zero. As optimization iterations continue, the level-set function is modified based on objective function and constraint gradient values so that the volume of the structure defined is fixed. It is permissible for holes to nucleate within the structure region but adding solid regions to a section not in the structure is not permitted

if the region would be unsupported [32]. Level-set methods have been used with the density penalization method used above, as a mapping can be defined between the finite elements and their densities and the scalar level-set function.

2.2.2.6 Other topology optimization methods. Topology optimization is typically formulated as a constrained optimization with many design variables. Several new methods have recently been introduced that perform well but have not yet received the level of attention of the above widely used methods. For example, sequential linear or quadratic programming can be used to solve the topology optimization problem [38], which is a similar implementation to the MMA approach described above. In addition, the free material optimization approach can achieve an arbitrary level of geometric resolution [39] [40] with mesh refinement and perimeter constraints.

2.2.3 Applications

Although topology optimization of mechanical performance measures such as compliance served as the original motivation for topology optimization, topology optimization has been applied to a diverse group of problems. The following are several of the primary applications outside of mechanical performance, but this list is not exhaustive.

2.2.3.1 Heat transfer. Optimizing the thermal performance of a part can encompass many types of problems. The conduction properties of a heat fin can be optimized [24], by considering the thermal compliance which is analogous to mechanical compliance [41]. Minimizing thermal compliance corresponds to maximizing the fin temperature effectiveness. Convection has been included in heat transfer topology

optimization problems where convection has been coupled with fluid flow around the part [42]. Figure 2.12 shows an example of a topology-optimized heat fin.



Figure 2.12: Heat Fin Optimized for Thermal Compliance [43]

Other thermal heat transfer applications of topology optimization investigate the mechanical structural performance of parts under thermal loading. As the temperature of a structure changes, thermal stresses result from temperature gradients within the part which can deform the part mechanically. The thermal loading can be dependent on the parts' shape [44], as in the structure of an aircraft exhaust, or the thermal loading can derive from a fixed temperature change when the thermal expansion is constrained [44]. Under such weakly coupled thermomechanical loading where the optimization function is mechanical, but the loading is thermal or mixed thermal and mechanical, recent work suggests that optimizing compliance does not actually generate parts with maximum stiffness [45], [46]. For a given temperature increase, minimizing the strain energy of a structure generates a lower final maximum Von Mises stress than minimizing

compliance. Other objective functions have been considered for the weakly coupled thermomechanical problem [47]. In cases where thermal and mechanical properties are each desired, such as in a wall that must support a load while insulating an interior space, the analyses need not be coupled. In applications such as designing a heat fin with a desired efficiency that can also support a load, multi-objective optimization can be applied [44]. Thermal actuators have also been addressed as a weakly coupled thermomechanical problem, where the purpose is to maximize the displacement at a specific point [48]. Another complexity has been introduced to this system by applying a current to the structure and allowing resistance heating to generate the thermal behavior [49].

In weakly coupled thermomechanical systems where mechanical loading is included as well as stresses resulting from temperature changes, prior work in topology optimization has been limited to known temperature fields that are assumed given [50], [45], [46]. When the temperature field is design-dependent, significant additional complexity is introduced in the optimization problem as well as in the gradient calculations. To the best of our knowledge, the only work with design-dependent temperature field did not couple the thermal and mechanical analyses [44]. The work here seeks to advance the progress toward modeling the additive manufacturing process by considering a steady state weakly coupled thermomechanical system with design-dependent thermal and mechanical behavior.

2.2.3.2 Frequency of vibration. In large structures such as bridges or buildings [51], or structures subjected to repeated loading like engine components, cyclic loading at the fundamental frequency of vibration can cause premature failure of the part.

Maximizing the first natural frequency of the part is desirable and has been done with topology optimization using the homogenization method and with linear programming [24]. In these applications there is often another constraint or optimization function related to the deformation of the structure, as the part must meet other performance specifications. Compliance and the first natural frequency can be optimized simultaneously [31] in multiobjective optimization, where many mechanical parameters can be considered simultaneously [52]. In other applications the natural frequency has been optimized alone [53] [54].

2.2.3.3 Multiple material design. Early topology optimization applications assume that only one type of material is used in the part. Introducing a second material with a different set of material properties can improve the performance of structures under complex loading. Multiobjective problems with competing objective functions can benefit from including a second material, as in [44] where both the structural and heat transfer properties of residential building siding are simultaneously optimized. A mechanically stiff and thermally conductive material was considered with a mechanically weak but thermally insulating material to design the parts. Applications of structural optimization have included multiple materials, as in optimizing a dam where air, water, and concrete must each be considered individually. Additive manufacturing methods have been developed that use multiple thermoplastics in a single printed structure [6], so multimaterial design methods are now applicable to a large range of applications. In one formulation, topology optimization is performed with a second material that provides structural support for the material used for the main structure during the printing process. Other techniques use a strong, heavy material and a weaker but lighter material, or

materials with different heat conduction coefficients and densities for heat transfer problems [49].

2.2.3.4 Geometrically nonlinear problems. It is common to assume that the stress-strain relationship of the material used in mechanical topology optimization is linear, along with all structural responses. However, linearity cannot be assumed under large displacements or contact or sliding boundary conditions. If multiple distinct parts are considered in one analysis, then a contact boundary condition models the parts touching without being fixed together [55]. Compliant mechanisms often experience displacements large enough to exhibit nonlinear behavior, and may also include stresses beyond the proportional stress-strain limit [56]. Obtaining reliable convergence of the topology optimization for nonlinear systems can be difficult [57] and maximizing stiffness may not be accomplished by minimizing compliance. Also, when compliance optimization is performed on a linear elastic system, increasing the applied loads yields an identical final topology. However, when nonlinear systems are optimized, changing the applied loading can generate different structures. This nonlinearity makes it challenging to design a part that can be used in more than a single specific loading scenario.

2.2.3.5 Anisotropic materials. Topology optimization is widely used to design stiff lightweight parts [58], and due to recent developments in material performance various polymers are well-suited to be used in those parts. The high strength to weight ratio of plastics can be improved further by adding glass or carbon fibers to form a polymer matrix composite. Polymer composites such as carbon fiber-reinforced ABS plastic can approach the strength of aircraft-grade aluminum [17] at much lower weights. However,

polymer composites are often anisotropic with respect to elasticity and strength, which depends on the method used for manufacture. Additive manufacturing, while providing immense design freedom, is known to produce highly anisotropic parts [17]. Introducing reinforcing fibers in the form of short chopped fibers or continuous fibers increases the strength of the part primarily in the direction that the fibers align in.

Several material models have been proposed in order to accurately model polymer composites. The homogenization method allowed for anisotropic materials by allowing the shape and orientation of the microscopic voids to be changed, though this has not been directly applied to fiber-reinforced composites. Several methods exist to optimize the orientation of fibers within a part directly, where the topology of the part is given and various fibers throughout the part have discontinuous orientations to achieve maximum stiffness [59], [60]. Optimizing a set of fiber orientations is not as common in topology optimization as it does not determine the shape of a structure, so more general optimization methods are often considered as approaches like the OC and BESO methods were designed for use with isotropic material. General optimization methods can be combined with existing topology optimization methods like the OC and BESO approaches to simultaneously optimize the shape and fiber orientation of a structure [61]. Several methods for computing the optimal fiber orientation exist, including stress-based and strain-based formulations. Examples include fiber angles with discrete values [3] and also those with continuous values, depending on the manufacturing method under consideration. The stacking sequence of three-dimensional laminates has also been considered with the same method [62].

The original homogenization approach allowed for anisotropic voids in the microstructure of the material [24] in the form of rotated rectangles or triangles. While this can adequately represent the complexity of fiber orientation, the formulation involves more design variables than is necessary to represent the system, and it often leads to designs that cannot be manufactured using current technology, even with additive manufacturing techniques.

Another common topology optimization formulation adds a second design variable to each finite element to represent fiber angle orientation [59]. For example, Jiang et al. [63] assumed the material to be orthotropic, with the orientation defining the direction of maximum stiffness, as in [59] as well. The simplest approach considers a part with defined shape where all the orientations are assumed to be equal [64], which models an additively manufactured part where the material is extruded in all the same direction, as seen in Figure 2.13. The global part orientation can be optimized to determine which direction the part should be printed.

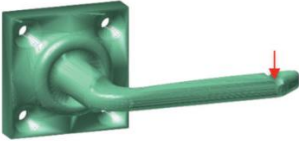



Problem Setup	Optimum Orientation
	 [-79.07°, 16.15°, -13.86°]
	 [117.10°, 26.19°, -180°]

Figure 2.13: Optimized Print Direction [64]

Additive manufacturing can print in arbitrary directions within a print plane, so allowing the finite elements' orientation to vary independently in the plane reflects this freedom. A two-dimensional problem was solved by Soto and Yang [59] for compliance minimization, where the shape of the part remained fixed. The optimal material orientation may need to be determined with a different method than that used in the topology optimization of density, particularly if the common topology optimization OC method is used (see e.g. Sigmund [22]) as it only includes density as a design variable. Strain or stress-based orientation optimization methods have been considered [61], though many approaches simply orient the elements in the direction of principal stress [65], [66].

In the Solid Orthotropic Method with Penalization (SOMP) [67] method, the density and material orientation optimization are performed simultaneously, whether the same method is used for both or not. When topologies are optimized under mechanical loading alone, Bendsoe et al. showed that a principal strain-based formulation may minimize compliance [68].

Under the SOMP formulation, the material orientations can range continuously or be confined to a set of allowable values. Restricting the allowable values of the angles to a finite set is applicable to the process of creating a composite laminate from several layers of woven fiber sheets, as in discrete material optimization [69], [70]. One example lamina is seen in Figure 2.14.

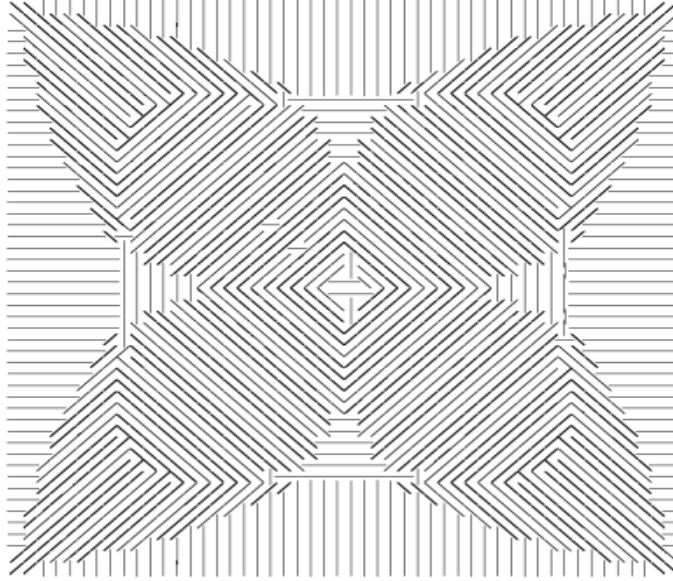


Figure 2.14: Discrete Material Optimization for Composite Lamina [70]

Figure 2.15, taken from Jiang et al. [63], shows the optimization process when the shape of a structure is optimized simultaneously with the material orientations. The structure considered is a beam in three-point bending.

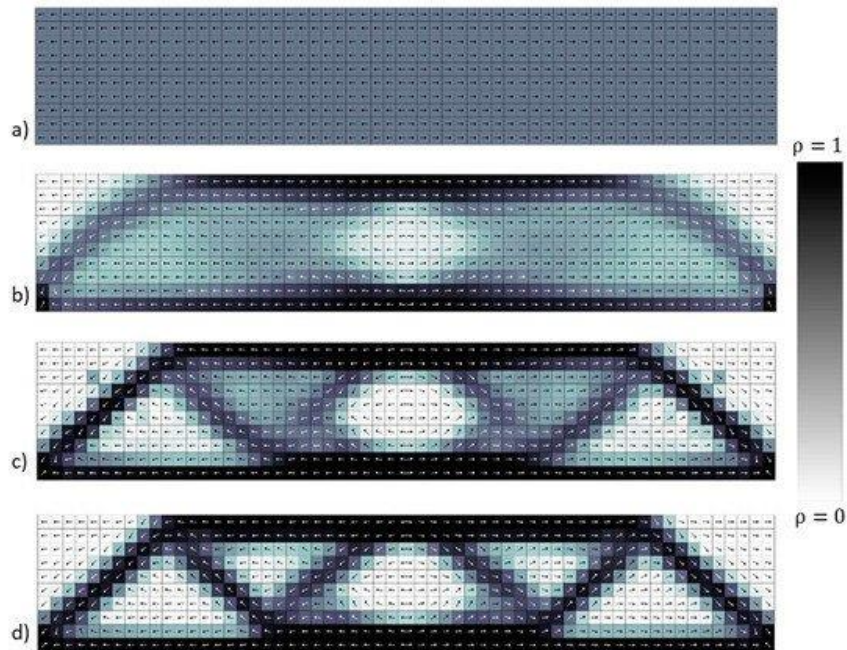


Figure 2.15: Continuous Fiber Angle Optimization [63]

Finally, [71] included a general anisotropic material model in a topology optimization where every component of the elasticity tensor can vary independently within the established rules of elasticity in each element. This allows complete freedom of material design, but it is not possible to manufacture a type of material that has arbitrary material properties, even with current AM techniques. The approach used in the research in this thesis is similar to the continuous fiber angle optimization (CFAO) method in Jiang, Hoglund, and Smith [63], as it uses continuous orientation variables that reflect additive manufacturing without adding unnecessary complexity.

2.3 Topology Optimization for Additively Manufactured Structures

Topology optimization has been used to design lightweight and stiff parts, but the geometry of the results are often complex and may display fractal-like behavior. As a result, the parts cannot often be produced by traditional manufacturing methods. The only viable method for production of many topology-optimized parts is additive manufacturing. In the past, the majority of research in topology optimization includes no actual production of test parts which could be due in part to additive manufacturing technologies lagging the development of topology optimization. Now, with additive manufacturing used in research and prototyping and beginning to be used to produce end-use parts [72], topology optimization is seeing increasing application in real-world applications. Some pre-processing and post-processing steps must still be taken when preparing to produce a part obtained through topology optimization [73], but the ease of constructing topology-optimized parts with additive manufacturing improves significantly on the large amount of post-processing necessary to produce a topology-optimized part with non-AM methods.

The anisotropic material behavior and thermal stresses present in additive manufacturing are the topic of the current research. Several related approaches have included anisotropic material properties, dating back to the original homogenization method as mentioned above. The recent development of the CFAO method [63] shows the success of simultaneous material orientation and density optimization. Including the thermal stresses is more complex. Much of the research cited above that considers thermal stresses are based on fixed, design-independent temperature fields, whether uniform or varying. To the best of our knowledge, research has yet to be done which captures the transient cooling process as the deposited material cools in a design or process optimization.

Also, while steady-state thermal stress and material anisotropy have both been considered separately, they have not been considered simultaneously. The method presented in Chapter 3 includes both factors and expands the thermal behavior to a steady-state design dependent temperature field. While this work does not fully encompass the complexity of an AM cooling process, it advances the ability to model and optimize additively manufactured structures.

The research here extends the work of two previous graduate students at Baylor University. The first work considered compliance minimization of two-dimensional structures with anisotropic material properties [74]. The anisotropy was considered as a fixed material property, and then as a set of design variables. This work was extended to three-dimensional systems by Jiang [75], who used a general Matlab optimizer. The code used in both prior theses began from Sigmund's 99-line Matlab code [22] for isotropic

compliance minimization. The thermomechanical topology optimization presented here also starts with Sigmund's work and builds on the earlier work by Hoglund and Jiang.

CHAPTER THREE

Methods

3.1 Design Space and Optimization Function

The density method [22] is adopted in the design approach presented here, as it is extended to solve the thermomechanical problem considered here with the fewest design variables. The homogenization method [25] is not used in the current works because it requires design variables for the length, width, and orientation of rectangular holes to define the microstructure [25] which leads to unwanted designs. The homogenization method requires more design variables than the density method, which would add computational expense while not providing a structure suitable for additive manufacturing.

The density method is a topology optimization approach that defines the design space and related design variables while being compatible with a variety of update schemes. The optimality criterion method and globally convergent method of moving asymptotes have both been widely adopted for structural optimization, such that both are considered in this work. The topology optimization design domain is presented first for a problem with mechanical loading only as in Sigmund [22], and then the approach is extended to a steady state weakly coupled thermomechanical problem that more closely simulate additive manufacturing processes. Material anisotropy is introduced through additional design variables which are included in both the material model and optimization methods. Special attention is given to the design sensitivities which are

needed for efficient implementation of the topology optimization method used in this work. Convergence issues encountered in the optimization implementation are discussed, along with other modifications done to the optimization methods.

3.1.1 Finite Element Formulation

The finite elements method commonly used to compute the numerical solution of partial differential equations for elastic deformation of a structural system form the basis of our topology optimization method. The strong form of the associated elasticity problem can be written in two dimensions as the steady-state equations of motion

$$\frac{\partial \sigma_{xx}}{\partial x} + \frac{\partial \sigma_{xy}}{\partial y} + f_x = 0 \quad (3.1)$$

$$\frac{\partial \sigma_{xy}}{\partial x} + \frac{\partial \sigma_{yy}}{\partial y} + f_y = 0 \quad (3.2)$$

The equilibrium is written in terms of strains σ_{xx} , σ_{xy} , and σ_{yy} , which are a function of the displacement fields. The body force vector f can be expressed in terms of components as $f = \begin{Bmatrix} f_x \\ f_y \end{Bmatrix}$. The stress – strain relationship utilizes the material properties to relate the stresses to the strains as

$$\begin{Bmatrix} \sigma_{xx} \\ \sigma_{yy} \\ \sigma_{xy} \end{Bmatrix} = \begin{bmatrix} c_{11} & c_{12} & 0 \\ c_{12} & c_{22} & 0 \\ 0 & 0 & c_{66} \end{bmatrix} \begin{Bmatrix} \varepsilon_{xx} \\ \varepsilon_{yy} \\ \varepsilon_{xy} \end{Bmatrix} \quad (3.3)$$

The strains can then be expressed in terms of the displacements by the definition of strains written as

$$\begin{Bmatrix} \varepsilon_{xx} \\ \varepsilon_{yy} \\ \varepsilon_{xy} \end{Bmatrix} = \begin{Bmatrix} \frac{\partial u_x}{\partial x} \\ \frac{\partial u_y}{\partial y} \\ \frac{1}{2} \left(\frac{\partial u_x}{\partial y} + \frac{\partial u_y}{\partial x} \right) \end{Bmatrix} \quad (3.4)$$

Where u_x and u_y are the displacements in the x – and y – coordinate directions. The c_{ij} terms are elastic stiffness terms that can be expressed in terms of the material properties as follows. This research assumes a plane strain condition with an orthotropic material which yields

$$c_{11} = \frac{E_x(1 - \nu_{xy})}{(1 + \nu_{xy})(1 - \nu_{xy} - \nu_{yx})} \quad (3.5)$$

$$c_{22} = \frac{E_y(1 - \nu_{yx})}{(1 + \nu_{yx})(1 - \nu_{xy} - \nu_{yx})} \quad (3.6)$$

$$c_{66} = G_{xy} \quad (3.7)$$

The Young's moduli in the global x and y directions at an arbitrary location are E_x and E_y respectively, and the related Poisson's ratios are ν_{xy} and ν_{yx} . Note that the material properties can be spatially varying and that $\nu_{xy}E_y = \nu_{yx}E_x$, as is usual for orthotropic materials. For the first model described below, the material is assumed to be isotropic, i.e. $E_x = E_y$ and they are constant across the entire domain. The G_{xy} term in Equation 3.7 is the shear modulus. Equations 3.3 – 3.7 can be substituted into Equations 3.1 and 3.2 to express the strong form of the governing equations in terms of the displacements as

$$\frac{\partial}{\partial x} \left(c_{11} \frac{\partial u_x}{\partial x} + c_{12} \frac{\partial u_y}{\partial y} \right) + \frac{\partial}{\partial y} \left(c_{66} \frac{\partial u_x}{\partial y} + c_{66} \frac{\partial u_y}{\partial x} \right) = -f_x \quad (3.8)$$

$$\frac{\partial}{\partial x} \left(c_{66} \frac{\partial u_x}{\partial y} + c_{66} \frac{\partial u_y}{\partial x} \right) + \frac{\partial}{\partial y} \left(c_{12} \frac{\partial u_x}{\partial x} + c_{22} \frac{\partial u_y}{\partial y} \right) = -f_y \quad (3.9)$$

The strong form can be converted to the weak form over an arbitrary domain Ω_e with boundary Γ_e in the standard manner with two arbitrary weight functions w_1 and w_2 to obtain

$$0 = \int_{\Omega_e} \frac{\partial w_1}{\partial x} \left(c_{11} \frac{\partial u_x}{\partial x} + c_{12} \frac{\partial u_y}{\partial y} \right) + c_{66} \frac{\partial w_1}{\partial y} \left(\frac{\partial u_x}{\partial y} + \frac{\partial u_y}{\partial x} \right) dx dy - \int_{\Omega_e} w_1 f_x dx dy - \oint_{\Gamma_e} w_1 t_x ds \quad (3.10)$$

$$0 = \int_{\Omega_e} c_{66} \frac{\partial w_2}{\partial x} \left(\frac{\partial u_x}{\partial y} + \frac{\partial u_y}{\partial x} \right) + \frac{\partial w_2}{\partial y} \left(c_{12} \frac{\partial u_x}{\partial x} + c_{22} \frac{\partial u_y}{\partial y} \right) dx dy - \int_{\Omega_e} w_2 f_y dx dy - \oint_{\Gamma_e} w_2 t_y ds \quad (3.11)$$

The boundary traction forces in the x – and y – directions are t_x and t_y respectively. Once weight functions and element domains are selected, Equations 3.10 and 3.11 can be applied to any two-dimensional domain. In practice, all of the integrals involved are evaluated using two-point Gauss quadrature. The domains are chosen to be elements, which consist of a region of space with specific nodes.

To evaluate the integrals in Equations 3.10 and 3.11 over an arbitrary n -noded finite element, the primary variables u_x and u_y are approximated throughout the element with interpolation functions $\psi_j(x, y)$ and the nodal values u_x^j and u_y^j as

$$u_x \approx \sum_{j=1}^n u_x^j \psi_j(x, y) \quad u_y \approx \sum_{j=1}^n u_y^j \psi_j(x, y) \quad (3.12)$$

The interpolation functions must be at least bilinear. Equation 3.12 can be written in matrix form as

$$\mathbf{u} = \begin{Bmatrix} u_x \\ u_y \end{Bmatrix} = \mathbf{\Psi} \mathbf{\Delta} \quad (3.13)$$

where $\mathbf{u} = \begin{Bmatrix} u_x \\ u_y \end{Bmatrix}$ and the nodal displacement vector $\mathbf{\Delta}$ is defined as

$$\mathbf{\Delta} = \{u_x^1 \quad u_y^1 \quad u_x^2 \quad u_y^2 \quad \dots \quad u_x^n \quad u_y^n\}^T \quad (3.14)$$

where the superscript T indicates the transpose operation. In Equation 3.15, the interpolation functions are assembled into the matrix

$$\mathbf{\Psi} = \begin{bmatrix} \psi_1 & 0 & \psi_2 & 0 & \dots & \psi_n & 0 \\ 0 & \psi_1 & 0 & \psi_2 & \dots & 0 & \psi_n \end{bmatrix} \quad (3.15)$$

The interpolation functions used for displacements \mathbf{u} are also chosen for the weight functions w_1 and w_2 , as is typical in the Galerkin finite element method [76]. The displacements in Equation 3.13 can be substituted into the weak form (Equations 3.10 and 3.11) and written in vector form. Defining the following gathering matrix simplifies the expression

$$\mathbf{D} = \begin{bmatrix} \frac{\partial}{\partial x} & 0 & \frac{\partial}{\partial y} \\ 0 & \frac{\partial}{\partial y} & \frac{\partial}{\partial x} \end{bmatrix} \quad (3.16)$$

which makes it convenient to define the displacement gradient matrix \mathbf{B} as

$$\mathbf{B} = \mathbf{D} \mathbf{\Psi} = \begin{bmatrix} \frac{\partial \psi_1}{\partial x} & 0 & \frac{\partial \psi_2}{\partial x} & 0 & \dots & \frac{\partial \psi_n}{\partial x} & 0 \\ 0 & \frac{\partial \psi_1}{\partial y} & 0 & \frac{\partial \psi_2}{\partial y} & \dots & 0 & \frac{\partial \psi_n}{\partial y} \\ \frac{\partial \psi_1}{\partial y} & \frac{\partial \psi_1}{\partial x} & \frac{\partial \psi_2}{\partial y} & \frac{\partial \psi_2}{\partial x} & \dots & \frac{\partial \psi_n}{\partial y} & \frac{\partial \psi_n}{\partial x} \end{bmatrix} \quad (3.17)$$

Combining Equations 3.12 and 3.13 with the weak form in Equations 3.10 and 3.11

yields the usual element level steady-state finite element equilibrium

$$\mathbf{K}^e \mathbf{U}^e = \mathbf{F}^e + \mathbf{Q}^e \quad (3.18)$$

where each term is defined as

$$\mathbf{K}^e = \int_{\Omega_e} \mathbf{B}^T \mathbf{C} \mathbf{B} d\Omega_e, \quad \mathbf{F}^e = \int_{\Omega_e} \mathbf{\Psi}^T \mathbf{f} d\Omega_e, \quad \mathbf{Q}^e = \oint_{\Gamma_e} \mathbf{\Psi}^T \mathbf{t} ds \quad (3.19)$$

In the above, the element stiffness matrix \mathbf{K}^e is a square matrix of size $2n$, and both the elemental load vector \mathbf{F}^e and internal force vector \mathbf{Q}^e are $2n \times 1$. Elemental equilibrium can be summed at the corresponding nodal displacements and forces to yield the global finite element equilibrium in terms of the global stiffness matrix \mathbf{K} , global nodal displacement vector \mathbf{U} , and global load vectors \mathbf{F} and \mathbf{Q} , where equilibrium may be written as

$$\mathbf{K} \mathbf{U} = \mathbf{F} + \mathbf{Q} \quad (3.20)$$

Note that the local elemental stiffness matrices \mathbf{K}^e are assembled to form the global stiffness matrix \mathbf{K} , and likewise the global displacements \mathbf{U} and the global force vectors \mathbf{F} and \mathbf{Q} are assembled from the elemental displacements \mathbf{U}_e and forces \mathbf{F}_e and \mathbf{Q}_e .

The equilibrium in Equation 3.20 can be solved for unknown displacements and forces by partitioning the matrices and vectors with respect to fixed and free degrees of freedom, as is standard in finite element problems. The resulting reduced system does not have the singularity issue in Equation 3.20 once a sufficient set of fixed degrees of freedom are defined, and therefore may be solved using an appropriate linear system equation solver.

The finite element system in Equation 3.20 is defined for the mechanical elasticity equilibrium. Later in this work, the conduction heat transfer problem is also considered. Coupling between the two models will occur through the force vector where thermal stresses are generated.

While the above equations may employ finite elements of arbitrary shape, identically sized square bi-linear finite elements are used in this work. The identical size

and shape cause certain parts of the elemental stiffness matrix evaluation to be equivalent, which decreases the computational burden in the finite element solution. For an isotropic material, the elemental stiffness matrix for the bi-linear square finite element can be expressed as a function of the isotropic Young's modulus E and Poisson's ratio ν , as shown in [22]

$$K^e = \frac{E}{1-\nu^2} \begin{bmatrix} \frac{1}{2} - \frac{\nu}{6}, & \frac{1}{8} + \frac{\nu}{8}, & -\frac{1}{4} - \frac{\nu}{12}, & -\frac{1}{8} + \frac{3\nu}{8}, & -\frac{1}{4} + \frac{\nu}{12}, & -\frac{1}{8} - \frac{\nu}{8}, & \frac{\nu}{6}, & \frac{1}{8} - \frac{3\nu}{8} \\ \frac{1}{8} + \frac{\nu}{8}, & \frac{1}{2} - \frac{\nu}{6}, & \frac{1}{8} - \frac{3\nu}{8}, & \frac{\nu}{6}, & -\frac{1}{8} - \frac{\nu}{8}, & -\frac{1}{4} + \frac{\nu}{12}, & -\frac{1}{8} + \frac{3\nu}{8}, & -\frac{1}{4} - \frac{\nu}{12} \\ -\frac{1}{4} - \frac{\nu}{12}, & \frac{1}{8} - \frac{3\nu}{8}, & \frac{1}{2} - \frac{\nu}{6}, & -\frac{1}{8} - \frac{\nu}{8}, & \frac{\nu}{6}, & -\frac{1}{8} + \frac{3\nu}{8}, & -\frac{1}{4} + \frac{\nu}{12}, & \frac{1}{8} + \frac{\nu}{8} \\ -\frac{1}{8} + \frac{3\nu}{8}, & \frac{\nu}{6}, & -\frac{1}{8} - \frac{\nu}{8}, & \frac{1}{2} - \frac{\nu}{6}, & \frac{1}{8} - \frac{3\nu}{8}, & -\frac{1}{4} - \frac{\nu}{12}, & \frac{1}{8} + \frac{\nu}{8}, & -\frac{1}{4} + \frac{\nu}{12} \\ -\frac{1}{4} + \frac{\nu}{12}, & -\frac{1}{8} - \frac{\nu}{8}, & \frac{\nu}{6}, & \frac{1}{8} - \frac{3\nu}{8}, & \frac{1}{2} - \frac{\nu}{6}, & \frac{1}{8} + \frac{\nu}{8}, & -\frac{1}{4} - \frac{\nu}{12}, & \frac{1}{8} + \frac{3\nu}{8} \\ -\frac{1}{8} - \frac{\nu}{8}, & -\frac{1}{4} + \frac{\nu}{12}, & -\frac{1}{8} + \frac{3\nu}{8}, & -\frac{1}{4} - \frac{\nu}{12}, & \frac{1}{8} + \frac{\nu}{8}, & \frac{1}{2} - \frac{\nu}{6}, & \frac{1}{8} - \frac{3\nu}{8}, & \frac{\nu}{6} \\ \frac{\nu}{6}, & -\frac{1}{8} + \frac{3\nu}{8}, & -\frac{1}{4} + \frac{\nu}{12}, & \frac{1}{8} + \frac{\nu}{8}, & -\frac{1}{8} - \frac{\nu}{8}, & \frac{1}{4} - \frac{\nu}{12}, & \frac{1}{8} - \frac{3\nu}{8}, & -\frac{1}{4} - \frac{\nu}{12} \\ \frac{1}{8} - \frac{3\nu}{8}, & \frac{1}{4} - \frac{\nu}{12}, & \frac{1}{8} + \frac{\nu}{8}, & -\frac{1}{4} + \frac{\nu}{12}, & \frac{1}{8} + \frac{3\nu}{8}, & \frac{\nu}{6}, & -\frac{1}{8} - \frac{\nu}{8}, & \frac{1}{2} - \frac{\nu}{6} \end{bmatrix} \quad (3.21)$$

3.1.2 Design Domain

This research considers structures defined over a two-dimensional region in space which may be discretized into multiple finite elements. The same finite element mesh is used here for both the elasticity analysis described above and the thermal analysis in the sections to follow. Initially, only the mechanical analysis is considered, and the thermal and thermomechanical analyses will be included subsequently in Section 3.7. Figure 3.1 shows an example of a two-dimensional design domain.

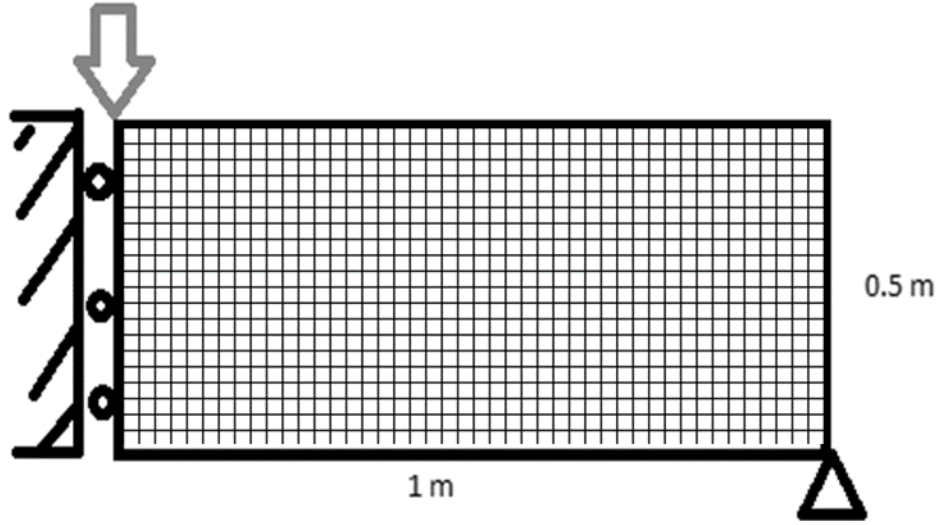


Figure 3.1: Example Two-Dimensional Design Domain

Boundary conditions for the elasticity problem are fixed displacements and applied nodal forces. The linear finite element equilibrium in Equation 3.20 is enforced across the design domain, and it is assumed that no element edge traction forces are applied in our example problems, i.e. ($\mathbf{Q} = \mathbf{0}$). Thus, Equation 3.20 reduces to

$$\mathbf{K}\mathbf{U} = \mathbf{F} \quad (3.22)$$

3.1.3 Optimization Function

In systems where only mechanical loading of a linearly elastic material is considered, minimizing the compliance of the structure maximizes its stiffness. Compliance was the objective function used in Bendsoe and Kikuchis' original homogenization approach [25] which continues to be common in topology optimization of mechanical systems. The structural compliance \mathcal{C} can be expressed in terms of the global finite element variables as

$$\mathcal{C} = \mathbf{U}^T \mathbf{F} = \mathbf{U}^T \mathbf{K} \mathbf{U} \quad (3.23)$$

Note that some authors define compliance as $C = \frac{1}{2} \mathbf{U}^T \mathbf{F}$, however, the definition in Equation 3.23 was chosen here to allow for more straightforward comparison to strain energy, which will be considered as a design metric in the discussion in Section 4.4. Depending on the design requirements, other objective functions may be considered. For example, minimizing the maximum displacement or maximum Von Mises stress, or the displacement at a specific point may be most useful for a specific scenario. When thermal factors are considered, minimizing compliance is not guaranteed to maximize the stiffness of the part [77] and other objective functions should be considered.

3.1.4 Finite Element Discretization and Design Variables

The creation of a structure within the design domain is modeled by defining the amount of material in each finite element with an associated density design variable ρ_i that ranges from 0 to 1. The element density ρ_i represents whether the element contains material or is void, where a density of $\rho_i = 1$ designates an element that is completely full of material and a density of $\rho_i = 0$ indicates that an element is void of material. There is no physical interpretation for a fractional density, however, densities are permitted to take on values between 0 and 1 in the optimization process. Several interpolation methods exist that model fractional densities. The method used here is a modification of the Solid Isotropic Material with Penalization (SIMP) approach [24], where the elemental stiffness of element i is expressed as a function of the density as

$$\mathbf{K}_i = \rho_i^p \mathbf{K}_0 \quad (3.24)$$

where \mathbf{K}_0 is given in Equation 3.21 for a square element having an isotropic material. The penalty parameter p is used to penalize the stiffness of elements with intermediate densities so that as the optimization algorithm progresses element density values tend

toward solid or void since intermediate density states are structurally less efficient. This is desirable, as only density values of 0 or 1 have physical interpretation and fractional density values cannot be produced. The penalty is often set to 3 [22]. The set of all densities in the design space can be represented in graphical form by shading each element according to their density. Figure 3.2 shows densities in a portion of a design domain where a value of 1 is black, a density of 0 is white, and fractional densities are grayscale interpolations.

Other penalty methods exist that offer unique advantages [24] compared to that in Equation 3.24. The SIMP method uses only one heuristic parameter p which may require tuning and the stresses become unbounded as the element density approaches 0. The RAMP penalization approach [24] (Rational Approximations of Material Properties) has two heuristic parameters but eliminates the unbounded stress behavior found in the SIMP approach. Our research currently does not optimize the stress or use any stress-based constraints, so the SIMP method is used for its simplicity.

The compliance objective function C in Equation 3.22 can be written in terms of the design variables ρ_i , individual element stiffness matrices, and the local elemental displacements \mathbf{U}_i as

$$\min_{\bar{\rho}} C = \sum_{i=1}^{N_{el}} \rho_i^p \mathbf{U}_i^T \mathbf{K}_0 \mathbf{U}_i \quad (3.25)$$

where \mathbf{K}_0 is described in Equation 3.21 above, and there are N_{el} finite elements in the discretization.

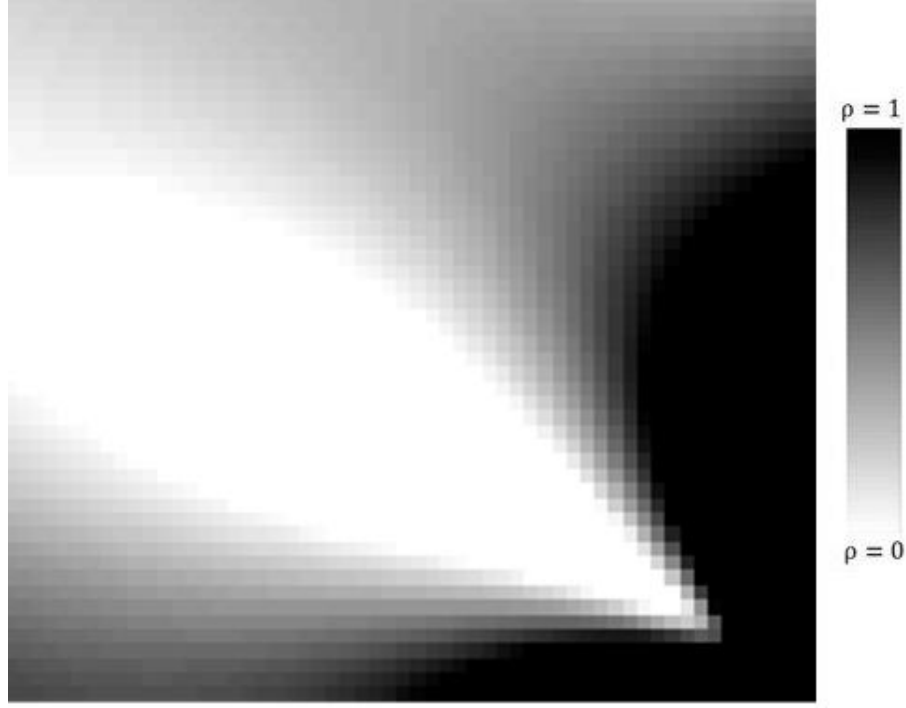


Figure 3.2: Density Visualization

Representing the objective function as a sum over the element matrices in terms of the design variables ρ_i provide a highly efficient computation of the objective function and its design gradient, which will be needed in the iterative update scheme used to solve the topology optimization described below. Note that nodal displacements $\mathbf{U}_i = \mathbf{U}_i(\hat{\rho})$ are functions of the element densities $\hat{\rho}$ through the finite element solution $\mathbf{K}(\hat{\rho})\mathbf{U}(\hat{\rho}) = \mathbf{F}(\hat{\rho})$, and this coupled dependency must be considered in design sensitivity derivations.

3.1.5 Constraint: Volume Fraction

In the compliance optimization problem, the minimum compliance could be achieved by setting all of the design variables equal to 1, as this fills the design space completely with material, which also maximizes the stiffness. However, it is often not desirable for the structure to consist of a single block of material. In many applications a

lightweight part is desired to minimize the cost of material or energy necessary. A predefined amount of material can be given for the construction of the structure, which limits the sum of the densities in the design domain. A volume constraint that limits the amount of material in the optimum design can be defined through the equality constraint

$$\frac{1}{A_{net}} \sum_{i=1}^{N_{el}} \rho_i A_i = V_f \quad (3.26)$$

where the total area of the part is A_{net} and the area of element i is A_i . The volume fraction V_f is a predefined constant taking values between 0 and 1 that represents what fraction of the design space that is occupied by material. In the case where every element is the same size, as is considered in this research, Equation 3.25 becomes

$$\frac{1}{N_e} \sum \rho_i = V_f \quad (3.27)$$

where N_e is the number of elements, which in our study equates to the number of design variables n . Note that when only mechanical compliance optimization is included, adding more material will always make the part stiffer so the equality sign in Equations 3.26 and 3.27 can be replaced with an inequality and the optimization will naturally find a solution along the constraint. This is not always the case in thermomechanical systems for design-dependent thermal loading.

3.1.6 Optimization Problem

The topology optimization problem for minimum compliance of an elastic structure under static loads considered above can be stated as

$$\begin{aligned}
\min_{\vec{x}} C &= \sum_{i=1}^{N_{el}} \rho_i^p \mathbf{U}_i^T \mathbf{K}_0 \mathbf{U}_i \\
\text{such that } \frac{1}{N_i} \sum_{i=1}^{N_{el}} \rho_i &= V_f \\
0 < \rho_{min} < \rho_i &\leq 1
\end{aligned} \tag{3.28}$$

where the objective function, compliance C , is expressed in terms of the mechanical finite element stiffness matrix and displacement vector and the design variables x_i . The single equality volume constraint fixes the amount of material in the structure. Note that the element densities ρ_i are bounded between a constant ρ_{min} that satisfies $0 < \rho_{min} < \rho_i \ll 1$ and 1. This is because an element density of $\rho_i = 0$ causes a singularity in the global stiffness matrix \mathbf{K} and must be avoided. It is common to set $\rho_{min} = 0.001$ [22], which is the value used in this work.

3.1.7 Classes of Optimization Techniques

A significant attribute an optimization approach is the need for the design gradient of the objective function and constraints. Traditional optimization approaches such as sequential linear or quadratic programming, Newton's method, and the method of steepest descent, rely on the gradient to find a local minimum. Optimality criterion-based method, the method of moving asymptotes, and the level-set method are all frequently used for topology optimization, and these methods also incorporate the gradients. These methods can be computationally intensive when the design gradient involves time consuming calculations, and there is no guarantee that the local minimum found is the global minimum. This research uses an optimality criteria method [22] and also a method

of moving asymptotes [23] to solve the topology optimization problem, both of which require design gradients.

Optimization methods that do not require the gradient are often based on heuristic algorithms [35]. The evolutionary structural optimization methods remove and add material based on local objective function values without requiring the gradient. Genetic algorithms can be applied to solve topology optimization problems [24], although the required computation become excessive for a large number of design variables as in a typical topology optimization problem. The genetic algorithm generates many different potential solutions, then selects and recombines them in a way that mimics natural selection to determine the fittest solution. The randomness inherent in the genetic algorithm formulation means that the same starting set of solutions can reach different optima in different runs, but the random nature of the iteration can allow the algorithm to escape local minima. It constrains the element densities to discrete values of ρ_{min} or 1 and would not need to consider density penalization.

A gradient-based approach was chosen as a means to solve the topology optimization problem in this research. The design space of a topology optimization problem typically has an extremely high number of variables, making a genetic algorithm computationally prohibitive as each iteration holds a population of several dozen to several hundred design points. The evolutionary approaches, while simple, neglect the coupled effects of densities on each other. While assuming element density independence is a feasible approximation for small element density changes in purely mechanical compliance optimization, it was found in the course of this work that in the systems modeled here the objective function and design sensitivities are sensitive to small

changes in density, indicating that the independence of element density assumption is a less-accurate approximation in this system.

Of the numerous gradient-based optimization approaches available in the literature, we choose the optimality criterion-based approach (OC approach [22]) and the globally convergent method of moving asymptotes (GCMMA approach [23]) for this research. Matlab codes for both methods are freely available for compliance minimization of mechanical systems. Design gradients in our work are evaluated via the adjoint method.

3.2 Design Sensitivity via the Adjoint Method

As described above, topology optimization solutions are typically obtained with gradient-based algorithms. Given the large number of design variables in a topology optimization, special attention must be given to the calculation of the design derivatives, often referred to as design sensitivities. Design sensitivities for problems that include the solution of a system of equations such as that given in Equation 3.20, a significant reduction in computational cost and improved accuracy may be obtained using the Direct Differentiation Method or the Adjoint Variable Method [56]. Here we employ the Adjoint Variable Method as it is well understood that it is highly efficient for design problems having more design variables than implicit performance measures such as that considered in our topology optimization in Equation 3.28.

In the topology optimization problem described above, the compliance is given in terms of the global finite element variables [22] as

$$C = \mathbf{U}^T \mathbf{F} \quad (3.29)$$

The finite element equilibrium in Equation 3.20, $\mathbf{KU} = \mathbf{F}$, may be rearranged as $\mathbf{KU} - \mathbf{F} = \mathbf{0}$ to define the augmented compliance \hat{C} as

$$\hat{C} = C - \lambda(\mathbf{KU} - \mathbf{F}) \quad (3.30)$$

where we note that $C = \hat{C}$ for the displacement solution \mathbf{U} that satisfies equilibrium. The augmented compliance \hat{C} in Equation 3.29 is written in terms of the Lagrange Multiplier λ , which is an arbitrary vector of the same size as the global displacement vector \mathbf{U} . The total derivative of \hat{C} , denoted $\frac{D\hat{C}}{D\rho_i}$, can then be taken using the chain rule to obtain

$$\frac{D\hat{C}}{D\rho_i} = \frac{D}{D\rho_i}(C) - \lambda \frac{D}{D\rho_i}(\mathbf{KU} - \mathbf{F}) - \frac{D\lambda}{D\rho_i}(\mathbf{KU} - \mathbf{F}) \quad (3.31)$$

where we note that $\frac{D\hat{C}}{D\rho_i} = \frac{D}{D\rho_i}(C)$ at the finite element solution $\mathbf{KU} = \mathbf{F}$. Recognizing that the compliance is a function of both \mathbf{U} and \mathbf{F} , and with $\mathbf{KU} - \mathbf{F} = \mathbf{0}$, Equation 3.30 can then be written as

$$\frac{D\hat{C}}{D\rho_i} = \frac{dC}{d\mathbf{U}} \frac{D\mathbf{U}}{D\rho_i} + \frac{dC}{d\mathbf{F}} \frac{D\mathbf{F}}{D\rho_i} - \lambda \left(\frac{D\mathbf{K}}{D\rho_i} \mathbf{U} + \mathbf{K} \frac{D\mathbf{U}}{D\rho_i} - \frac{D\mathbf{F}}{D\rho_i} \right) \quad (3.32)$$

It is computationally expensive to determine the change in the global displacement vector with respect to all element densities, and this would be needed to be evaluated for each term in the gradient vector if Equation 3.31 is used directly (see e.g. the Direct Differentiation Method [48]). Therefore, it is desirable to eliminate the $\frac{D\mathbf{U}}{D\rho_i}$ term by first collecting these terms as

$$\frac{D\hat{C}}{D\rho_i} = \left(\frac{dC}{d\mathbf{U}} - \lambda \mathbf{K} \right) \frac{D\mathbf{U}}{D\rho_i} + \left(\frac{dC}{d\mathbf{F}} + \lambda \right) \frac{D\mathbf{F}}{D\rho_i} - \lambda \frac{D\mathbf{K}}{D\rho_i} \mathbf{U} \quad (3.33)$$

The derivative of compliance (cf. Equation 3.28) with respect to \mathbf{U} and also with respect to \mathbf{F} may be substituted into Equation 3.32 to obtain

$$\frac{D\hat{C}}{D\rho_i} = (\mathbf{F} - \lambda\mathbf{K}) \frac{D\mathbf{U}}{D\rho_i} + (\mathbf{U}^T + \lambda) \frac{D\mathbf{F}}{D\rho_i} - \lambda \frac{D\mathbf{K}}{D\rho_i} \mathbf{U} \quad (3.34)$$

It is desirable to eliminate the first term on the right side of Equation 3.34, so we choose

$\lambda = \mathbf{U}^T$ such that $(\mathbf{F} - \lambda\mathbf{K}) \frac{D\mathbf{U}}{D\rho_i} = (\mathbf{F} - \mathbf{K}\mathbf{U}) \frac{D\mathbf{U}}{D\rho_i} = \mathbf{0}$ for symmetric \mathbf{K} . As a result, the

derivative simplifies to

$$\frac{D\hat{C}}{D\rho_i} = 2\mathbf{U}^T \frac{D\mathbf{F}}{D\rho_i} - \mathbf{U}^T \frac{D\mathbf{K}}{D\rho_i} \mathbf{U} \quad (3.35)$$

Note that when the global force vector is constant, related components of $\frac{D\mathbf{F}}{D\rho_i}$ are zero. In

addition, when tall fixed displacements considered are set to zero, the related fixed

degrees of freedom of \mathbf{U}^T are zero. Under these conditions, the term $2\mathbf{U}^T \frac{D\mathbf{F}}{D\rho_i}$ in Equation

3.35 equates to zero. Therefore, the design sensitivity for constant applied force and zero prescribed displacements consists of only one term

$$\frac{D\hat{C}}{D\rho_i} = -\mathbf{U}^T \frac{D\mathbf{K}}{D\rho_i} \mathbf{U} \quad (3.36)$$

Evaluation of Equation 3.36 can be simplified for our topology optimization

problem by noting that any one of the element stiffness matrices \mathbf{K}_i is only a function of

the corresponding elemental density ρ_i . For the identically sized linear finite elements

used in this work, Equation 3.36 becomes

$$\frac{DC}{D\rho_i} = -\mathbf{U}_i^T \frac{D\mathbf{K}_i}{D\rho_i} \mathbf{U}_i = -\mathbf{U}_i^T \frac{D}{D\rho_i} (\rho_i^p \mathbf{K}_i) \mathbf{U}_i = -p\rho_i^{p-1} \mathbf{U}_i^T \mathbf{K}_i \mathbf{U}_i \quad (3.37)$$

which is easily implemented once the \mathbf{U}_i are computed, as it is only in terms of the local finite element variables and the densities.

3.3 Optimality Criteria Method

The first topology optimization method considered in this work, the Optimality Criterion (OC) based method, is a heuristic gradient-based update scheme developed specifically for topology optimization. It was used by Bendsoe [22] for compliance optimization of two-dimensional mechanical parts subject to a volume fraction constraint. The gradient is used in a heuristic update step that inherently preserves the volume fraction constraint as an equality constraint at each iteration.

3.3.1 Update Scheme

The densities are assumed to all be equal to the prescribed volume fraction V_f at the beginning of the optimization solution process. Each density $\rho_i, i = 1, \dots, N_e$ is updated according to the design sensitivities

$$\rho_i^{new} = \begin{cases} \max(\rho_{min}, \rho_i - m), & \text{if } \rho_i B_i^\eta \leq \max(\rho_{min}, \rho_i - m) \\ \min(1, \rho_i + m), & \text{if } \rho_i B_i^\eta \geq \min(1, \rho_i + m) \\ \rho_i B_i^\eta, & \text{else} \end{cases} \quad (3.38)$$

The densities are bounded to remain within the range of ρ_{min} to 1, and a move limit of m is implemented to prevent large changes to density that could lead to oscillating convergence behavior. The coefficient η serves as a numerical damping coefficient and is often set to 0.5. It is used to accelerate convergence [22] but may be set as $\eta = 1$ if no numerical damping is desired. The term B_i in Equation 3.37 is defined in terms of the design sensitivities as

$$B_i = \frac{\frac{-dC}{d\rho_i}}{\gamma} \quad (3.39)$$

Here, the design sensitivity of compliance with respect to the i th element is denoted $\frac{dC}{d\rho_i}$. The constant γ is chosen at each iteration so that the sum of the updated densities still respects the volume fraction constraint in Equation 3.27. The value of γ is the same for all x_i within a given iteration, so a separate one-dimensional optimization is performed at each iteration to find λ . We use a bisection method for this purpose, as in Sigmund [22], as λ can be bounded between 0 and a sufficiently large number, but other methods like a golden-section search may be employed.

Convergence of the topology optimization criteria algorithm can be defined with several different methods. A fixed number of iterations can be performed, or a condition can be imposed on the gradient magnitude or density change. In Sigmund's implementation of the optimality criterion method [22], a design is considered converged when the maximum change in the set of element densities ρ_i in a single iteration drops below 0.01, which can be formulated as

$$\max(|\rho_{i_{new}} - \rho_i|) < 0.01 \quad (3.40)$$

This convergence criteria proves to be a conservative estimate in the tests conducted by the authors [22], as once Equation 3.39 is satisfied the design is usually found to have converged. However, it is often possible to determine the final design well before the threshold in Equation 3.39 has been reached. As this work seeks to compare the optimality criteria method and the GCMMA approach, a given number of iterations will be conducted to ensure that the comparison between the methods is consistent.

3.4 The Globally Convergent Method of Moving Asymptotes

The method of moving asymptotes (MMA [23]) algorithm and its family of related methods are modified linear programming methods that are designed for general

optimization. They are designed to solve an optimization problem of the following form [23]

$$\text{minimize } f_0(\mathbf{x}) + a_0 z + \sum_{i=1}^m (c_i y_i + \frac{1}{2} d_i y_i^2) \quad (3.41)$$

$$\begin{aligned} \text{Subject to: } & f_i(\mathbf{x}) - a_i z - y_i \leq 0, \quad i = 1, \dots, m \\ & \mathbf{x} \in \mathbf{X}, \quad \mathbf{y} \geq \mathbf{0}, \quad z \geq 0 \end{aligned}$$

where the objective function is $f_0(\mathbf{x})$ and the $f_i(\mathbf{x})$ are constraint functions that are desired to be less than zero. The design variables are $\mathbf{x} = (x_1, x_2, \dots, x_n)$ and are contained within the set $X = \{\mathbf{x} \in \mathbb{R}^n | x_j^{\min} \leq x_j \leq x_j^{\max}, j \in \{1, \dots, n\}\}$, where the individual design variables are bounded between a predefined lower and upper bound. The set of y_i , $i = 1, \dots, m$, and the single value z are artificial variables added penalize violation of the constraints. The remaining variables are constants defined the beginning of the optimization. The c_i , $i = 1, \dots, m$, define linear constraint penalties and the d_i , $i = 1, \dots, m$, form quadratic constraint penalties. The a_i , $i = 1, \dots, m$, and z weight the relative importance of the constraints. Note that all constants must be non-negative and that for each i , at least one of the c_i and d_i must be positive to ensure that each constraint is considered.

Depending on the problem under consideration, many of the constants in Equation 3.40 may be set to zero as certain penalizations and constraints may not be needed. To adapt it to topology optimization with one equality constraint, we set $d_i = 0$, $a_0 = 0$, and $a_i = 0$ [23].

The globally convergent method of moving asymptotes (GCMMA) used here and provided by Dr. Svanberg [23] is modified from the original Method of Moving Asymptotes (MMA). The MMA approach is an iterative method that uses a linear

approximation of the objective function and constraint functions which are both written in terms of their respective gradients. The presentation below describes the GCMMA algorithm and follows the procedure described by Svanberg.

In each optimization iteration k , the moving asymptotes $u_j^{(k)}$ and $l_j^{(k)}$ must be determined and the constraint functions are approximated by

$$f_i(\mathbf{x}) \approx f_i^{(k)}(\mathbf{x}) = \sum_{j=1}^n \left(\frac{p_{ij}^{(k)}}{u_j^{(k)} - x_j} + \frac{q_{ij}^{(k)}}{x_j - l_j^{(k)}} \right) + r_i^{(k)}, \quad i = 0, 1, \dots, m \quad (3.42)$$

where values $p_{ij}^{(k)}$ and $q_{ij}^{(k)}$ are determined by

$$p_{ij}^{(k)} = \left(u_j^{(k)} - x_j^{(k)} \right)^2 * \left(1.001 \left(\frac{\partial f_i}{\partial x_j}(\mathbf{x}^{(k)}) \right)^+ + 0.001 \left(\frac{\partial f_i}{\partial x_j}(\mathbf{x}^{(k)}) \right)^- + \frac{10^{-5}}{x_j^{max} - x_j^{min}} \right) \quad (3.43)$$

$$q_{ij}^{(k)} = \left(x_j^{(k)} - l_j^{(k)} \right)^2 * \left(0.001 \left(\frac{\partial f_i}{\partial x_j}(\mathbf{x}^{(k)}) \right)^+ + 1.001 \left(\frac{\partial f_i}{\partial x_j}(\mathbf{x}^{(k)}) \right)^- + \frac{10^{-5}}{x_j^{max} - x_j^{min}} \right) \quad (3.44)$$

$$r_i^{(k)} = f_i(\mathbf{x}^{(k)}) - \sum_{j=1}^n \left(\frac{p_{ij}^{(k)}}{u_j^{(k)} - x_j^{(k)}} + \frac{q_{ij}^{(k)}}{x_j^{(k)} - l_j^{(k)}} \right) \quad (3.45)$$

In the above, the expression $\left(\frac{\partial f_i}{\partial x_j}(\mathbf{x}^{(k)}) \right)^+ = \max \left(0, \frac{\partial f_i}{\partial x_j}(\mathbf{x}^{(k)}) \right)$ and $\left(\frac{\partial f_i}{\partial x_j}(\mathbf{x}^{(k)}) \right)^- = \max \left(0, -\frac{\partial f_i}{\partial x_j}(\mathbf{x}^{(k)}) \right)$. In each iteration, move limits are placed on the

design variables which restrict them within $\alpha_j^{(k)} \leq x_j \leq \beta_j^{(k)}$ where:

$$\alpha_j^{(k)} = \max \left\{ x_j^{min}, l_j^{(k)} + 0.1(x_j^{(k)} - l_j^{(k)}), x_j^{(k)} - 0.5 * (x_j^{max} - x_j^{min}) \right\} \quad (3.46)$$

$$\beta_j^{(k)} = \min \left\{ x_j^{max}, u_j^{(k)} - 0.1(u_j^{(k)} - x_j^{(k)}), x_j^{(k)} + 0.5 * (x_j^{max} - x_j^{min}) \right\} \quad (3.47)$$

which is equivalent to restricting x_j to lie within its global bounds, allowing it to move up to 0.9 of the distance to $u_j^{(k)}$ or $l_j^{(k)}$, and allowing it to move up to half of the range $x_j^{max} - x_j^{min}$.

The asymptotes are determined in each iteration to define the new value of the design variables x_j as well as the artificial variables y_j and z . The first two iterations are used to initialize the asymptote parameters, with

$$l_j^{(k)} = x_j^{(k)} - 0.5(x_j^{max} - x_j^{min}) \quad (3.48)$$

$$u_j^{(k)} = x_j^{(k)} + 0.5(x_j^{max} - x_j^{min}) \quad (3.49)$$

On the third iteration and higher, the asymptotes are defined based on the previous iterations as

$$l_j^{(k)} = x_j^{(k)} - \gamma_j^{(k)}(x_j^{(k-1)} - l_j^{(k-1)}) \quad (3.50)$$

$$u_j^{(k)} = x_j^{(k)} + \gamma_j^{(k)}(u_j^{(k-1)} - x_j^{(k-1)}) \quad (3.51)$$

where the $\gamma_j^{(k)}$ is a constant that changes based on whether the design variable x_j has oscillated or remained monotonic in the past two iterations which is implemented through

$$\gamma_j^{(k)} = \begin{cases} 0.7 & \text{if } (x_j^{(k)} - x_j^{(k-1)})(x_j^{(k-1)} - x_j^{(k-2)}) < 0, \\ 1.2 & \text{if } (x_j^{(k)} - x_j^{(k-1)})(x_j^{(k-1)} - x_j^{(k-2)}) > 0, \\ 1 & \text{if } (x_j^{(k)} - x_j^{(k-1)})(x_j^{(k-1)} - x_j^{(k-2)}) = 0, \end{cases} \quad (3.52)$$

The purpose of the varying values of the $\gamma_j^{(k)}$ parameter is to minimize oscillating behavior. Note that the 0.7 and 1.2 values in Equation 3.51 could be adjusted, but these values have been found to work well in our optimization. Finally, the asymptotes are bounded to be between $0.01 * (x_j^{max} - x_j^{min})$ and $10 * (x_j^{max} - x_j^{min})$ away from $x_j^{(k)}$.

The GCMMA algorithm adds a separate iteration sub-loop for each step in the optimization. At each outer iteration, the objective and constraint functions are approximated by convex functions. The approximating functions are checked to determine if they are sufficiently accurate. If not, a more conservative set of approximating functions is generated iteratively in the inner loop until a sufficiently accurate set of approximating functions are found. They are then used to solve the subproblem in the current outer iteration.

It is worth observing that the method, while based on a linear approximation, is composed of several heuristic user defined parameters. This necessitates some tuning while modifying it to solve topology optimization problems. The objective function is scaled to allow it to be considered effectively relative to the magnitudes of the built-in constants by $f_0(\mathbf{x}) = 500 * f(\mathbf{x})$. There are $n = N$ design variables, where N is the number of finite elements, in the model presented above, and when both density and element orientation are considered as in Section 3.6 there are $n = 2N$ design variables. Two constraints ($m = 2$) are used to force the volume constraint to be an equality; it may be possible to tune the c_i parameters to require only one constraint to reflect the volume constraint, but for the tuning of the c_i parameters used by the authors two constraints are required. The design sensitivities are scaled by a factor of 100 for use with the user-defined parameters in the main algorithm.

3.5 Issues with the Density Method

The density method described in Section 3.1, while widely used in many popular topology optimization approaches, experiences some well-documented issues. Methods to accommodate or otherwise correct these issues for the problem are discussed below.

3.5.1 Checkerboarding

In many designs, regions of alternating solid and void elements can arise regardless of the update algorithm chosen [78]. These regions are physically meaningless, as it is impossible to manufacture this solid-void spacing. Figure 3.3 gives a structure that exhibits a large region of checkerboarding.

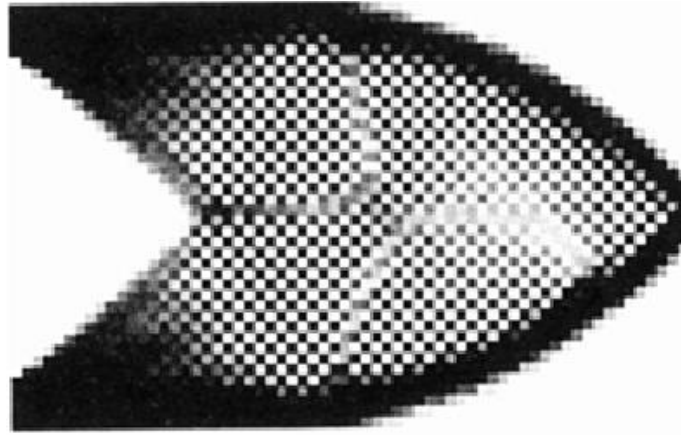


Figure 3.3: Checkerboarding in Cantilever Beam [79]

The checkerboarding behavior is due to the four-node square linear finite elements used in many finite element implementations [79]. It has been found that the alternating densities generates a material with an artificially high strength-to-weight ratio because of the finite element formulation [80]. Sigmund showed that using eight-node or nine-node square elements instead of four-node elements resolves this, at the cost of additional computational burden when solving the associated finite element problem. Using a mesh with different sized elements can also prevent checkerboarding [81], however the computational burden is increased as the efficiency of using the same local stiffness matrix for all elements is lost.

The checkerboarding problem has only been observed for linear identically sized finite element meshes, however it has been shown that a filter can be applied to the design sensitivities to avoid checkerboarding independent of the mesh [81]. Several different anti-checkerboarding filters have been proposed [82], with some PDE-based filters and some simpler weighted-average filters. Each of these filters have been shown to resolve checkerboarding, and the approach used in this work implements a minimum member size filter that replaces each sensitivity with the weighted average of all design sensitivities within a given radius, as shown in Section 4.6.3. The effects of this filter radius are investigated in Chapter 4. Note that this is identical to the filter that Sigmund uses in the 99-line Matlab code [22]. A constraint on the gradient can also prevent checkerboarding [83].

Another method of preventing checkerboarding is to add a constraint to the perimeter of the structure. This can avoid checkerboarding, and it can also resolve the mesh dependence problem [84], [85]. However, for simplicity no perimeter constraints are used in this research as satisfactory results were obtained with gradient filtering.

3.5.2 Mesh Dependence

In general, the topology optimization problem is not well-posed, meaning that no global minimum exists due to the generation of infinitely complex fractal-like structures that manifest under arbitrary levels of geometric resolution [81]. When the design space is discretized into a specific number of finite elements a minimum can be found, but there is not a guarantee that the design will resemble the final structure under a different discretization, or that the structure will eventually converge to a single result as the mesh is refined. This is a more theoretical problem, as each manufacturing method has a

maximum level of geometric resolution and there is no value in creating a mesh that is significantly finer than the level of detail that can feasibly be manufactured. The perimeter constraint methods prevent fractal behavior from manifesting at the expense of adding another constraint [84], and a Helmholtz-based differential equation filter can also generate mesh-independent results [78]. This work here does not use any filter or constraint methods to prevent mesh-dependence, as the additive manufacturing methods considered have a limited geometric resolution based on the bead size. Mesh-independence is investigated in Chapter 4, and it is shown that manipulating the minimum member size filter can prevent mesh dependence.

3.5.3 Local Minima

Both optimization algorithms considered in Sections 3.3 and 3.4 are gradient-based and thus do not guarantee convergence to the global minimum, thus allowing for the solution to be mesh dependent. This can easily be demonstrated by considering different starting points for the density values. For example, the final topologies can appear different if most of the material starts in the top half or bottom half of the structure (cf. Figure 3.10). Figure 3.4 shows two different initial density distributions for a design space that consists of half of a cantilever beam (see Figure 4.1) and the final structures obtained using the OC method. Although the final structures are similar, some differences can be noted.

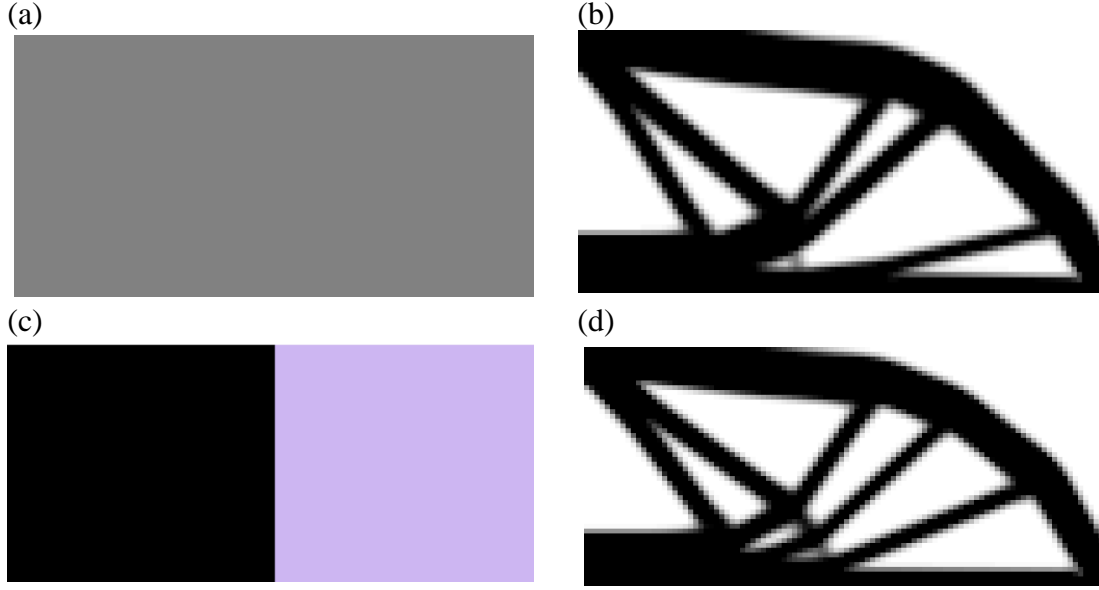


Figure 3.4: Different Initial Density Distributions and Resulting Final Structures

In Figure 3.4, image (a) shows an initial density distribution where every element density was set to $\frac{1}{2}$, and image (b) shows the final topology of the structure. Likewise, image (c) shows a different initial density distribution, where the densities on the left half were set to 1 and the densities on the right half of the design domain were set to ρ_{min} , and image (d) shows the final structure. The design domain considered was half of a beam in three-point bending.

The lack of a guarantee that the result obtained is the global minimum is a limitation inherent in all gradient-based methods, and while approaches like the genetic algorithm offer some probability of escaping local minima, those methods cannot be easily incorporated with the OC or GCMMA approaches. It can be observed that in the examples in Figure 3.4, although the final structures are different the final compliance values are extremely similar. The similar performance of local minima derived from topology optimization indicates that, although the structures are different, many of the

local minima have similar objective function values. It cannot be proven that the obtained structure is near the global minimum but running several simulations with different initial conditions can indicate that the results are “good enough” and converge to near-identical structures. Thus, the current approaches are utilized with the knowledge that the results are not likely the global optimum but are likely to be reasonably close.

3.6 Anisotropic Material Model

3.6.1 Methods for Anisotropic Topology Optimization

This work models the performance of fiber-reinforced polymer composite parts produced by additive manufacturing polymer deposition where material microstructure is highly aligned in the print direction. To account for the direction of material orientation, we consider a second design variable associated with each finite element to represent a preferred orientation of the bead material. The material is assumed to be orthotropic, with an orientation parameter treated as a design variable defining the direction of maximum stiffness. Various topology optimization update methods have been considered in the literature, some of which offer insights into the development of a robust approach for the research presented here. This includes material orientation in a SIMP-based topology optimization approach has been done in two-dimensional systems [59] for compliance optimization, where the topology of the part defined by element densities considered to be held constant. We consider an orientation optimization approach that includes computations performed independent of the density update at each optimization iteration for the OC method. Modifications to the OC method described above are presented as the standard OC approach is tailored specifically for optimization of isotropic systems. The

density and orientation optimization can be performed simultaneously, however, optimal orientation can also be performed through local optimization on the element level, allowing for a natural separation from the OC topology optimization solution. The modeling approach employed here follows the Solid Orthotropic Method with Penalization [67] which formed the basis for prior works by Jiang, Hoglund, and Smith [63].

3.6.2 Formulation of Material Model

Anisotropy is introduced to the elasticity problem in Equation 3.21 and the topology optimization problem in Equation 3.27 by assigning each finite element an orientation design variable θ_i that defines the material orientation of the element. This orientation is an angle between 0 and π radians that represents which direction maximum stiffness occurs within the element. Note that it is not necessary to consider a full 0 to 2π range of values for θ_i because the element is orthotropic and is thus symmetric under a rotation of π . Also, the material orientations are considered via modular arithmetic to be cyclic modulo π , which means that not only does an element rotated $\frac{\pi}{4}$ behave identically to an element rotated $\frac{5\pi}{4}$ or $\frac{9\pi}{4}$, all of the orientations of the form $\theta_i = a * \pi + b$, where $b \in [0, \pi)$ and $a \in \mathbb{Z}$ are considered to be the same value. This resolves the uniqueness issue in that explicit bounds are not applied to the element orientations, but each orientation generates a unique elemental stiffness matrix.

It is assumed that each element has a local $E_y \neq E_x$, and that the Young's Moduli are identical for all elements but can be rotated according to the element's orientation θ_i . To accommodate material orientation, the elemental stiffness matrices are defined in

terms of the material matrix D_M that reflects the anisotropic material in two dimensions, written as

$$\mathbf{D}_M = \begin{bmatrix} \frac{E_x}{1 - \nu_{xy}\nu_{yx}} & \frac{\nu_{xy}E_y}{1 - \nu_{xy}\nu_{yx}} & 0 \\ \frac{\nu_{xy}E_y}{1 - \nu_{xy}\nu_{yx}} & \frac{E_y}{1 - \nu_{xy}\nu_{yx}} & 0 \\ 0 & 0 & G_{xy} \end{bmatrix} \quad (3.53)$$

where ν_{xy} and ν_{yx} are the Poisson's ratios in the corresponding local rotated element $x - y$ coordinate system. Note that when the material within a finite element is not rotated (i.e. $\theta_i = 0$), the element has a Young's Modulus of $E_x = E_{x'}$ and $E_y = E_{y'}$, where the $x' - y'$ coordinate system denotes the global coordinate system. The orientation of the $x - y$ local material axes are defined through the element orientation θ_i which requires that the finite element stiffness matrix in Equation 3.19 be modified as

$$\mathbf{K}_{Mi}^e = \rho_i^p \int_{V_i} \mathbf{B}_M^T \mathbf{R}^T(\theta_i) \mathbf{D}_M \mathbf{R}(\theta_i) \mathbf{B}_M dV_i \quad (3.54)$$

where the subscript M is included to denote that this is the stiffness matrix for the mechanical system, as opposed to the thermal system discussed below. Here, \mathbf{B}_M is the mechanical displacement gradient matrix (which is the same \mathbf{B} in Equation 3.17).

The two-dimensional rotation tensor \mathbf{R} is employed to rotate the material matrix in Equation 5.54 from the local rotated material coordinate system into the global material coordinate system. The rotation tensor \mathbf{R} is a function of the elemental orientation angle θ_i alone, and is written as

$$\mathbf{R}(\theta_i) = \begin{bmatrix} \cos^2(\theta_i) & \sin^2(\theta_i) & -2 * \sin(\theta_i) * \cos(\theta_i) \\ \sin^2(\theta_i) & \cos^2(\theta_i) & 2 * \sin(\theta_i) * \cos(\theta_i) \\ \sin(\theta_i) * \cos(\theta_i) & -\sin(\theta_i) * \cos(\theta_i) & \cos^2(\theta_i) - \sin^2(\theta_i) \end{bmatrix} \quad (3.55)$$

For an orthotropic material model with orientation given by θ_i in each element i , the compliance of the overall structure becomes a function of the elemental densities and element orientations. Both densities and orientations are treated as design variables, which can be reflected in the objective function written as

$$C(\boldsymbol{\rho}, \boldsymbol{\theta}) = \mathbf{U}(\boldsymbol{\rho}, \boldsymbol{\theta})^T \mathbf{F}(\boldsymbol{\rho}, \boldsymbol{\theta}) \quad (3.56)$$

where $\boldsymbol{\rho}$ and $\boldsymbol{\theta}$ are the global matrices of the element densities and orientation design variables, respectively.

3.6.3 Optimization of Anisotropic Material Orientation

Many orientation optimization approaches use stress or strain-based formulations to determine the optimal set of orientations, as minimizing stress or strain tends to minimize compliance in the case when only mechanical loading is applied. However, more objective functions will be considered than mechanical compliance in this research, so a more general gradient-based approach is utilized. The design sensitivities of compliance with respect to element orientations can be determined by the adjoint variable method as used above to yield the following formulation, written for element i as

$$\frac{dC}{d\theta_i} = \rho_i^p * \mathbf{U}_i^T * \frac{d\mathbf{K}_{Mi}}{d\theta_i} * \mathbf{U}_i \quad (3.57)$$

The sensitivity of the local stiffness matrices with respect to the corresponding orientation angle design variable θ_i can be determined with the chain rule

$$\frac{d\mathbf{K}_{Mi}}{d\theta_i} = x_i^p \int_{V_i} 2 * \mathbf{B}_M^T \frac{d\mathbf{R}^T}{d\theta_i}(\theta_i) \mathbf{D}_M \mathbf{R}(\theta_i) \mathbf{B}_M dV_i \quad (3.58)$$

for symmetric \mathbf{D}_M . The derivative of the rotation matrix is readily obtained from Equation 3.55 as

$$\frac{d\mathbf{R}(\theta_i)}{d\theta_i} = \begin{bmatrix} -2 * \cos(\theta_i) * \sin(\theta_i) & 2 * \sin(\theta_i) * \cos(\theta_i) & -2 * \cos^2(\theta_i) + 2 * \sin^2(\theta_i) \\ 2 * \sin(\theta_i) * \cos(\theta_i) & -2 * \sin(\theta_i) * \cos(\theta_i) & 2 * \cos^2(\theta_i) - 2 * \sin^2(\theta_i) \\ \cos^2(\theta_i) - \sin^2(\theta_i) & -\cos^2(\theta_i) + \sin^2(\theta_i) & -4 * \sin(\theta_i) * \cos(\theta_i) \end{bmatrix} \quad (3.59)$$

The GCMMA method is capable of optimizing both the element densities and orientations using the gradient, but the OC method was designed to optimize over element densities alone. Therefore, when the optimality criterion method is used, a separate method must be used to optimize the element orientations. This method, described below, is conducted in parallel with the OC update step.

Each element orientation is considered individually. The associated local displacements \mathbf{U}_i can be determined from the finite element equilibrium, and the element-level compliance can be computed as

$$c_i = \rho_i^p \mathbf{U}_i^T \mathbf{K}_{M_i}(\theta_i) \mathbf{U}_i \quad (3.60)$$

The elemental compliance can be treated as the objective function in a one-dimensional optimization with the elemental orientation θ_i as the only design variable. We employ Newton's method to optimize Equation 3.60. Note that, although global compliance is minimized in Equation 3.28, the element-level compliance in Equation 3.60, written as a function of known fixed displacements \mathbf{U}_i , is maximized. In the formulation used for the entire structure, no nonzero displacements are applied in any of the loading scenarios considered. Our approach is similar to that documented in [86] which shows that when fixed nonzero displacements are applied, those displacements should be considered separately as a maximization problem.

Newton's method yields the optimal elemental orientation θ_{opt_i} for each element independently under a known fixed displacement field. Considering the elements individually neglects the coupled effects of the element orientation on the displacement

field, so the orientations determined by the independent optimizations are not necessarily the globally optimal orientations for the given loading. However, a sufficiently small changes to an element's orientation is assumed to have negligible effects on the displacements of the structure obtained by the finite element analysis. Thus, the orientations are not set to the locally optimal values determined but are moved toward those values

$$\theta_{i_{new}} = \begin{cases} \theta_i - m & , \theta_{opt_i} < \theta_i - m \\ \theta_{opt_i} & , |\theta_{opt_i} - \theta_i| \leq m \\ \theta_i + m & , \theta_{opt_i} > \theta_i + m \end{cases} \quad (3.61)$$

where the move limit of m is implemented to ensure that the change in orientation values is sufficiently small. In our work, this limit is set to be $m = 0.1 * |\theta_{i_{new}} - \theta_i|$. Recall that the element orientations are considered modulo π so that no bounds are needed.

In plotting, the elemental orientations can be represented as a vector showing the orientation at each element. Figure 3.5 demonstrates how the element orientations can be displayed with the densities.

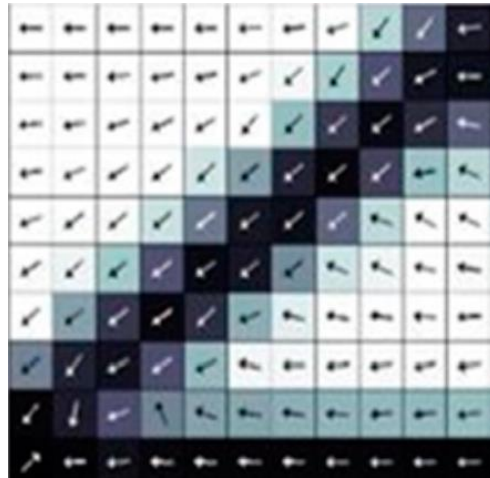


Figure 3.5: Example Element Orientations [63]

3.7 Weakly Coupled Thermomechanical Systems

Optimizing structures under thermal loading has been considered for many applications, such as heat fins to exhaust-washed structures. The additive manufacturing process often involves significant transient thermal loading during the material deposition process, particularly in polymer extrusion deposition as polymer is extruded in a melted state and experiences thermal stresses as it cools to the ambient temperature. To the best of our knowledge, no research has considered coupling a transient thermal history with mechanical loading, and this work does not seek to fill that gap. A simpler system is considered within a topology optimization process instead, with steady state thermal loading that advances the state-of-the-art toward modeling the full transient system. Steady-state thermal loading has been modeled before, but the design-dependent temperature field and weakly coupled thermal loading used here have not yet been considered.

3.7.1 Weakly Coupled Model

The conduction heat transfer is modeled by the Poisson equation in two dimensions, modified to allow for anisotropic heat conduction properties, to describe the temperature field T

$$\frac{\partial}{\partial x} \left(k_x \frac{\partial T}{\partial x} \right) + \frac{\partial}{\partial y} \left(k_y \frac{\partial T}{\partial y} \right) + g(x, y) = 0 \quad (3.62)$$

Where the heat flux g and the conductivities k_x and k_y in the global x – and y – directions, respectively, can be spatially varying. The strong form in Equation 3.62 can be converted into a weak form by integrating over an arbitrary domain Ω_e with boundary Γ_e and arbitrary weighting function w which may be written as

$$\int_{\Omega_e} \frac{\partial w}{\partial x} k_x \frac{\partial T}{\partial x} + \frac{\partial w}{\partial y} k_y \frac{\partial T}{\partial y} - w g \, dx \, dy - \oint_{\Gamma_e} w \left(n_x k_x \frac{\partial T}{\partial x} + n_y k_y \frac{\partial T}{\partial y} \right) ds \quad (3.63)$$

In the boundary integral over boundary edges Γ_e , n_x and n_y are the direction cosines of the unit normal vector. The weak form can then be discretized across a set of finite elements to generate the finite element equilibrium. Note that the expression $q_n = n_x k_x \frac{\partial T}{\partial x} + n_y k_y \frac{\partial T}{\partial y}$ is a prescribed boundary heat flux.

The discretization process can be done for a general element in a similar manner to the discretization of the mechanical elasticity weak form above. The temperature can be approximated over the element by using the nodal temperatures T_j^e and a series of interpolation functions $\psi_j^e(x, y)$, which must be at least bilinear. For an n -noded finite element, the temperature T is approximated as

$$T(x, y) \approx \sum_{j=1}^n T_j^e \psi_j^e(x, y) \quad (3.64)$$

Equation 3.64 can be substituted into the weak form (Equation 3.63), which yields the discretized equilibrium equation

$$\mathbf{K}_{Th}^e \mathbf{T}^e = \mathbf{F}_{Th}^e \quad (3.65)$$

with

$$\mathbf{K}_{Th}^e = \int_{\Omega_e} \mathbf{B}_{Th}^T \mathbf{D}_{Th} \mathbf{B}_{Th} d\Omega_e \quad \mathbf{F}_{Th}^e = \int_{\Omega_e} f \boldsymbol{\Psi}^e d\Omega_e + \oint_{\Gamma_e} q_n^e \boldsymbol{\Psi}^e d\Gamma_e \quad (3.66)$$

The thermal gradient matrix \mathbf{B}_{Th} can be expressed in terms of the interpolation functions as

$$\mathbf{B}_{Th} = \begin{bmatrix} \frac{\partial \psi_1}{\partial x} & \frac{\partial \psi_2}{\partial x} & \cdots & \frac{\partial \psi_n}{\partial x} \\ \frac{\partial \psi_1}{\partial y} & \frac{\partial \psi_2}{\partial y} & \cdots & \frac{\partial \psi_n}{\partial y} \\ 0 & 0 & \cdots & 0 \end{bmatrix} \quad (3.67)$$

and the elemental thermal elasticity matrix \mathbf{D}_{Th} can be written in terms of the material properties of the system in \mathbf{D}_{Th_0} as

$$\mathbf{D}_{Th} = \rho_i^p \mathbf{T}^T(\theta_i) \mathbf{D}_{Th_0} \mathbf{T}(\theta_i) \quad (3.68)$$

where

$$\mathbf{D}_{Th_0} = \begin{bmatrix} K_x & 0 & 0 \\ 0 & K_y & 0 \\ 0 & 0 & 0 \end{bmatrix} \quad (3.69)$$

The rotation tensor \mathbf{T} is the standard rotation tensor in two dimensions.

$$\mathbf{T} = \begin{bmatrix} \cos(\theta_i) & -\sin(\theta_i) & 0 \\ \sin(\theta_i) & \cos(\theta_i) & 0 \\ 0 & 0 & 1 \end{bmatrix} \quad (3.70)$$

The default anisotropic thermal conductivity matrix is written in terms of the anisotropic coefficients of conduction K_x and K_y , and the penalty parameter p is the same as that used in the mechanical analysis above. The conduction coefficient of each element is initially assumed to be K_x and K_y in the global x and y directions. The element orientation θ_i represents a rotation of these properties to the $x' - y'$ elemental coordinate system.

The elemental thermal conductivity matrices are functions of the elemental density and orientation in a similar manner to the mechanical stiffness matrices, which can be shown by substituting Equations 3.67 and 3.68 into Equations 3.65 and 3.66 as [87]

$$\mathbf{K}_{Th_i} = \rho_i^p \int_{V_i} \mathbf{B}_{Th}^T \mathbf{T}^T(\theta_i) \mathbf{D}_{Th_0} \mathbf{T}(\theta_i) \mathbf{B}_{Th} dV_i \quad (3.71)$$

The global thermal conductance matrix is evaluated from the integral in Equation 3.70 using two-point Gauss quadrature. Note that the anisotropic material properties in

the thermal model generated an elemental conductance matrix with comparable structure to the anisotropic mechanical stiffness matrix discussed in Section 3.6.

Here, the thermal finite element equilibrium is defined across the design domain using the same finite elements as the mechanical equilibrium. It could be discretized using any finite element mesh, but if the same discretization is used, it is not necessary to map the temperature field from one mesh to another. The thermal discretization also uses square linear finite elements, but each node has only one degree of freedom. The global thermal equilibrium is linear.

Boundary temperatures and heat fluxes are defined, and the thermal equilibrium is solved for the global temperature vector. The temperature vector is used to determine thermal stresses within each element [88]

$$\mathbf{F}_{TEi} = \rho_i^p \int_{V_i} \mathbf{B}_M^T \mathbf{R}^T(\theta_i) \mathbf{D}_M \mathbf{R}(\theta_i) \begin{Bmatrix} \alpha_x \\ \alpha_y \\ \alpha_{xy} \end{Bmatrix} \Psi^e(\Delta T)_i dV_i \quad (3.72)$$

The thermal expansion behavior is orthotropic, so coefficients of thermal expansion $\alpha_{x'}$ and $\alpha_{y'}$ are the coefficients of thermal expansion parallel and perpendicular to the element orientation respectively. Note that the coefficients of thermal expansion must be rotated from the local elemental coordinate system to the global coordinate system using the rotation

$$\begin{bmatrix} \alpha_x & \alpha_{xy} & 0 \\ \alpha_{xy} & \alpha_y & 0 \\ 0 & 0 & 0 \end{bmatrix} = \mathbf{T}^T(\theta_i) \begin{bmatrix} \alpha_{x'} & 0 & 0 \\ 0 & \alpha_{y'} & 0 \\ 0 & 0 & 0 \end{bmatrix} \mathbf{T}(\theta_i) \quad (3.73)$$

The elemental thermal forces are summed in the mechanical force vector along with the applied mechanical forces. The mechanical equilibrium is then solved for displacements.

3.7.2 Design Sensitivity Derivation

The design sensitivities must be computed for the coupled system, as the force vector is dependent on the temperatures and densities when the structure is under the influence of the thermal loading. The adjoint variable method can be used once again in a similar manner to the above derivation, with the only difference coming from the coupled nature of the thermomechanical problem. Compliance is defined as earlier

$$C = \mathbf{U}^T \mathbf{F}$$

The augmented compliance can be written in terms of an arbitrary Lagrange multiplier λ

$$\hat{C} = C - \lambda(\mathbf{KU} - \mathbf{F}) \quad (3.74)$$

Then, the design sensitivity can be computed with the chain rule

$$\begin{aligned} \frac{D\hat{C}}{D\rho_i} &= \frac{D}{D\rho_i}(C) - \lambda \frac{D}{D\rho_i}(\mathbf{KU} - \mathbf{F}) = \\ &= \frac{dC}{d\mathbf{U}} \frac{D\mathbf{U}}{D\rho_i} + \frac{dC}{d\mathbf{F}} \frac{D\mathbf{F}}{D\rho_i} - \lambda \left(\frac{D\mathbf{K}}{D\rho_i} \mathbf{U} + \mathbf{K} \frac{D\mathbf{U}}{D\rho_i} - \frac{D\mathbf{F}}{D\rho_i} \right) \end{aligned} \quad (3.75)$$

It is desired that the $\frac{D\mathbf{U}}{D\rho_i}$ term be eliminated, so all terms involving it are collected.

Equation 3.75 can be rewritten as

$$\frac{D\hat{C}}{D\rho_i} = \left(\frac{dC}{d\mathbf{U}} - \lambda \mathbf{K} \right) \frac{D\mathbf{U}}{D\rho_i} + \left(\frac{dC}{d\mathbf{F}} + \lambda \right) \frac{D\mathbf{F}}{D\rho_i} - \lambda \frac{D\mathbf{K}}{D\rho_i} \mathbf{U} \quad (3.76)$$

By definition of compliance, Equation 3.76 can be written in terms of the finite element variables

$$\frac{D\hat{C}}{D\rho_i} = (\mathbf{F} - \lambda \mathbf{K}) \frac{D\mathbf{U}}{D\rho_i} + (\mathbf{U}^T + \lambda) \frac{D\mathbf{F}}{D\rho_i} - \lambda \frac{D\mathbf{K}}{D\rho_i} \mathbf{U} \quad (3.77)$$

Let $\lambda = \mathbf{U}^T$. Then, the $\frac{DU}{D\rho_i}$ term can be eliminated, as $\mathbf{F} - \lambda\mathbf{K} = \mathbf{0}$. The force derivative term is more complex now, as the force vector is a function of the densities and the temperature field. Equation 3.77 can be written as

$$\frac{D\hat{C}}{D\rho_i} = 2\mathbf{U}^T \frac{D\mathbf{F}}{D\rho_i} - \mathbf{U}^T \frac{D\mathbf{K}}{D\rho_i} \mathbf{U} = 2\mathbf{U}^T \left(\frac{\partial \mathbf{F}}{\partial \rho_i} + \frac{\partial \mathbf{F}}{\partial \mathbf{T}} \frac{D\mathbf{T}}{D\rho_i} \right) - \mathbf{U}^T \frac{D\mathbf{K}}{D\rho_i} \mathbf{U} \quad (3.78)$$

Now, $\mathbf{K}_{Th}\mathbf{T} = \mathbf{F}_{Th}$ by the thermal finite element equilibrium, and differentiating yields $\frac{D\mathbf{K}_{Th}}{D\rho_i} \mathbf{T} + \mathbf{K}_{Th} \frac{D\mathbf{T}}{D\rho_i} = \frac{D\mathbf{F}_{Th}}{D\rho_i}$, which can be reordered as $\frac{D\mathbf{T}}{D\rho_i} = \mathbf{K}_{Th}^{-1} \left(\frac{D\mathbf{F}_{Th}}{D\rho_i} - \frac{D\mathbf{K}_{Th}}{D\rho_i} \mathbf{T} \right)$.

Then,

$$\frac{D\hat{C}}{D\rho_i} = 2\mathbf{U}^T \left(\frac{\partial \mathbf{F}}{\partial \rho_i} - \frac{\partial \mathbf{F}}{\partial \mathbf{T}} \mathbf{K}_{Th}^{-1} \frac{D\mathbf{K}_{Th}}{D\rho_i} \mathbf{T} \right) - \mathbf{U}^T \frac{D\mathbf{K}}{D\rho_i} \mathbf{U} \quad (3.79)$$

Equation 3.79 can be discretized across the elements in Equation 3.80. Other finite element choices will generate different discretizations, and while the derivation ending in Equation 3.79 is general, the discretized equation is only valid for the square linear elements used here. Note that the global \mathbf{K}_{Th} matrix is singular, but the inverse of the sub-matrix composed of the free degrees of freedom of \mathbf{K}_{Th} can be found, and this is substituted where \mathbf{K}_{Th}^{-1} is required.

$$\begin{aligned} \frac{DC}{D\rho_i} = & -p\rho_i^{p-1} \mathbf{U}_i^T \mathbf{K}_{Mi} \mathbf{U}_i + 2\mathbf{U}_i^T \frac{\partial \mathbf{F}_{TE}}{\partial \rho_i} - \\ & 2p\rho_i^{p-1} \mathbf{U}_i^T \left(\frac{\partial \mathbf{F}_{TE}}{\partial \mathbf{T}} \mathbf{K}_{Th}^{-1} \right)_i \mathbf{K}_{Thi} \mathbf{T}_i \end{aligned} \quad (3.80)$$

Equation 3.80 is the expression used for the design sensitivity. The two partial derivative terms can be evaluated in terms of the integration expression of the thermal force vector by using the finite element discretization considered above.

$$\frac{\partial \mathbf{F}_{TE}}{\partial \rho_i} = p\rho_i^{p-1} \int_{V_i} \mathbf{B}_M^T \mathbf{R}^T(\theta_i) \mathbf{D}_{Th} \mathbf{R}(\theta_i) \begin{Bmatrix} \alpha_x \\ \alpha_y \\ \alpha_{xy} \end{Bmatrix} \Psi^e(\Delta \mathbf{T})_i dV_i \quad (3.81)$$

$$\frac{\partial \mathbf{F}_{TEi}}{\partial \mathbf{T}_i} = \rho_i^p \int_{V_i} \mathbf{B}_M^T \mathbf{R}^T(\theta_i) \mathbf{D}_{Th} \mathbf{R}(\theta_i) \begin{Bmatrix} \alpha_x \\ \alpha_y \\ \alpha_{xy} \end{Bmatrix} N_i dV_i \quad (3.82)$$

Equations 3.81 and 3.82 are evaluated with two-point Gauss quadrature.

Similarly, the design sensitivity of compliance with respect to the orientations can be computed. A similar manner is used, and the derivation proceeds in a nearly identical manner.

$$\begin{aligned} \frac{dC}{d\theta_i} = & -\rho_i^p \mathbf{U}_i^T \frac{\partial \mathbf{K}_{Mi}}{\partial \theta_i} \mathbf{U}_i + 2 \mathbf{U}_i^T \frac{\partial \mathbf{F}_{TH}}{\partial \theta_i} \\ & - 2 \rho_i^p \mathbf{U}_i^T \frac{\partial \mathbf{F}_{TEi}}{\partial \mathbf{T}_i} (\mathbf{K}_{Th}^{-1})_i \frac{\partial \mathbf{K}_{Thi}}{\partial \theta_i} \mathbf{T}_i \end{aligned} \quad (3.83)$$

The individual partial derivatives can be computed in terms of their integral expressions, which are all evaluated with two-point Gauss quadrature. Note that Equation 3.83 is a general expression of the design sensitivity, and that Equations 3.84 – 3.86 are all discretizations based on the finite element formulation used.

$$\frac{\partial \mathbf{F}_{TE}}{\partial \theta_i} = \rho_i^p \int_{V_i} 2 \mathbf{B}_{Th}^T \frac{\partial \mathbf{R}^T(\theta_i)}{\partial \theta_i} \mathbf{D}_{Th} \begin{Bmatrix} \alpha_x \\ \alpha_y \\ \alpha_{xy} \end{Bmatrix} (\Delta T)_i dV_i \quad (3.84)$$

$$\frac{\partial \mathbf{K}_{Thi}}{\partial \theta_i} = \rho_i^p \int_{V_i} 2 \mathbf{B}_{Th}^T \frac{\partial \mathbf{R}^T(\theta_i)}{\partial \theta_i} \mathbf{D}_{Th} \mathbf{R}(\theta_i) \mathbf{B}_{Th} dV_i \quad (3.85)$$

$$\frac{\partial \mathbf{K}_{Mi}}{\partial \theta_i} = \rho_i^p \int_{V_i} 2 \mathbf{B}_M^T \frac{\partial \mathbf{R}^T(\theta_i)}{\partial \theta_i} \mathbf{D}_M \mathbf{R}(\theta_i) \mathbf{B}_M dV_i \quad (3.86)$$

3.7.3 Sensitivity Filters for Compliance Optimization

The design sensitivity of compliance with respect to density takes exclusively negative values in purely mechanical systems. However, under weakly coupled thermomechanical loading the design sensitivities can be positive. When thermal loading is zero, increasing an element's density will always increase the part's overall stiffness.

However, when thermal loading is included, an increase in density can increase the thermal loading that an element experiences, which in elements with high temperature changes and low mechanical loads can decrease the stiffness of the part.

This presents no problem for the GCMMA algorithm, as it is a general optimization algorithm, but the OC method assumes that all design sensitivities are negative. The heuristic update scheme was not designed with positive-sign sensitivities in mind and cannot effectively operate on them. Any element with a positive design sensitivity will cause its density to be reduced by the maximum allowable amount, subject to move limits and boundary conditions. This can cause difficulties with convergence as elements may alternate between positive and negative sensitivities in subsequent operations. If a significant number of the elements have positive sensitivities, the OC method may fail to operate as all elements with positive sensitivities are treated identically and enough material may be removed to prevent a λ value from being found.

The solution implemented in this work operates on the design derivatives to map any positive derivatives into negative ones while preserving the relative ordering of the design sensitivities. There are several ways that this mapping could occur, and this work considers a family of mappings of the following form

$$\frac{dC}{dx_i}|_{new} = \begin{cases} \frac{dC}{dx_i}, & \frac{dC}{dx_i} < 0 \\ f\left(\frac{dC}{dx_i}\right), & \frac{dC}{dx_i} \geq 0 \end{cases} \quad (3.87)$$

The mapping function $f\left(\frac{dC}{dx_i}\right)$ can take many forms, and several different ones were considered. The relative performance of mapping functions will be evaluated in Section 4. The function used by default is displayed in Equation 3.87, and unless stated otherwise it is used

$$f\left(\frac{dC}{dx_i}\right) = 0 \quad (3.88)$$

This mapping function alters the design sensitivities minimally, hence its choice as the default mapping.

3.8 Strain Energy Optimization

3.8.1 Motivation

In weakly coupled thermomechanical systems minimizing compliance may not necessarily maximize the stiffness of a part. The strain energy of the part has been considered as a different objective function [77], [47]. The strain energy is equal to the compliance in pure mechanical loading, and the two diverge as thermal loading increases. Some work [47] indicates that optimizing strain energy yields a lower maximum von Mises stress than optimizing compliance, but this was only compared for isothermal systems. The relative performance of compliance and strain energy as objective functions will be evaluated in Chapter 4.

3.8.2 Definition and Sensitivity Derivation

The strain energy can be written in terms of the global finite element variables as follows

$$S = \frac{1}{2} \mathbf{U}^T \mathbf{F} - \mathbf{U}^T \mathbf{F}_{TE} + \frac{1}{2} \mathbf{U}_{TE}^T \mathbf{F}_{TE} \quad (3.89)$$

Note that the thermal effects can be considered by examining the global thermal force vector \mathbf{F}_{TE} as a separate loading case, yielding $\mathbf{K} \mathbf{U}_{TE} = \mathbf{F}_{TE}$, where \mathbf{U}_{TE} is the global displacement vector due to thermal loading. Previous works have used a different definition of strain energy, where the third term is written in terms of thermal strains

$$S = \frac{1}{2} \mathbf{U}^T \mathbf{F} - \mathbf{U}^T \mathbf{F}_{TE} + \frac{1}{2} \int_{\Omega} (\boldsymbol{\varepsilon}_{th})^T \mathbf{B} \boldsymbol{\varepsilon}_{th} dV \quad (3.90)$$

All previous works involving strain energy have only investigated isothermal systems. In that case, a structure under a uniform temperature change experiences thermal expansion that can be computed elementwise, as the structure expands or contracts uniformly. This is free expansion, as the thermal expansion of the structure as a whole can be considered as the sum of elementwise expansions.

However, under non-isothermal temperature fields, whether design dependent as used here or not, free expansion does not occur. The elementwise thermal strains do not necessarily cause a uniform expansion, as uneven elemental expansion generates additional stresses within the structure. This set of additional strains ensures that, even separate from the mechanical constraints, the elementwise thermal expansion does not fully represent the unconstrained expansion. Put another way, the sum of the elementwise thermal expansions is not equal to the total mechanically unconstrained expansion of the structure.

In all loading cases considered in Section 4, the mechanical fixed degrees of freedom do not constrain the expansion of the structure, so the formulations in Equations 3.89 and 3.90 are equivalent if the thermal strain is computed from the mechanically unconstrained expansion of the entire structure. In cases where more mechanical constraints are applied, the two would not be equal as mechanically fixing different points in the structure may require additional loading from the unconstrained expansion. This additional loading has been considered [77], and those stresses classified as mechanical stresses when they are nonzero.

It is worth noting that here the stresses generated by thermal unconstrained expansion in addition to the elementwise stresses are considered part of the overall thermal stresses and are used when computing thermal displacements. Assigning these stresses to the thermal analysis instead of the mechanical stresses was a choice of the authors, as no precedent for this was found and these stresses arise before any mechanical displacements and forces are applied. It would be possible to define the thermal stresses as only accounting for the elementwise expansion and classifying all other stresses as mechanical. This would change the definition and sensitivity of strain energy and generate different structures. Only the thermal classification is used here, but future researchers could investigate this alternate formulation.

The design sensitivity derivation for strain energy takes the same form as previous design sensitivity derivations, but two Lagrange multipliers must be used. An augmented definition of the strain energy can be expressed with the two Lagrange multipliers η and γ

$$\hat{S} = S - \lambda(KU - F) - \gamma(KU_{TE} - F_{TE}) \quad (3.91)$$

The total derivative can be taken with respect to an arbitrary element density ρ_i

$$\frac{D\hat{S}}{D\rho_i} = \frac{DS}{D\rho_i} - \lambda \frac{D}{D\rho_i} (KU - F) - \gamma (KU_{TE} - F_{TE}) \quad (3.92)$$

Using the definition of strain energy, Equation 3.92 can be expressed in terms of the global displacements and forces

$$\begin{aligned} \frac{D\hat{S}}{D\rho_i} = & \frac{dS}{d\mathbf{U}} \frac{D\mathbf{U}}{D\rho_i} + \frac{dS}{d\mathbf{F}} \frac{D\mathbf{F}}{D\rho_i} + \frac{dS}{d\mathbf{U}_{TE}} \frac{D\mathbf{U}_{TE}}{D\rho_i} + \frac{dS}{d\mathbf{F}_{TE}} \frac{D\mathbf{F}_{TE}}{D\rho_i} \\ & - \lambda \left(\frac{DK}{D\rho_i} \mathbf{U} + \mathbf{K} \frac{D\mathbf{U}}{D\rho_i} - \frac{d\mathbf{F}}{d\rho_i} \right) - \\ & \gamma \left(\frac{DK}{D\rho_i} \mathbf{U}_{TE} + \mathbf{K} \frac{D\mathbf{U}_{TE}}{D\rho_i} - \frac{D\mathbf{F}_{TE}}{D\rho_i} \right) \end{aligned} \quad (3.93)$$

Equation 3.93 can be reordered, as once again it is desired that the $\frac{DU}{D\rho_i}$ term be eliminated. The $\frac{DU_{TE}}{D\rho_i}$ term is also grouped, as it will be eliminated because it is also computationally intensive to evaluate.

$$\begin{aligned} \frac{D\hat{S}}{D\rho_i} = & \left(\frac{dS}{d\mathbf{U}} - \lambda \mathbf{K} \right) \frac{D\mathbf{U}}{D\rho_i} + \left(\frac{dS}{d\mathbf{U}_{TE}} - \gamma \mathbf{K} \right) \frac{D\mathbf{U}_{TE}}{D\rho_i} + \left(\frac{dS}{d\mathbf{F}} + \lambda \right) \frac{D\mathbf{F}}{D\rho_i} \\ & + \left(\frac{dS}{d\mathbf{F}_{TE}} + \gamma \right) \frac{D\mathbf{F}_{TE}}{D\rho_i} - \lambda \frac{D\mathbf{K}}{D\rho_i} \mathbf{U} - \gamma \frac{D\mathbf{K}}{D\rho_i} \mathbf{U}_{TE} \end{aligned} \quad (3.94)$$

The definition of strain energy yields

$$\begin{aligned} \frac{D\hat{S}}{D\rho_i} = & \left(\frac{1}{2} \mathbf{F} - \mathbf{F}_{TE} - \lambda \mathbf{K} \right) \frac{D\mathbf{U}}{D\rho_i} + \left(\frac{1}{2} \mathbf{F}_{TE} - \gamma \mathbf{K} \right) \frac{D\mathbf{U}_{TE}}{D\rho_i} + \left(\frac{1}{2} \mathbf{U}^T + \lambda \right) \frac{D\mathbf{F}}{D\rho_i} \\ & + \left(-\mathbf{U}^T + \frac{1}{2} \mathbf{U}_{TE}^T + \gamma \right) \frac{D\mathbf{F}_{TE}}{D\rho_i} - \lambda \frac{D\mathbf{K}}{D\rho_i} \mathbf{U} - \gamma \frac{D\mathbf{K}}{D\rho_i} \mathbf{U}_{TE} \end{aligned} \quad (3.95)$$

Choose $\lambda = \frac{1}{2} \mathbf{U}^T - \mathbf{U}_{TE}^T$ and $\gamma = \frac{1}{2} \mathbf{U}_{TE}^T$. Then, the first two terms simplify to zero, eliminating the $\frac{DU}{D\rho_i}$ and $\frac{DU_{TE}}{D\rho_i}$ terms as needed.

$$\begin{aligned} \frac{D\hat{S}}{D\rho_i} = & \left(\frac{1}{2} \mathbf{U}^T + \frac{1}{2} \mathbf{U}^T - \mathbf{U}_{TE}^T \right) \frac{D\mathbf{F}}{D\rho_i} + \left(-\mathbf{U}^T + \frac{1}{2} \mathbf{U}_{TE}^T + \frac{1}{2} \mathbf{U}_{TE}^T \right) \frac{D\mathbf{F}_{TE}}{D\rho_i} - \left(\frac{1}{2} \mathbf{U}^T \right. \\ & \left. - \mathbf{U}_{TE}^T \right) \frac{D\mathbf{K}}{D\rho_i} \mathbf{U} - \frac{1}{2} \mathbf{U}_{TE}^T \frac{D\mathbf{K}}{D\rho_i} \mathbf{U}_{TE} \end{aligned} \quad (3.96)$$

Note that $\frac{D\mathbf{F}}{D\rho_i} = \frac{D\mathbf{F}_{TE}}{D\rho}$ because the only forces that the density can alter are the thermal forces, and the first two terms cancel:

$$\frac{D\hat{S}}{D\rho_i} = -\frac{1}{2} \mathbf{U}^T \frac{D\mathbf{K}}{D\rho_i} \mathbf{U} + \mathbf{U}_{TE}^T \frac{D\mathbf{K}}{D\rho_i} \mathbf{U} - \frac{1}{2} \mathbf{U}_{TE}^T \frac{D\mathbf{K}}{D\rho_i} \mathbf{U}_{TE} \quad (3.97)$$

Equation 3.97 can be computed easily but note that the displacements due to the thermal forces \mathbf{U}_{TE} must be computed in an additional finite element step in order to evaluate both strain energy and the design sensitivity. Note once again that, although the

design sensitivity in Equation 3.97 is valid in general, the discretization in Equation 3.98 is only valid for the specific discretization used in this work

$$\frac{D\hat{S}}{D\rho_i} = p\rho_i^{p-1}(-\frac{1}{2}\mathbf{U}_i^T \mathbf{K}_i \mathbf{U}_i + \mathbf{U}_{TEi}^T \mathbf{K}_i \mathbf{U} - \frac{1}{2}\mathbf{U}_{TEi}^T \mathbf{K}_i \mathbf{U}_{TEi}) \quad (3.98)$$

Similarly, the design sensitivity of strain energy in terms of the element orientations can be computed. The manner of derivation is similar, and it can be expressed in terms of the terms that have already been computed in a fully discretized form.

$$\frac{D\hat{S}}{D\theta_i} = \rho_i^p * (-\frac{1}{2}\mathbf{U}_i^T \frac{\partial \mathbf{K}_i}{\partial \theta_i} \mathbf{U}_i + \mathbf{U}_{TEi}^T \frac{\partial \mathbf{K}_i}{\partial \theta_i} \mathbf{U} - \frac{1}{2}\mathbf{U}_{TEi}^T \frac{\partial \mathbf{K}_i}{\partial \theta_i} \mathbf{U}_{TEi}) \quad (3.99)$$

With these design sensitivities evaluated, either compliance or strain energy could be considered as the objective function in a topology optimization performed using either the OC or GCMMA method.

CHAPTER FOUR

Results

4.1 Overview

The purpose of this work is to compute optimal topologies for and determine which objective function and update method can optimize the performance of weakly coupled thermomechanical systems. The two objective functions compared here, compliance and strain energy, are identical under purely mechanical loading, so any test cases used for comparison must incorporate significant thermal loading. Compliance is considered as it is the classical stiffness inverse and has been extensively studied as such. Strain energy has recently been explored as an alternate stiffness inverse and is a measure of the amount of energy needed to deform the structure from unconstrained expansion to a loading scenario. The effects of increasing the contribution of thermal loading as a fraction of overall loading are considered in a case study. Both the optimality criterion method and the GCMMA method described in Sections 3.3 and 3.4 respectively are used to optimize the design, and the relative effectiveness of each optimization algorithm is compared. As the thermal loading is a significant fraction of the total loading, a sensitivity mapping is provided for compliance optimization in the optimality criterion method. Several different gradient mappings are presented and compared to determine if the choice of gradient mapping impacts the structure.

A simple design domain is chosen for this study as shown in Figure 4.1. The anisotropic weakly coupled system is defined over this design domain as described in

Chapter three. The topology optimization problem in Equation 3.28 is first solved for minimum compliance assuming purely mechanical loading of an isotropic structure, and then anisotropy and thermal loading are included in successive optimization examples. The successive introduction of anisotropy and thermal loading demonstrate their effects on the optimized structure, and the difference in performance between compliance optimization and strain energy optimization is determined.

4.2 Problem Setup

The MBB beam [22], a two-dimensional aircraft structural beam in three-point bending, has been used extensively in the literature as a benchmark topology optimization problem, and it is considered here with the design domain in Figure 4.1. This design domain includes a two-dimensional rectangle, with the length four times the width. Half symmetry is assumed for the structure, so only half of the beam appears in Figure 4.1, which also shows the shape of the design domain and the location of applied loads and displacements are shown in Figure 4.1.

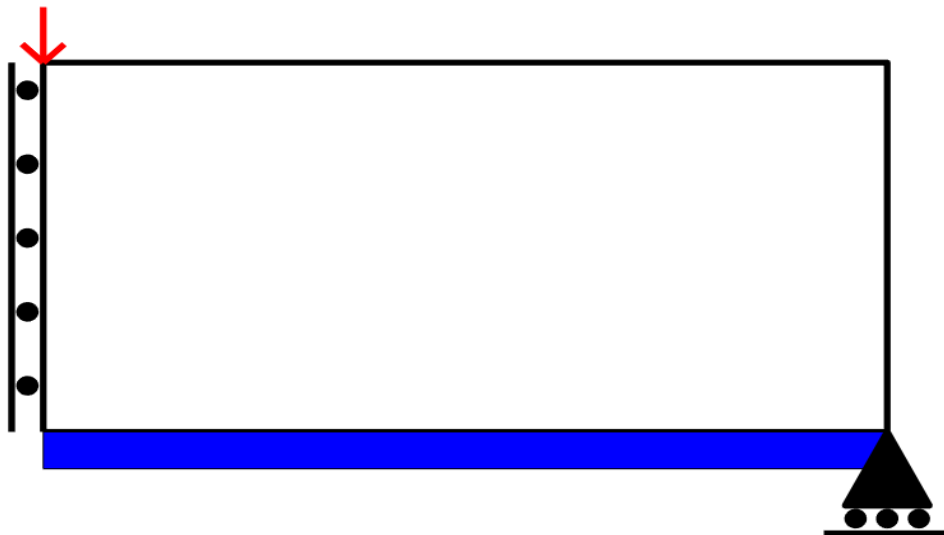


Figure 4.1: Design Domain of MBB Beam

The left edge has a symmetric boundary condition in the x-direction, and the bottom right corner is fixed in the y-direction. A force is applied at the top left node in the negative y-direction. When only mechanical loading is considered, the magnitude of the applied force is irrelevant as the small-displacement assumption results in compliance being directly proportional to the applied force by linearity. However, once thermal loading is included the relative magnitude of the applied heat fluxes to the mechanical force directly influence the optimal topology, so the force is arbitrarily chosen to be $F = 500 \text{ N}$.

Thermal boundary conditions are also defined. It is assumed that the structure is initially set at an arbitrary temperature, and all thermal behavior is driven by temperature changes relative to this initial temperature. The bottom edge is prescribed a temperature increase of zero, and a heat flux is applied at the same location as the mechanical force. The intensity of this heat flux is changed in different optimizations to investigate the effects of increasing thermal loading.

In the first example, an isotropic material is considered, with the applied heat flux set to zero (i.e. $F_{Th} = 0$ in Equation 3.65). This set of loading conditions is identical to the system considered in the 99-line code in Sigmund's 2001 paper [22] and serves to validate the basic performance of our topology optimization method. Under this loading compliance and strain energy are equal, so compliance is considered as the objective function. The volume fraction is set to $V_f = 0.5$ and the material properties of carbon fiber-reinforced ABS polymer are used. Note that the value of the Young's modulus is arbitrary as the displacement field is proportional to the Young's modulus, but the computed optimal structure does not vary with Young's modulus. The design space in

Figure 4.1 is discretized into 200×100 identically sized bi-square linear finite elements. The OC method in Section 3.5 is applied until convergence is achieved, and the final structure is presented in Figure 4.2.

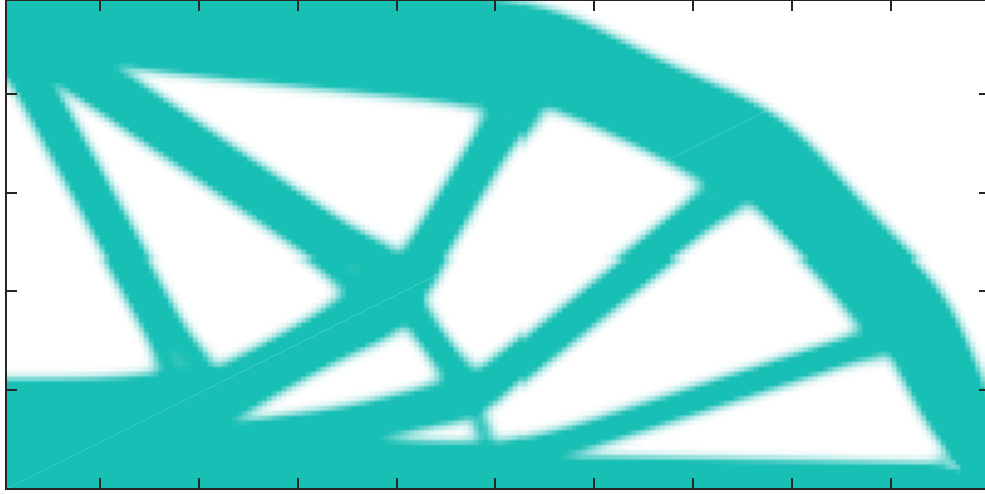


Figure 4.2: Final Topology of Isotropic MBB Beam Under Pure Mechanical Loading by OC Method

Under the OC method, convergence is monotonic, and the algorithm is run for 200 iterations. The final compliance value is 5.604 mJ , and the convergence history is displayed in Figure 4.3.

The GCMMA method in Section 3.6 can also be used to optimize the structure, but it requires the volume fraction constraint to be expressed as two separate inequality constraints in order to imitate the equality constraint in the OC algorithm. The tuning parameters for the GCMMA method are presented in Table 4.1.

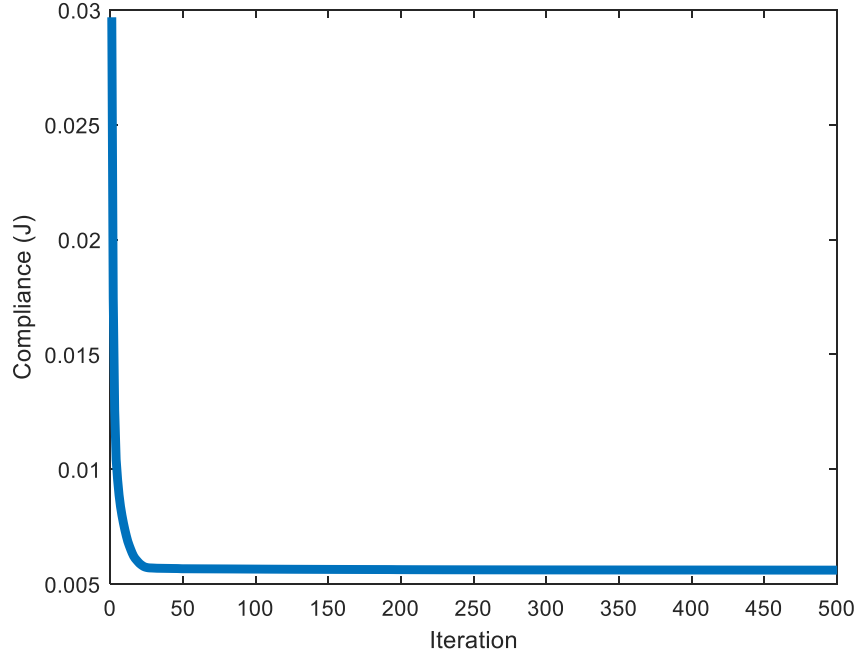


Figure 4.3: Convergence History of Compliance Optimization of Isotropic Mechanical MBB Beam Using OC Method

Table 4.1: Constants for GCMMA Algorithm

Variable	Value
f_0	500
c_1	100
c_2	100

The final topology was reached in 500 iterations of the GCMMA algorithm and yields the design in Figure 4.4. Note that the structure different from the final topology of the OC method in Figure 4.2, as each method has found different local minima. The design space has a vast number of local minima, and each method treats the gradient differently, so it is expected that each method would generate different structures.

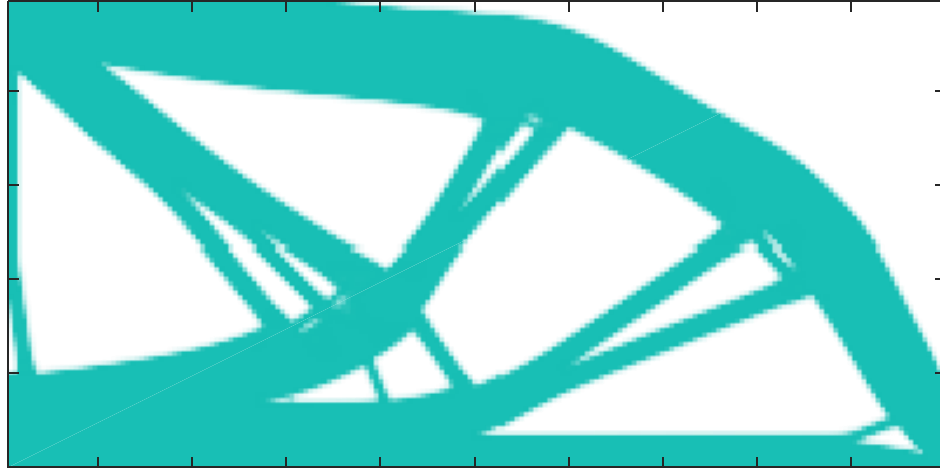


Figure 4.4: Final Topology of Isotropic MBB Beam Under Pure Mechanical Loading by GCMMA Method

The convergence of the compliance is also monotonic under the GCMMA algorithm. Note that the convergence rate is much slower than the OC method, as seen in Figure 4.5. The final compliance value is 5.494 mJ , which is higher than the compliance obtained by the OC method, but only by 1.3%. This near-identical performance suggests that both algorithms can optimize compliance effectively over an isotropic system with only mechanical loading.

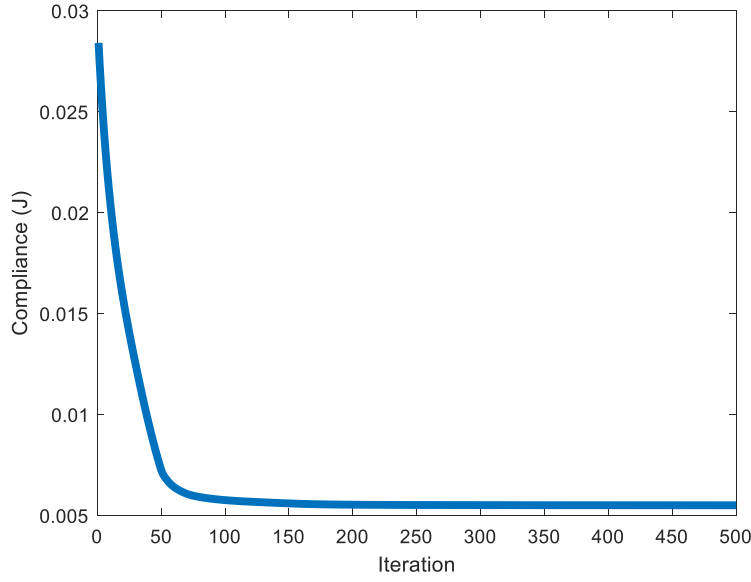


Figure 4.5: Convergence History of Compliance Optimization of Isotropic Mechanical MBB Beam Using GCMMA Method

As a second example, the material in the design domain in Figure 4.1 is assumed to be orthotropic, with a Young's modulus E_x in the principal direction greater than that in the perpendicular direction (i.e. E_y) according to $\frac{E_x}{E_y} = 10$. Note that this modulus ratio is higher than what is usually found in short-fiber reinforced composite structures and is instead closer to the increase in Young's modulus for continuous fiber-reinforced structures. Our work primarily considers short-fiber reinforced polymers but exaggerating the degree of anisotropy allows for its effects to be clearly demonstrated. The same design domain (Figure 4.1) is optimized with this new material, allowing both elemental densities ρ_i and orientations θ_i to be altered as design variables, using both the OC and GCMMA algorithm. Recall that allowing anisotropic material properties to vary spatially is one of the two factors we seek to include to model the additive manufacturing process. Thermal behavior will be incorporated subsequently, but the applied heat flux is kept at

zero. The converged structure obtained with the OC method is presented in Figure 4.6 where element material orientation appears as a short line segment in corresponding elements. Only the orientations in alternating elements are displayed to ensure that the orientations are visible.

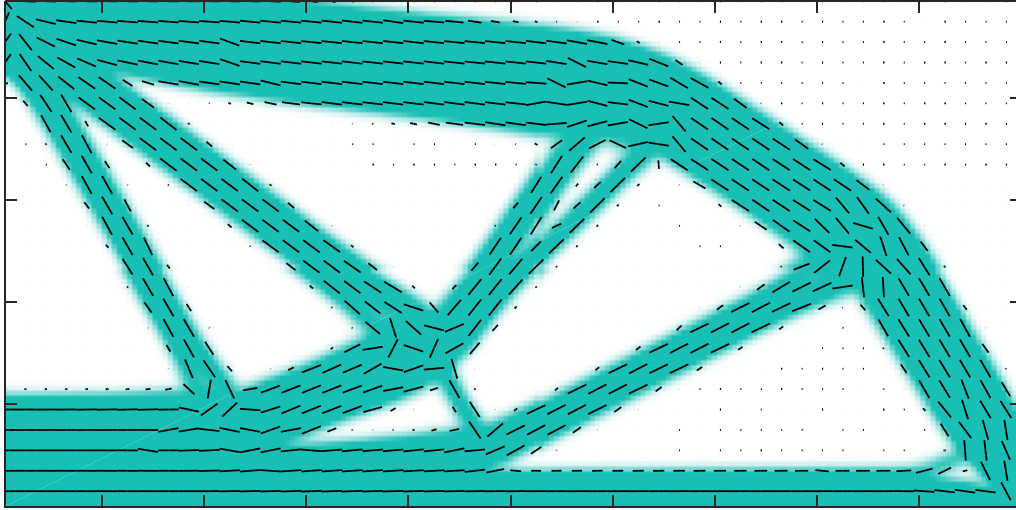


Figure 4.6: Final Topology of Anisotropic MBB Beam Under Pure Mechanical Loading by OC Method

Only half of the structure is displayed so that element orientations can be more easily observed. Note that Figure 4.6 is a different structure than the isotropic optimization in Figure 4.2, indicating that the same result cannot be obtained by first assuming isotropy and optimizing the material density, and then optimizing the element orientations separately. The design space is thus not convex and optimizing all design variables simultaneously is necessary. The convergence is still smooth and monotonic, and the final compliance value is 0.5861 mJ after 500 iterations as shown in Figure 4.7.

Note that the element orientations, represented by vectors at each element, are oriented roughly in the axial direction of each of the truss-like sections. Axial alignment

of fibers is intuitive, as the elements in those regions are loaded approximately axially. In the regions where the truss-like segments meet, the orientations are more complex.

The compliance decreases rapidly in the initial 20 iterations as the orientations adjust from the initial random state to a more ordered alignment. After about 20 iterations through the final iteration the compliance experiences small decreases, as seen in Figure 4.7.

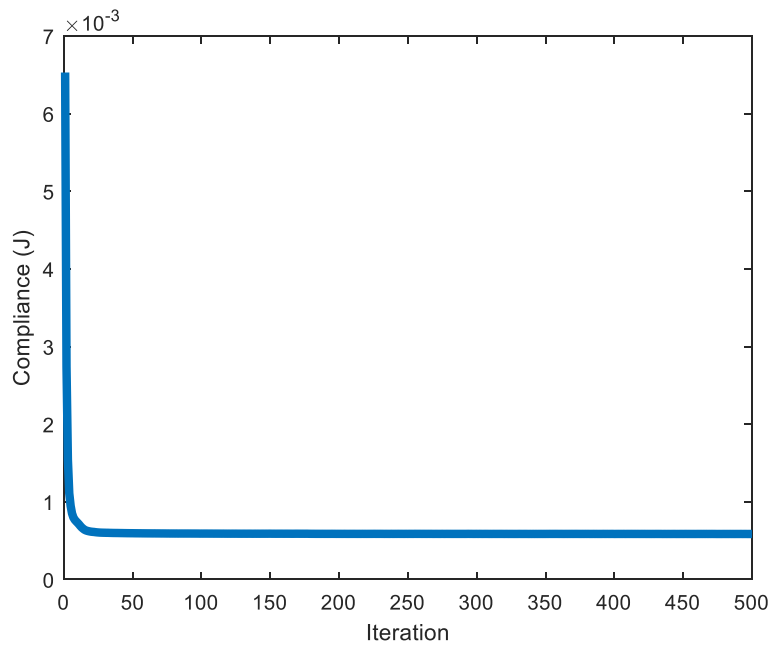


Figure 4.7: Convergence History of Compliance Optimization of Anisotropic Mechanical MBB Beam Using OC Method

The GCMMA algorithm converges slower for the same design domain and is run for 500 iterations. Convergence is no longer uniform in the early iterations but decreases monotonically after the first thirty iterations. Once again, the structure obtained is different than the structure obtained in the OC method due to the difference in how each algorithm treats the gradient, as seen in Figure 4.8.

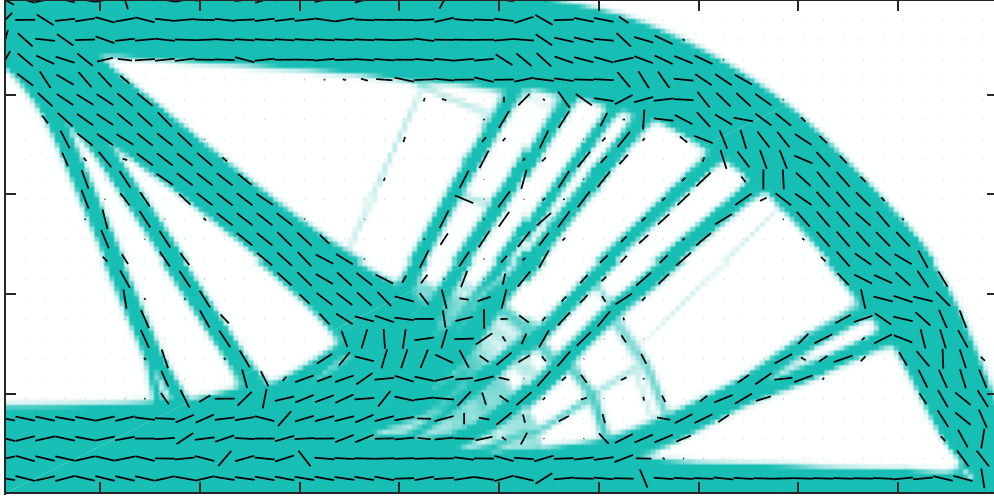


Figure 4.8: Final Topology of Anisotropic MBB Beam Under Pure Mechanical Loading by GCMMA Method

It is clear from Figure 4.8 that the element orientations have more variation and are not as uniformly aligned, which may explain why the compliance in this test is slightly higher than the compliance obtained in the OC optimization. The convergence is no longer monotonic, as seen in Figure 4.9.

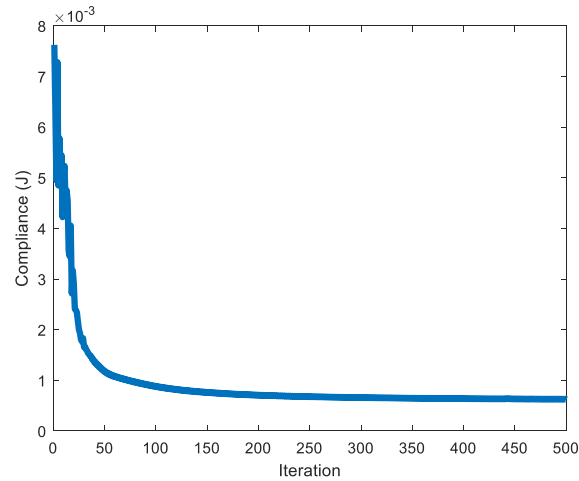


Figure 4.9: Convergence History of Compliance Optimization of Anisotropic Mechanical MBB Beam Using GCMMA Method

The non-monotonic convergence behavior is likely due to the extremely high sensitivity of compliance to the orientation of the elements near the point of load application. The GCMMA approach is based on a linear approximation of the objective function and constraints, and the behavior of compliance with respect to these orientations is highly nonlinear, so as those element orientations change by a large amount in the first few iterations the assumption that each element orientation can be optimized independently is not particularly accurate, and the compliance value can increase. Once those element orientations have stabilized, the compliance convergence is monotone. Note that the tests in Figure 4.6 and 4.8 show that the OC and GCMMA algorithms can converge to final structures, and that under no thermal loading compliance and strain energy are equal.

4.3 Weakly Coupled Orthotropic Thermomechanical System

It has now been shown that the anisotropic topology optimization can be performed, and that the optimization converges to a local minimum efficiently. The local minimum differs based on the technique used, but both methods converge effectively to structures with near-identical performance. To more closely model additive manufacturing, thermal behavior is included as described in Section 3.7. Recall that the structure is assumed to begin at an arbitrary temperature, and the bottom edge of the structure is fixed at that temperature and subjected to no temperature change. At the top corner, the same location where the force is applied, a heat flux of 30 W is applied to the node at the top left corner. The temperature field, thermal stresses, and their effects on compliance and strain energy are computed as described in Chapter 3.

As described above, compliance and strain energy are equivalent under pure mechanical loading. However, when the thermal loading is nonzero, these objective functions yield different values and optimizing each will lead to different structures. It is not immediately clear which optimization function yields superior results, or even how “superior results” should be defined. Thus, the optimization will be performed once for compliance and then once for strain energy as the objective function using both the OC and GCMMA optimization methods, making four separate optimization solutions being performed below. The results are displayed below.

The optimality criterion method’s performance is examined first, and both objective functions are optimized in successive tests. Only half of the final topology is presented, as the design is symmetric. The first system considered is compliance optimization with the OC method, as seen in Figure 4.10.

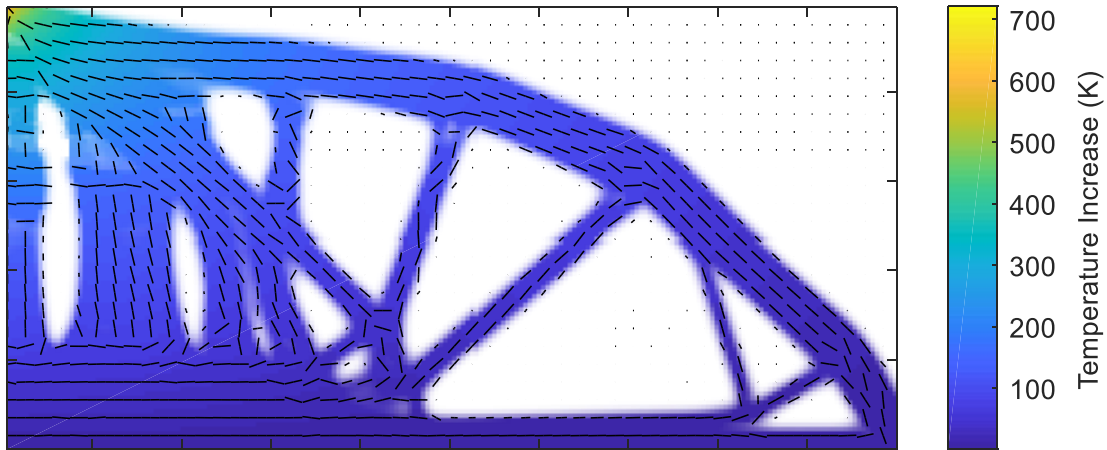


Figure 4.10: Final Topology of Orthotropic Weakly Coupled Model, Compliance Optimized with the Optimality Criteria Method

Note that the colored contours represent temperature. The optimal topology of the compliance-based model retains some small areas of fractional density where the material

has not completely converged to solid or void. This is highlighted in Figure 4.10b, where the region of intermediate density is shown.

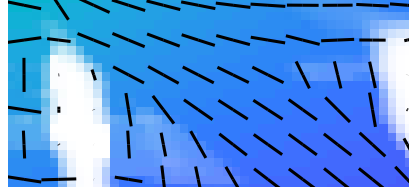


Figure 4.10b: Region of Fractional Density Present in Figure 4.10

Further iterations do not resolve these small regions. These regions have no physical interpretation and cannot be produced, although these regions are small enough that a simple rounding step in post-processing would remedy this while only trivially altering the structure's performance. Under higher density move limits, material was found to oscillate within these regions without converging, so a density move limit of $m = 0.05$ was imposed to prevent this behavior. The convergence history of the compliance objective function appears in Figure 4.11.

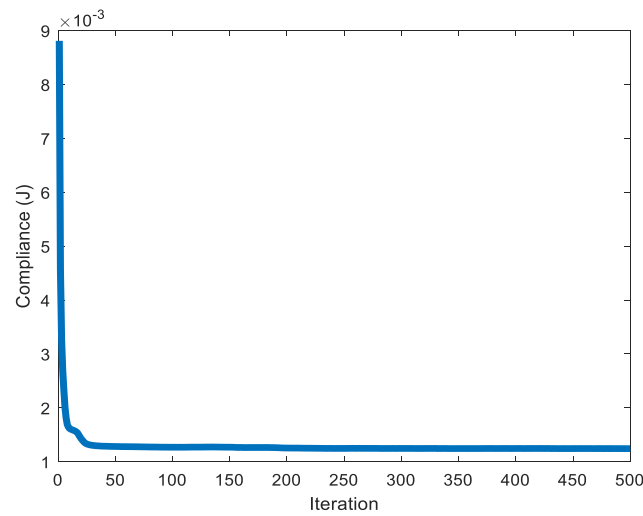


Figure 4.11: Compliance Convergence History of Orthotropic Weakly Coupled Model, Optimality Criterion Method

As seen in Figure 4.11, the compliance decreases rapidly initially, and then experiences little change for the next 900 iterations, although the convergence is not monotonic. This may be due to the heuristic modifications to the gradient given in Equation 3.38 for the optimality criterion method. The strain energy optimization generates a structure with a much different form than that produced with the OC method, as seen in Figure 4.12.

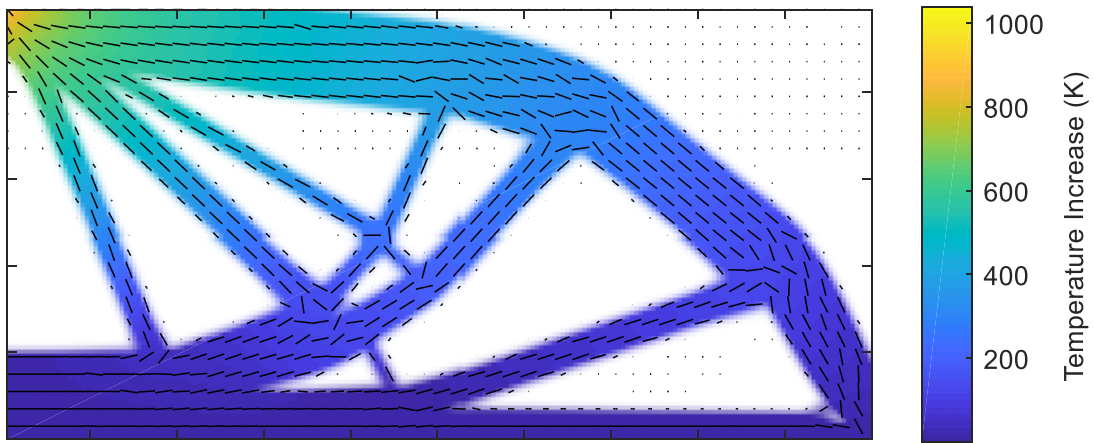


Figure 4.12: Final Topology of Orthotropic Weakly Coupled Model, Strain Energy Optimized via the Optimality Criteria Method

The optimum structure in Figure 4.12 converges to a design that resolves entirely to solid or void when strain energy is optimized. Unlike the compliance optimization, the design resembles the structure generated by optimization of purely mechanical compliance in Figure 4.6. The convergence is also not monotonic, but the strain energy is the lowest strain energy value for the optimization after 1000 iterations. The convergence history is displayed in Figure 4.13.

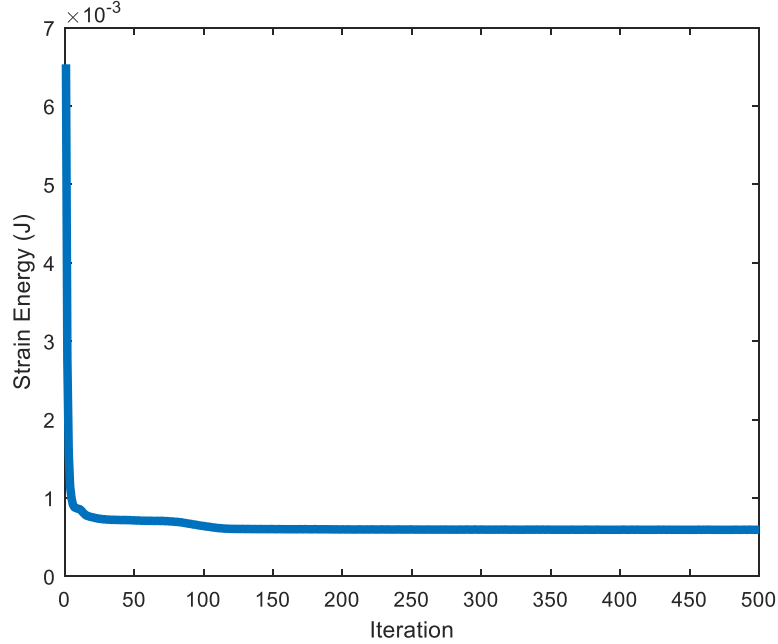


Figure 4.13: Strain Energy Convergence History of Orthotropic Weakly Coupled Model, Optimality Criterion Method

It is worth noting that the strain energy increases between iterations 42 and 185 in Figure 4.13. This increase despite the use of the gradient is similar to the behavior of the compliance optimization, although the algorithm does indeed converge to a minimum. The design has no fractional density regions, and thus can be produced without density rounding in post-processing. The need for less post-processing is a minor improvement over the compliance optimization, though the relative performance of each has not yet been compared.

While these optimizations converge to generate structures, the non-monotonic convergence and fractional density in the compliance optimization are not ideal. We thus turn to the GCMMA algorithm to perform the same optimizations. The compliance is optimized once again, though the GCMMA method is now used. The resultant structure is presented in Figure 4.14.

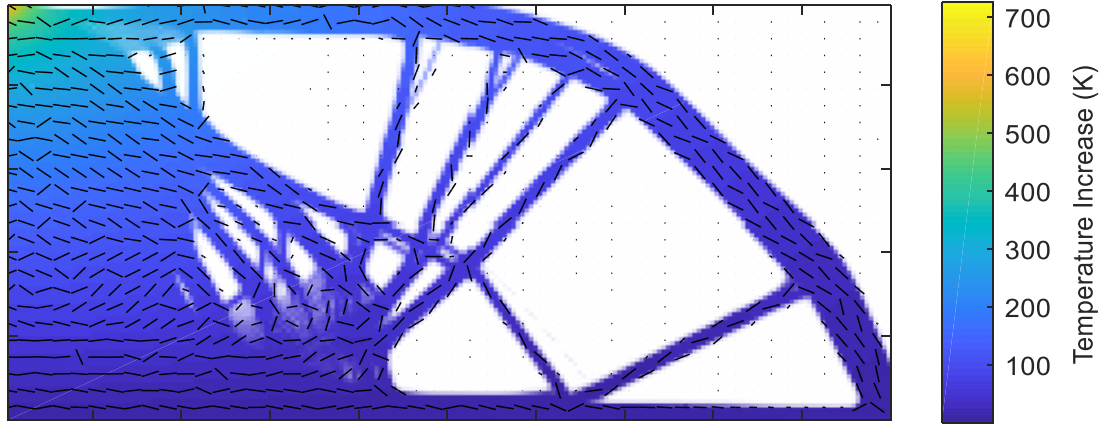


Figure 4.14: Final Topology of Orthotropic Weakly Coupled Model, Compliance Optimized via the GCMMA Method

After 1000 iterations, the design has approached a structure with some similarities to the OC optimization. A region of intermediate density still exists at the top-left corner, and does not resolve to solid or void under further iterations. The arch structure supporting a pyramid-like structure resembles Figure 4.10. The convergence history in Figure 4.15 shows near-monotonic convergence.

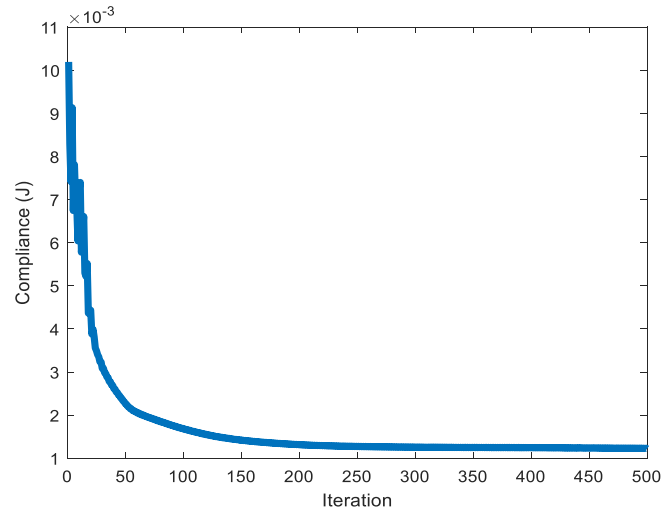


Figure 4.15: Compliance Convergence History of Orthotropic Weakly Coupled Model, GCMMA Method

The convergence appearing in figure 4.15 is near-monotonic as in the OC method, and a similar structure with regions of fractional density is generated. The differences in the structure are likely because the GCMMA algorithm does not alter the gradient as much as the OC method, but the similarity of the convergence histories and final structures indicate that both operate comparatively. The strain energy is optimized next, and the final structure is shown in Figure 4.16.

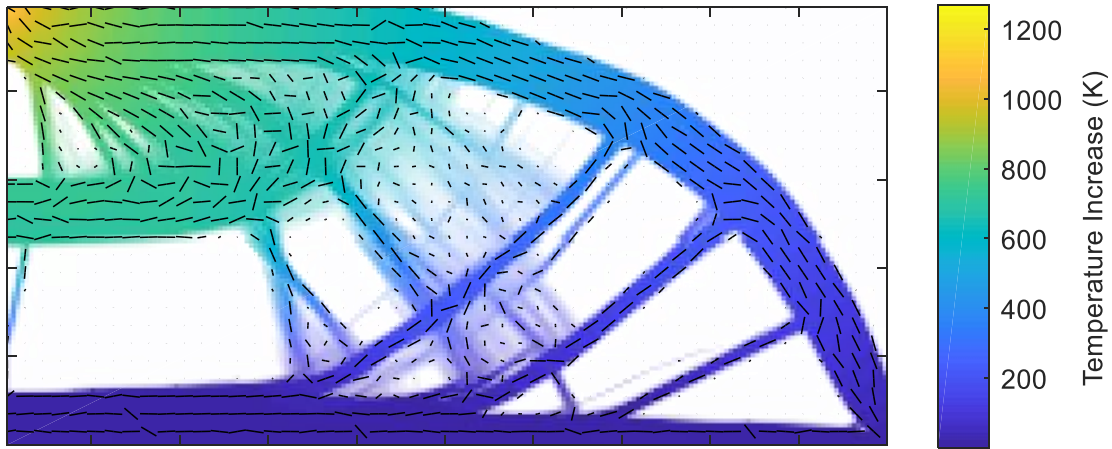


Figure 4.16: Final Topology of Orthotropic Weakly Coupled Model, Strain Energy Optimized via the GCMMA Method

The design retains several large regions of intermediate density, unlike the strain energy optimization by the OC method. The design looks significantly different from the one appearing in Figure 4.12, as the methods have different move limits and ways of handling the gradient. The relative performance of these optimizations can be compared to indicate the effectiveness of the optimization methods and objective functions. The convergence history is near-monotonic and the final strain energy is higher than the strain energy of the OC strain energy optimization, as seen in Figure 4.17. Note that the spike at iteration 316 is due to a matrix singularity issue due to numerical instabilities.

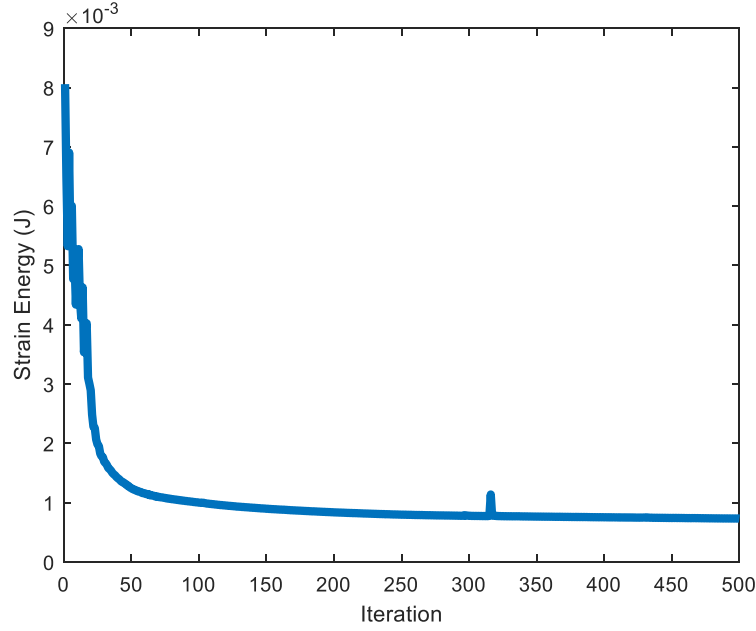


Figure 4.17: Strain Energy Convergence History of Orthotropic Weakly Coupled Model, GCMMA Method

4.4 Comparison of Performance

The performance of each of the optimizations of the full model is summarized in Table 4.2. Note that both objective function values are given even though only one response is optimized in each simulation.

Table 4.2: Optimization Performance

Test Type	Compliance [mJ]	Strain Energy [mJ]
OC Strain Energy	-	0.5927
GCMMA Strain Energy	-	0.7310
OC Compliance	1.243	-
GCMMA Compliance	1.221	-

The OC method obtains a significantly lower value of the objective function for strain energy optimization, but slightly worse performance in the compliance optimization. Specifically, it appears that the GCMMA strain energy optimization

converged to a local minimum that is much further from the global minimum than the local minimum found by OC method. However, the compliance optimization shows that the relative performance of the algorithms is problem dependent. Both algorithms handle the gradient differently, and the OC method has been modified with a separate orientation optimization method devised in this work. This is more specialized than the general GCMMA algorithm which considers the densities and orientations simultaneously. The effects of the thermal loading on the relative performance of the algorithms can be further investigated by optimizing the weakly coupled thermomechanical system for an isotropic material. Figure 4.18 shows the final structure of compliance optimization by the OC method for the same design space used above, except that $\frac{E_x}{E_y} = 1$.

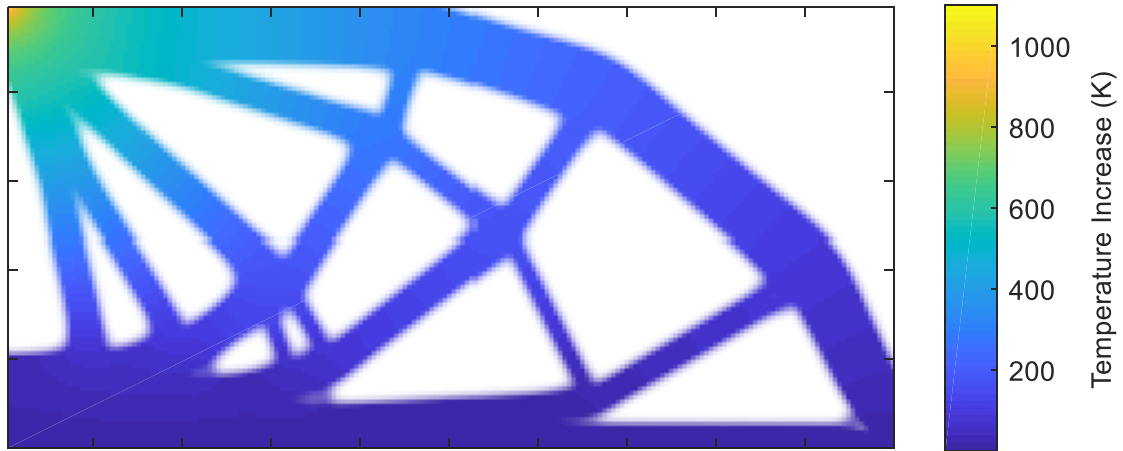


Figure 4.18: Final Topology of Isotropic Compliance Optimization via the OC Method

The same design domain can be optimized with the GCMMA method, which is presented in Figure 4.19. Note that the temperature distribution, as shown by the colored temperature contours, is very similar.

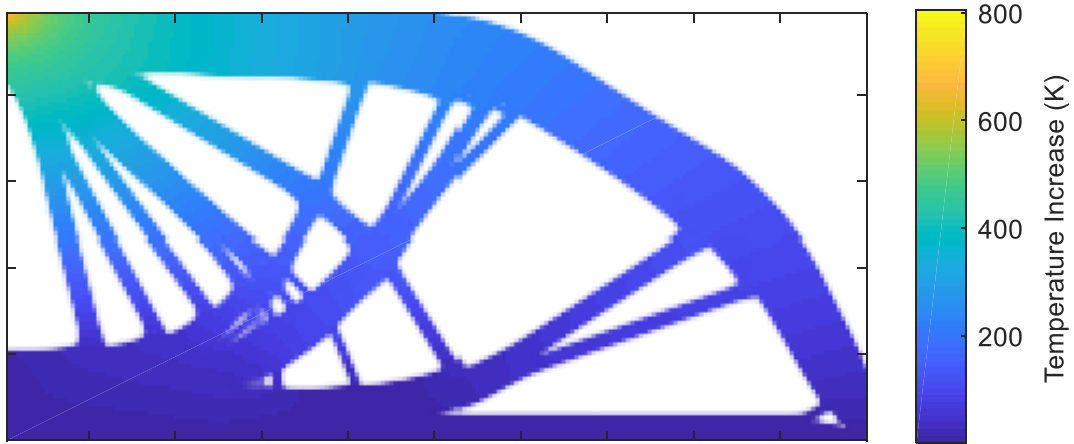


Figure 4.19: Final Topology of Isotropic Compliance Optimization via the GCMMA Method

The strain energy can also be optimized with the OC and GCMMA methods, and the final structures are presented in Figure 4.20 and 4.21 respectively. When the material is isotropic, the OC and GCMMA methods generate nearly identical structures.

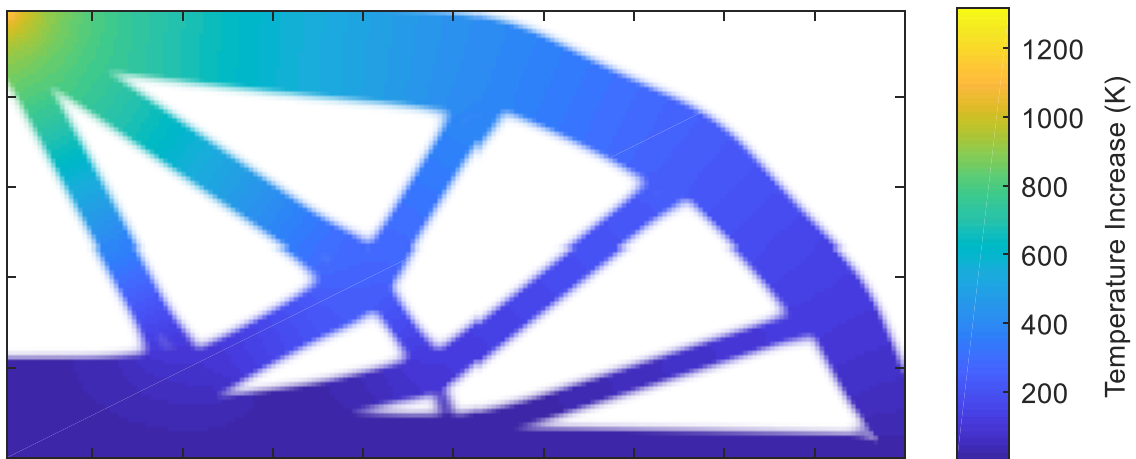


Figure 4.20: Final Topology of Isotropic Strain Energy Optimization via the OC Method

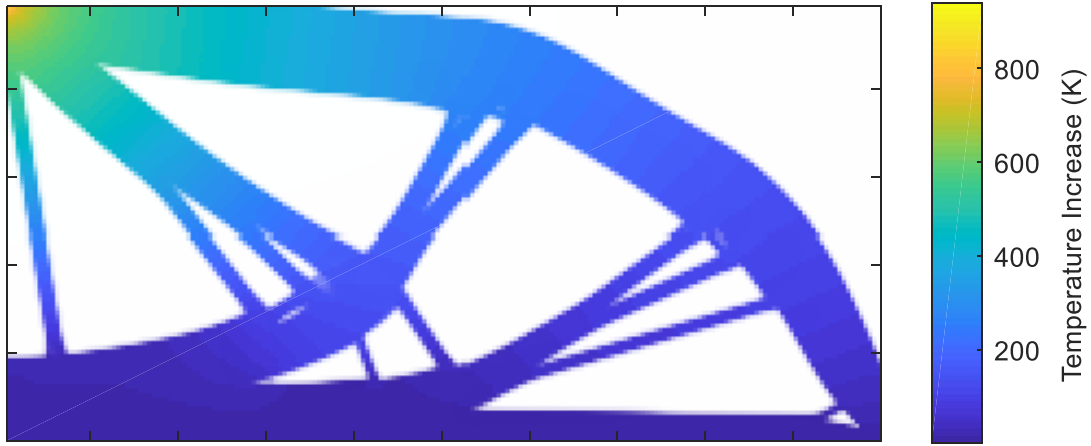


Figure 4.21: Final Topology of Isotropic Strain Energy Optimization via the GCMMA Method

The relative performance of the isotropic optimizations can be compared by presenting the objective functions for each structure. This is shown in Table 4.3.

Table 4.3: Optimization Performance for Isotropic Material

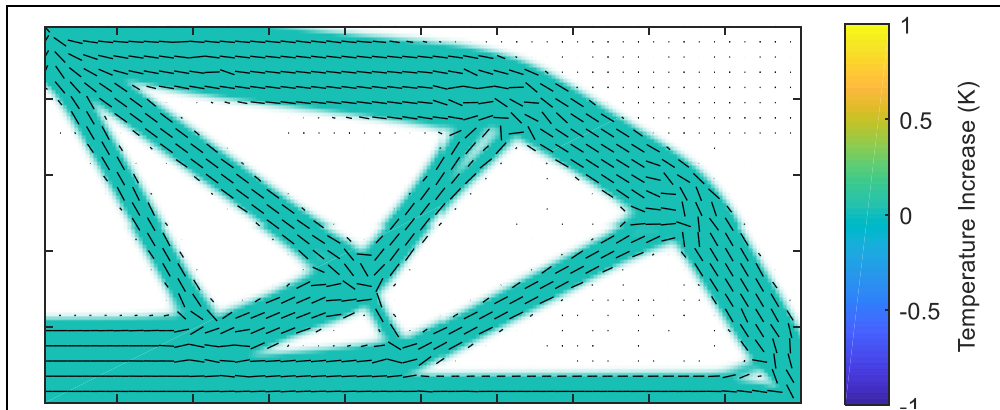
Test Type	Compliance [mJ]	Strain Energy [mJ]
OC Strain Energy	-	5.601
GCMMA Strain Energy	-	5.521
OC Compliance	6.331	-
GCMMA Compliance	6.052	-

In the isotropic case, the OC and GCMMA methods perform very similarly in both topology and objective function. The nearly identical performance indicates that the interaction between the anisotropy and thermal effects are causing the convergence difficulty observed in the earlier GCMMA strain energy optimization case. Based on these tests, the authors recommend using the OC method as it converges overall to lower local minimums in the full anisotropic weakly coupled thermomechanical case.

4.5 Effects of Increased Thermal Loading

Under only mechanical loading, compliance and strain energy are equal. As the thermal loading increases the two objective functions diverge and optimizing over each generates radically different structures. Since the pure mechanical problem is well-documented even for anisotropic materials, it is interesting to observe the effects as the thermal loading increasingly dominates the structure. The mechanical force is fixed at 500 N and the thermal heat flux is allowed to vary from 0 W to 50 W in successive optimizations. Both compliance and strain energy are optimized with the OC method, and the results are presented below in Figure 4.22.

For each design space, two optimizations are performed with the OC method and half of each structure is displayed. When the thermal loading is zero, the structures are identical and as the thermal load increases the structures adopt radically different forms. The strain energy-optimized structure maintains the same rough arch shape throughout, although the support members shift. The compliance-optimized structure increasingly adopts a pyramid-like shape, which is optimal to distribute the thermal flux.



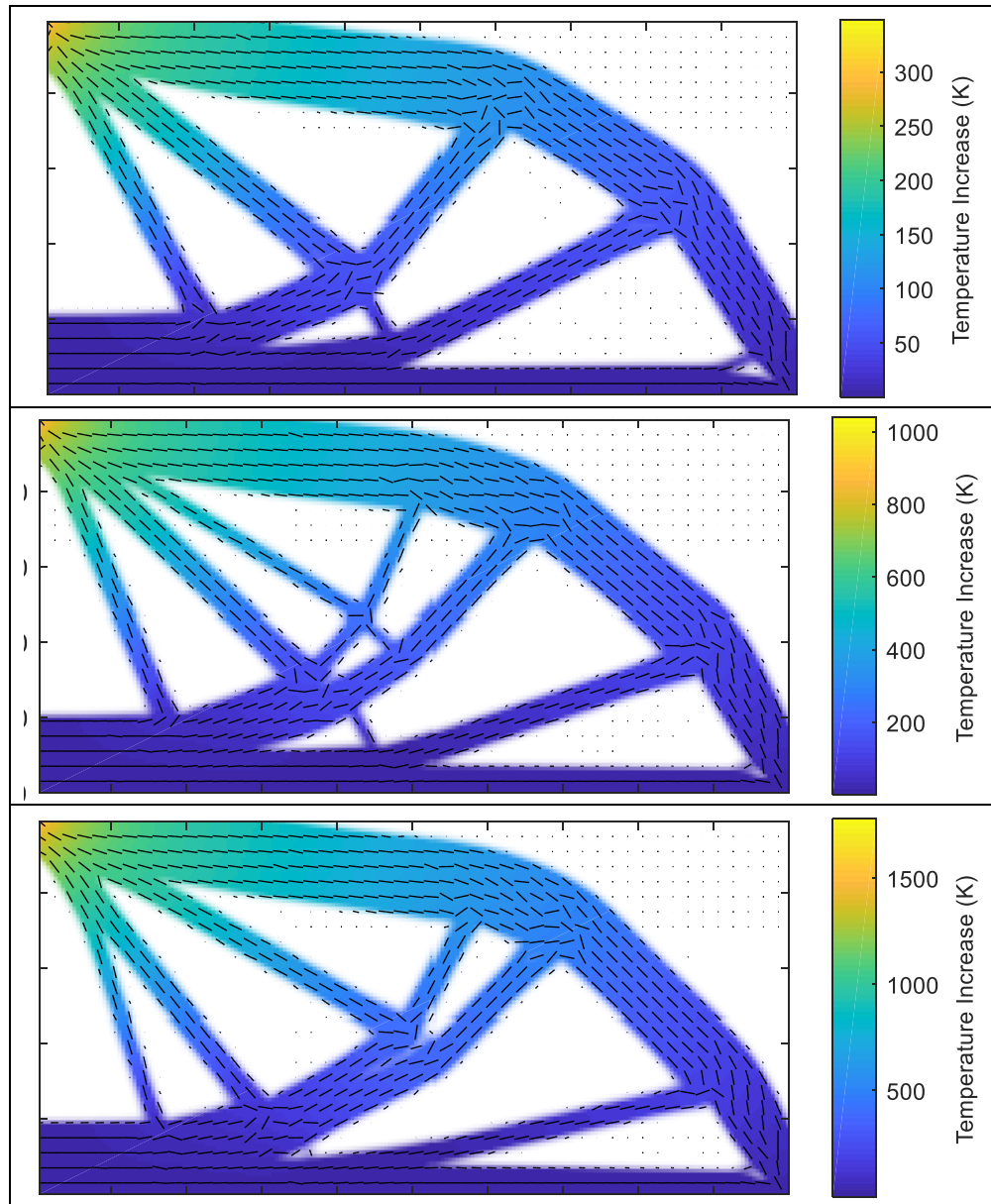


Figure 4.22a: Final Strain Energy – Optimized Topologies as Thermal Loading Increases. Thermal Load Values are 0 W , 10 W , 30 W , and 50 W

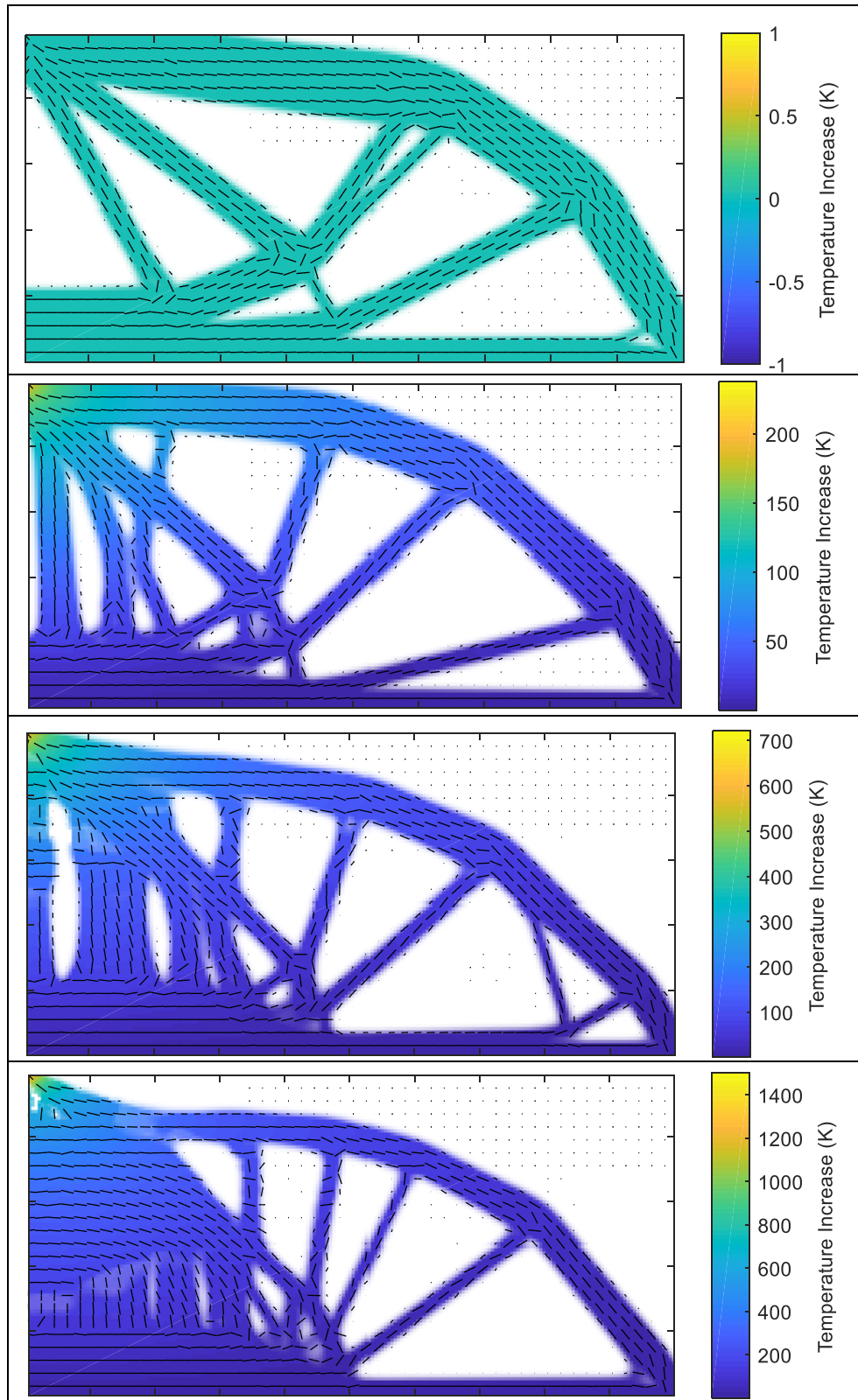


Figure 4.22b: Final Compliance – Minimized Topologies as Thermal Loading Increases. Thermal Load Values are 0 W , 10 W , 30 W , and 50 W

Their relative performance can be compared in Table 4.4.

Table 4.4: Performance of Compliance and Strain Energy-Optimized Structures

Tests	Compliance (mJ)	Strain Energy (mJ)	Max Disp (μm)
Test 1 C	0.5861	0.5861	2.302
Test 1 SE	0.5856	0.5856	2.302
Test 2 C	0.8069	0.6380	2.771
Test 2 SE	0.9750	0.5862	2.847
Test 3 C	1.243	0.7361	3.496
Test 3 SE	2.376	0.5927	3.895
Test 4 C	1.796	0.8683	4.349
Test 4 SE	4.971	0.5993	5.075

The compliance optimization and strain energy optimization each optimize their respective objective functions, so the maximum displacement value is given as a basis for comparison. The slight difference in test 1 compliance and strain energy optimizations is likely due to different randomly generated initial values for the orientation field. While the maximum displacement is higher for strain energy, depending on the application and desired performance of the structure, one objective function may be better suited than the other.

To quantify the amount of thermal loading in the above tests, the fraction of each compliance value due to the thermal loading is computed. This is done for compliance by setting the thermal displacements to zero and computing the compliance for the determined topology using only the mechanical displacements to determine the

mechanical contribution. This is then subtracted from the total compliance to determine the thermal contribution, which is presented in Table 4.5.

Table 4.5: Thermal Contribution to Compliance in Various Tests

Tests	Thermal Contribution to Compliance (%)
Test 1 C	0
Test 1 SE	0
Test 2 C	20.9
Test 2 SE	39.9
Test 3 C	40.8
Test 3 SE	75.1
Test 4 C	51.7
Test 4 SE	87.9

It is apparent that the thermal loading contributes differently in the various optimally computed structures existing in the same design domain. Some designs are more effective at distributing the thermal loading relative to how they distribute the mechanical loading. It is clear that the compliance-optimized parts are more effective at distributing the heat transfer, as the effect of the thermal loading is lower. This is consistent with the lower maximum displacement values for compliance optimization noted in Table 4.4, as compliance-minimized structures distribute the heat more effectively which causes lower thermal stresses. This can be seen in the placement of significant amounts of material on the left of the design domain in the compliance-optimized structures, which distributes the heat flux to the cold plate at bottom. The strain energy-optimized structures do not share this behavior.

4.6 Convergence Issues

4.6.1 Compliance Sensitivity Shifting

Several convergence issues were encountered in the above optimizations, particularly for compliance optimization using the OC method. The OC method was designed for mechanical compliance optimization, and in such systems the design sensitivities always have negative values. Under high thermal loading it is possible for the design sensitivities of compliance with respect to density to be positive, which in the optimality criterion method will force those elements to remove material up to the move limit. The procedure used here is to map the positive sensitivities to the negative numbers with some mapping function. Several different functions are considered. All mapping functions share the following form, as shown in Equation 3.

$$\frac{dC}{d\rho_i}|_{new} = \begin{cases} \frac{dC}{d\rho_i}, & \frac{dC}{d\rho_i} < 0 \\ f\left(\frac{dC}{d\rho_i}\right), & \frac{dC}{d\rho_i} \geq 0 \end{cases} \quad (4.1)$$

The function used in all the above optimization examples was $f(d) = 0$, as this mapping function alters the sensitivities as little as possible. Several prospective functions can be considered however, and their performance compared. Note that $mp = \max\left(\frac{dC}{d\rho_i} \mid \frac{dC}{d\rho_i} < 0\right)$, the negative design sensitivity with the smallest magnitude. The four mapping functions that are considered are given in Equations 4.2 – 4.5.

$$f(d) = 0 \quad (4.2)$$

$$f(d) = \left(-\frac{\pi}{2} - \text{atan}(d)\right) * \frac{mp}{10} \quad (4.3)$$

$$f(d) = \left(-\frac{\pi}{2} - \text{atan}(d)\right) * mp \quad (4.4)$$

$$f(d) = -mp * e^{-d} \quad (4.5)$$

Each of these sensitivity mappings is tested in an optimization simulation where the compliance is optimized by the OC method. It is identical to the test done for Figure 4.10, except that the move limit is set to an extremely conservative 0.02 and the thermal loading is set to $1 \mu W$. The resultant topologies are presented below in Figure 4.23.

Based on the near-identical topologies shown in Figure 4.23, it appears that the mapping function used does not actually affect the convergence of the structure for the design domain considered. Slightly different topologies are generated, but such minor differences are expected due to the random initialization of the orientation design variables, and all topologies exhibit similar small regions of fractional density. The simplest mapping function, setting the positive compliances to zero, is then the preferred method as it causes the smallest changes to the design sensitivities.

4.6.2 Relative Penalty Values

Another convergence issue is that the compliance-optimized structures, regardless of the method used, can retain regions of intermediate density. Fractional density, as stated before, has no physical interpretation and it is desired that a method exists to force these regions to resolve. These regions are generally present in loading cases with higher thermal loads. This is likely due to the behavior of elements with fractional density under the SOMP penalization method. A material with half density is mechanically weak but behaves as a thermal insulator which can be beneficial in the thermal analysis. While such behavior may be effective from the perspective of the algorithm, it is necessary to prevent this behavior to make the designs useable.

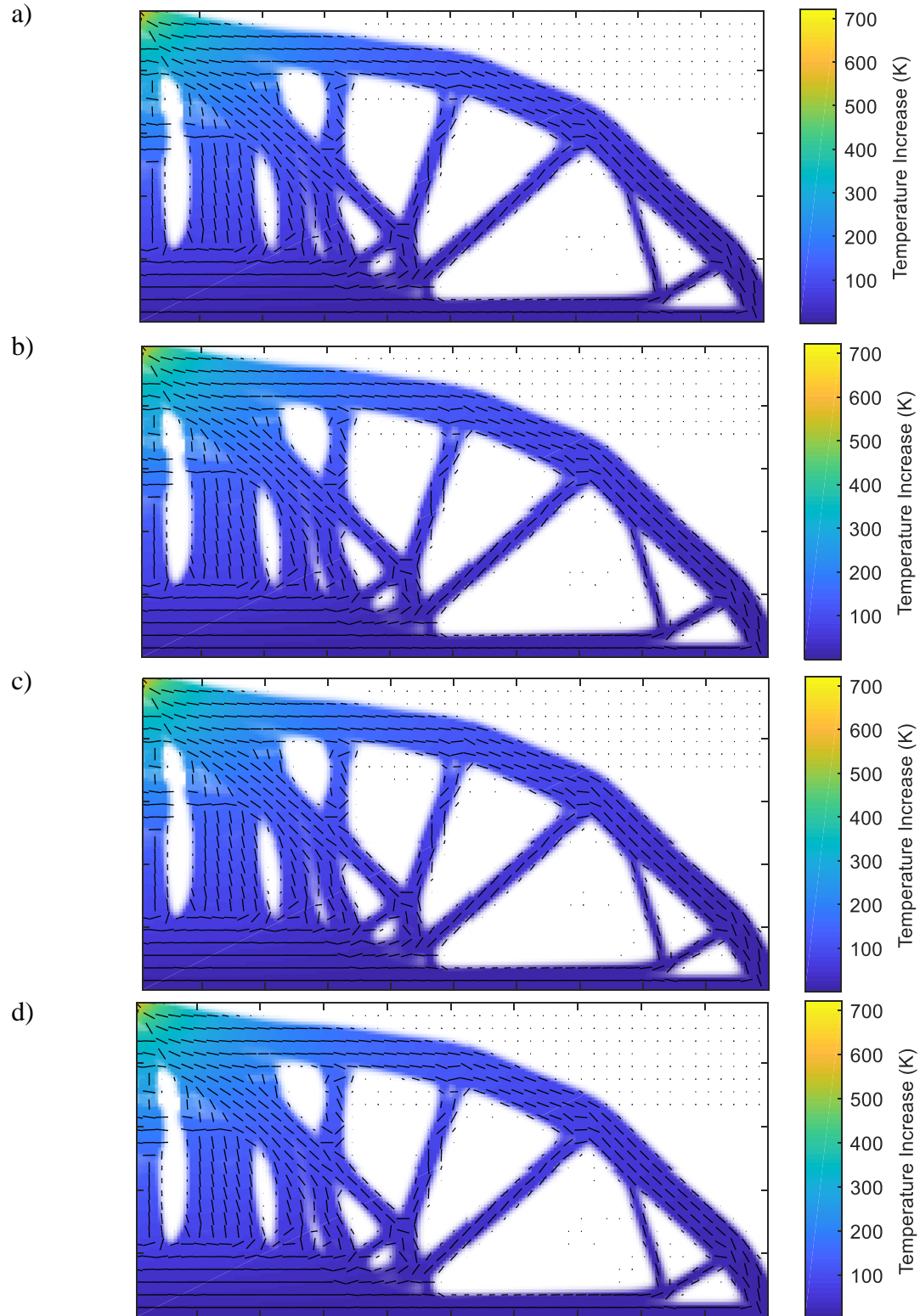


Figure 4.23: Final Topologies for Various Sensitivity-Shifting Functions. The Graphs in a-d Correspond with Shifting Functions in Equations 4.2 – 4.5, Respectively

Adjusting the penalty in the SOMP method affects the behavior of these regions, as well as the final converged structure. The penalty value can be adjusted from the default value of 3 to cause different behavior. In addition, the thermal and mechanical analyses can have different penalties. In that case, the equations for the thermal and mechanical elasticity matrices and the thermal loading equation are rewritten as:

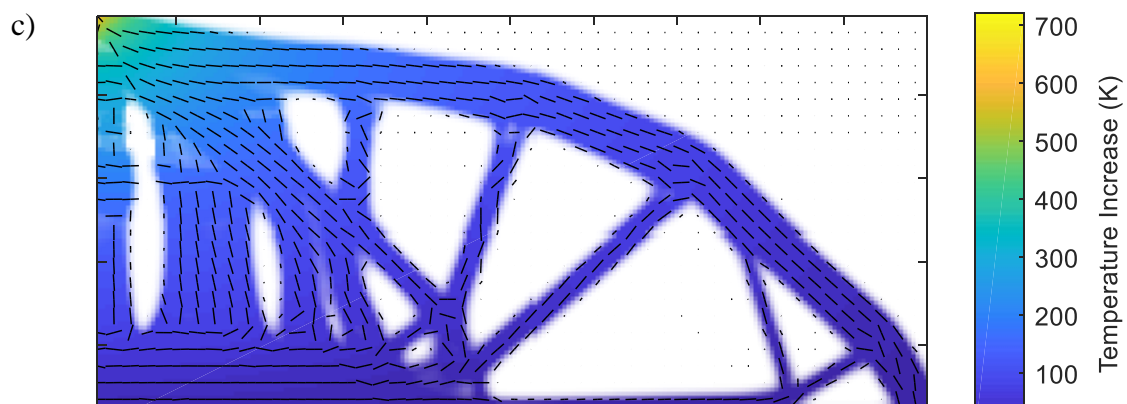
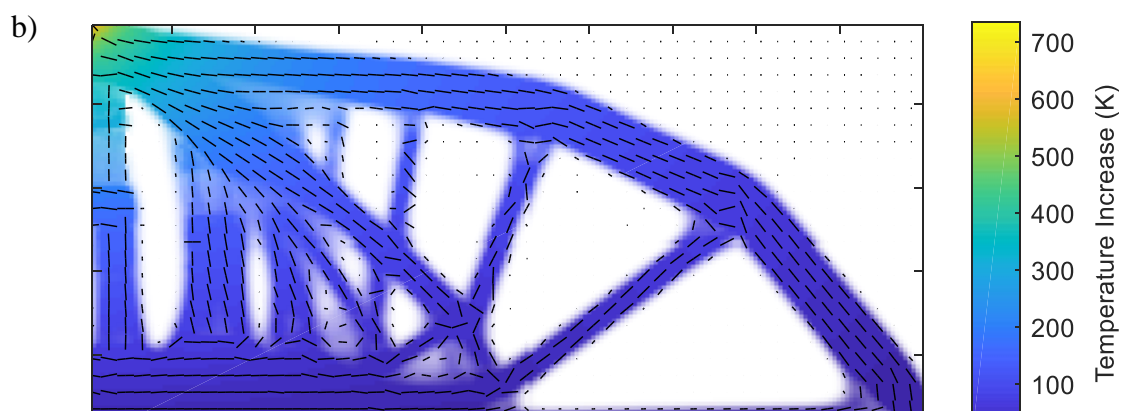
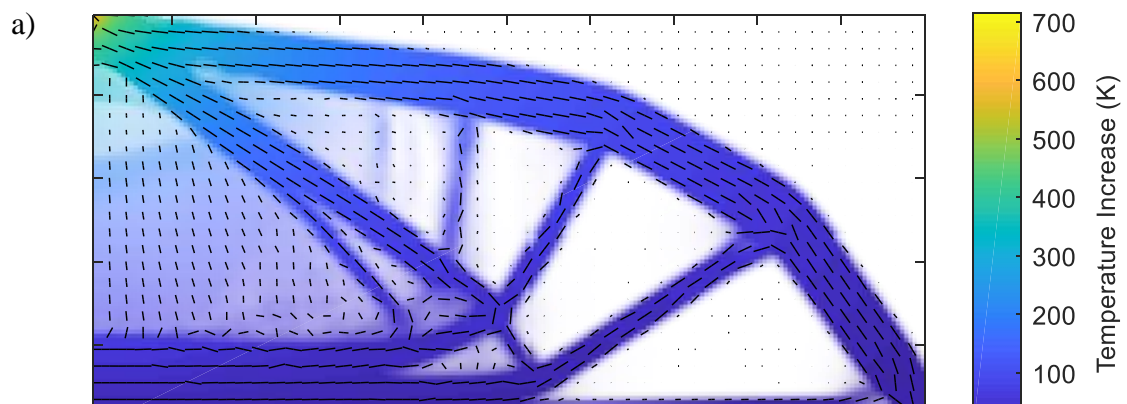
$$\mathbf{K}_{Mi} = x_i^{p_m} \int_{V_i} \mathbf{B}_M^T \mathbf{R}^T(\theta_i) \mathbf{D}_M \mathbf{R}(\theta_i) \mathbf{B}_M dV_i \quad (4.6)$$

$$\mathbf{K}_{Thi} = x_i^{p_{th}} \int_{V_i} \mathbf{B}_{Th}^T T^T(\theta_i) \mathbf{D}_{Th} T(\theta_i) \mathbf{B}_{Th} dV_i \quad (4.7)$$

$$\mathbf{F}_{TE} = x_i^{p_m} \int_{V_i} \mathbf{B}_{Th}^T \mathbf{R}^T(\theta_i) \mathbf{D}_M \begin{Bmatrix} \alpha_x \\ \alpha_y \\ \alpha_{xy} \end{Bmatrix} (\Delta T)_i dV_i \quad (4.8)$$

Redefining the elemental stiffness matrices and thermal force vector as in Equations 4.6-4.8 affects the design sensitivity expressions, although the derivation proceeds identically and will not be shown.

To test the behavior of the optimization under varying penalty parameters, the same design space is used as was used above for the mapping function tests. The mechanical penalty is fixed at $p_m = 3$ and the thermal penalty is allowed to vary between 1 and 5 in successive optimizations. The optimality criterion method is run for 500 iterations, and the results are displayed below.



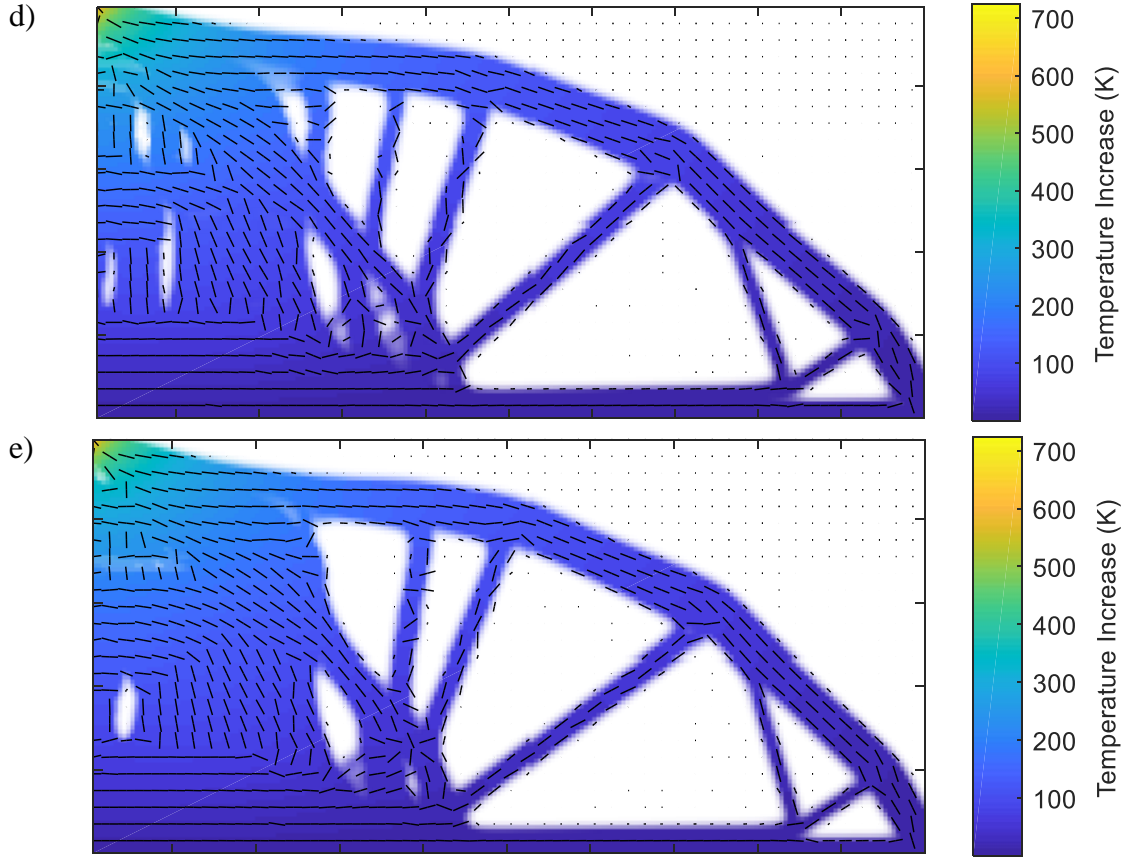


Figure 4.24: Final Topologies for Various Thermal Penalty Values, $p_m = 3$. The Graphs in a-e Correspond with $p_{th} = 1$ to $p_{th} = 5$ Respectively

For low thermal penalties ($p_{th} \leq 2$), the design retains regions of fractional density. Similar behavior is observed in pure mechanical optimization if the mechanical penalty is set low as documented in [22], so the behavior in Figure 4.24 a-b is analogous. The structure does change as the thermal penalty increases beyond 3, but the changes are extremely minor and potentially due to the random variation in initial element orientation. It is thus theorized that a thermal penalty of at least 3 is needed to ensure convergence but there is no observed value in increasing the value of p_{th} beyond 3. The recommended parameters are then $p_m = p_{th} = 3$, and although it was worth

investigating the behavior of different mechanical and thermal penalty values, these are the values used in all prior optimizations.

4.6.3 Mesh Independence and Minimum Member Size

The discretization of the design space into the finite element mesh can introduce two main problems. As the mesh size increases, the finer mesh allows for more complex structures to be produced that take advantage of the greater design freedom. However, with such systems, as increasingly complex structures are generated there is no guarantee that these structures will converge to a consistent design, as is desirable. The mesh and associated density variables are a spatially discrete approximation of the continuously variable design space, and as the approximation better represents the full freedom of the design space the structure should converge to a final design.

Such convergence can be ensured by adding a constraint that prevents the design of features below a certain size. This minimum member size constraint is implemented by applying a filter on the density gradient that replaces each density sensitivity with a weighted average of sensitivities within a given radius.

$$\frac{\partial \widehat{F}}{\partial \rho_i} = \frac{1}{\rho_i \sum_{f=1}^N \widehat{H}_f} \sum_{f=1}^N \widehat{H}_f \rho_f \frac{\partial F}{\partial \rho_f} \quad (4.9)$$

Here, F is the objective function (whether compliance or strain energy) and the parameter \widehat{H}_f is defined by the following.

$$\widehat{H}_f = r_{min} - \text{dist}(e, f) \quad (4.10)$$

The indices e and f represent arbitrary elements, and \widehat{H}_f is only defined if the distance between elements e and f is less than r_{min} . The parameter r_{min} is a tuneable radius that defines the range of the averaging.

The r_{min} parameter prevents the creation of any structures smaller than twice its value. Increasing this radius forces the algorithm to generate coarser structures, which ensures that the design approaches a constant shape as the mesh is refined. In practical consideration it also ensures that no structure will be generated that is too fine to manufacture, so long as r_{min} is set equal to or above the minimum resolution of the manufacturing method under consideration. For polymer additive manufacturing methods like fused-filament fabrication, this maximum resolution would be the width of the extruded bead. The behavior of this minimum member size filter is demonstrated in Figure 4.25. The original full design space of the beam in three-point bending is considered, with the thermal and mechanical loads given above in the full thermomechanical system. Strain energy is considered as the objective function as it generates structures that easily illustrate the behavior of the filter. A mesh of 100×200 elements is used with a volume fraction of 0.5.

The member size is set at lengths of 1, 2, 5, 10, and 20 elements, and the topologies can be observed in Figure 4.25. The increasing size of the member thicknesses can be clearly observed. Under a high minimum member size, the structure cannot converge to a structure with only solid or void elements as averaging a large enough region of density sensitivities causes the associated densities to retain fractional values.

It is also worth noting that the minimum member size constraint prevents checkerboarding. In the first design of Figure 4.25 the structure has a radius small enough that no change to the density sensitivities occurs due to rounding the distance between elements. Large areas of checkerboarding are observed. However, once the radius allows for any averaging of adjacent sensitivities, the designs converge without

checkerboarding. Thus, it is recommended that this filter be used to prevent checkerboarding even if no minimum member size need be considered. The minimum member size filter can be used to prevent checkerboarding without otherwise applying a minimum member size by choosing $1 < r_{min} < 2$.

It can also be shown that when the mesh size increases the designs converge to a constant value under a fixed r_{min} . Note that a fixed r_{min} needs to be expressed in terms of the length of the part, and not in terms of elements as the number of elements within a specific geographic region increases as the mesh is refined. The same system used for Figure 4.25 is considered as the mesh is increased from 100×50 to 150×75 , 200×100 , 300×150 , and 400×200 , with a filter radius of $r_{min} = 0.012 \text{ m}$. The final topologies are presented in Figure 4.26.

As the mesh increases the designs approach the same structure, which supports the convergence of the design under mesh refinement. It is worth considering that, although the minimum member size filter affects the densities, no similar filter is applied to the orientations. As mesh refinement increases, the density field cannot generate structures below the specified radius, but the orientation field can produce more complex structures. A similar filter could be applied to the orientations to bound their complexity as well, although the tests performed here show convergence regardless, indicating that mesh independence is achieved without a filter on the element orientations.

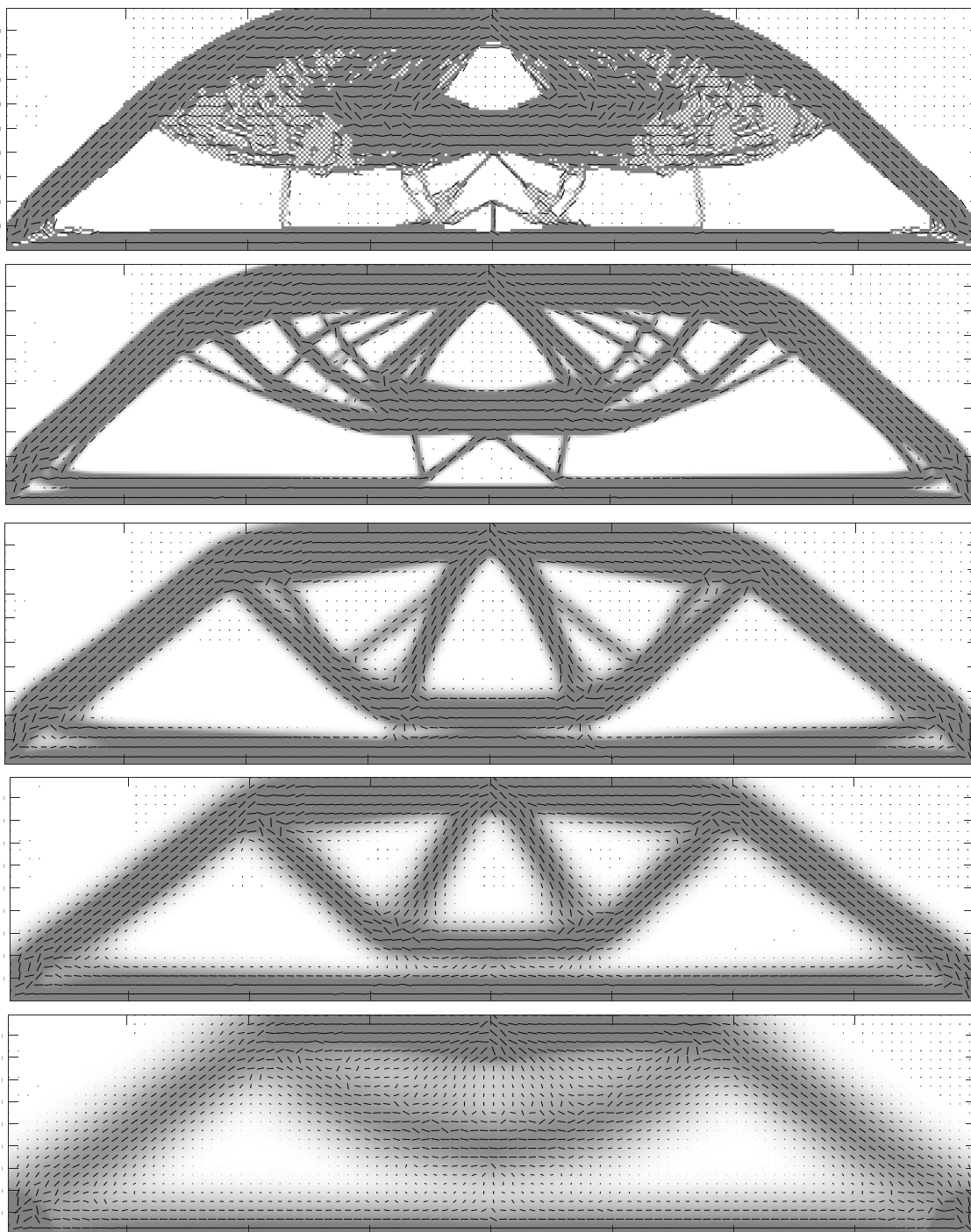


Figure 4.25: Converged Topologies for Filter Radius of $r_{min} \in \{1,2,5,10,20\}$ Pixels, Respectively, from Top to Bottom

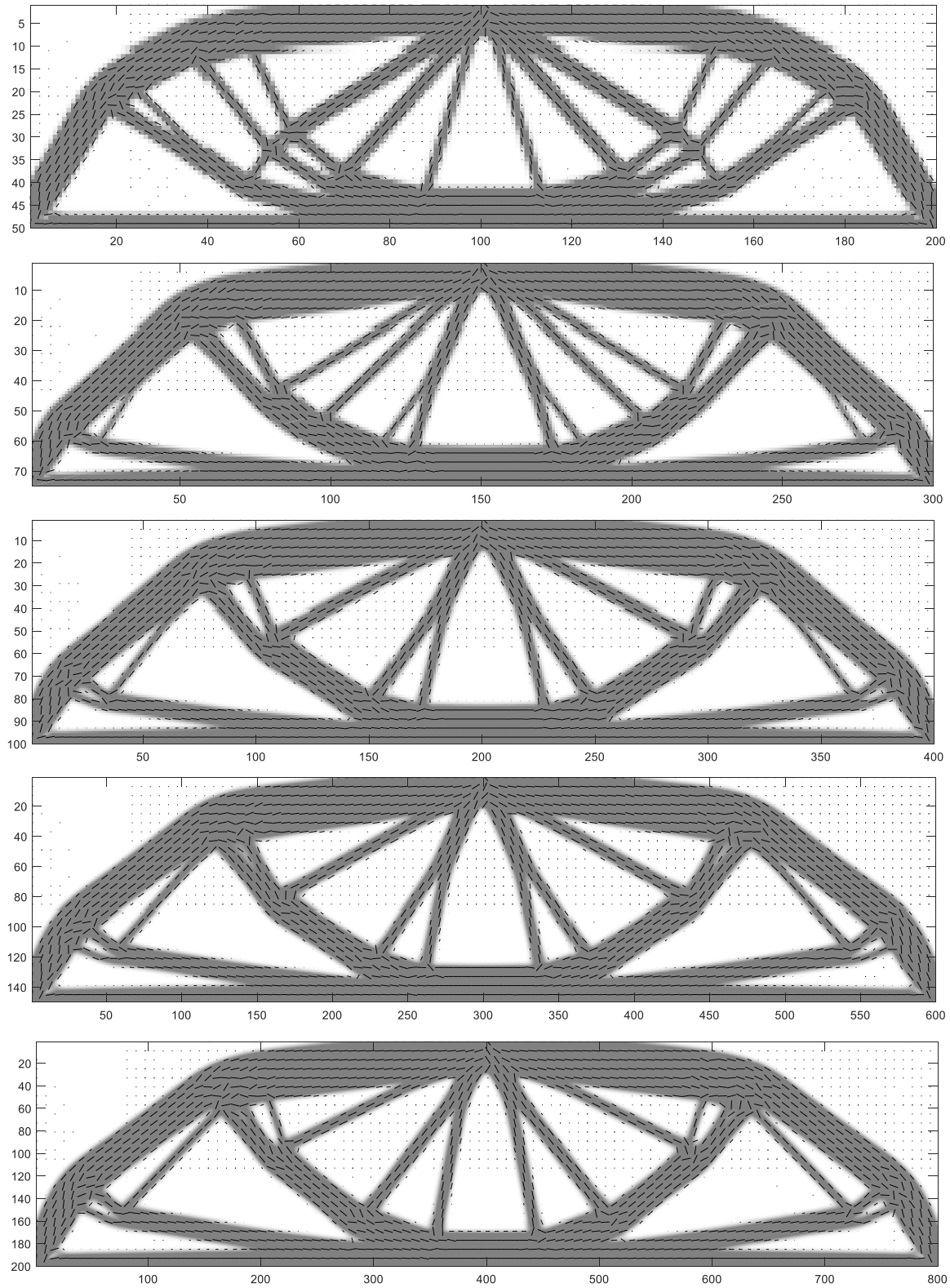


Figure 4.26: Final Topologies for Increasing Mesh Refinement, as Indicated on Each Plot

CHAPTER FIVE

Conclusions

5.1 Summary of Progress

The research presented here implements a topology optimization approach for weakly coupled thermomechanical systems. A two-dimensional design domain with thermal and mechanical equilibrium is defined, and the design of a structure is optimized in this design space. The optimality criterion-based approach and globally convergent method of moving asymptotes are both considered as methods to compute the optimal design. The structure is anisotropic in both the thermal and mechanical models, and the element density and orientation are both considered as design variables.

In the weakly coupled thermomechanical system, both compliance and strain energy can be used as stiffness inverses for the objective function. Both were considered, and while no single metric exists to judge their relative performance, both optimizations converge to feasible structures that can be produced. The compliance-optimized parts do have a lower maximum displacement, which in some cases may make those results superior to strain energy-optimized parts. A parameter study with increasing thermal loading shows that the compliance and strain energy-optimized parts are identical when thermal loading is absent, and that the structures diverge as the thermal load dominates the structure. The strain energy optimization resembles the pure mechanical structure in all cases considered here, while the compliance-optimized parts change more drastically to distribute the thermal loading. It was shown by computing the load contribution of the

thermal loading that the compliance-optimized parts are more effective at distributing the thermal load.

Two separate methods were used for the optimization here. Both are widely used in topology optimization research, and each has different advantages. The optimality criterion method converges quickly, but the heuristic nature of the update method is designed to accommodate only density as the design variable, and it only allows for a single constraint. It was necessary to create a separate step to optimize the element orientations for OC optimizations in this work, which demonstrate smooth and rapid convergence, but the additional orientation optimization step is a significant modification to the method. The GCMMA method needed no such modifications, as it was designed to optimize over a general design space with an arbitrary number of constraints. However, the final topologies showed poorer orientation alignment and in at least one case the GCMMA method converged to a local minimum with poor performance. For the specific anisotropic weakly coupled thermomechanical model used, the set of design variables, constraint, and objective function, the OC method is preferred by the authors. It is worth noting that the GCMMA method uses many tunable parameters and it is possible that the issues encountered were due to the author's lack of familiarity with those. For more complex systems, as must be adopted to fully capture the complete additive manufacturing process as described below, the GCMMA algorithm may be better suited to optimizing the structure as additional constraints and design variables are required for more complete models. In summary, each algorithm has significant strengths and weaknesses, but the OC method suits the specific system considered here while the GCMMA method may be more useful in subsequent works.

5.2 Production of Structures

The final topologies can be produced in proof-of-concept parts to demonstrate that the structure generated in this work can be feasibly produced. A Matlab code obtained from Dr. Keith Ma generates a series of streamlines with defined spacing that fill the converged topology while traveling along the orientation field (Figure 5.1b). A custom Matlab code created in-house then generates a gcode file that prints the streamlines in identical layers, which is converted to x3g code and printed in a Makerbot + with PLA filament (Figure 5.1c). The process is illustrated below in Figure 5.1.

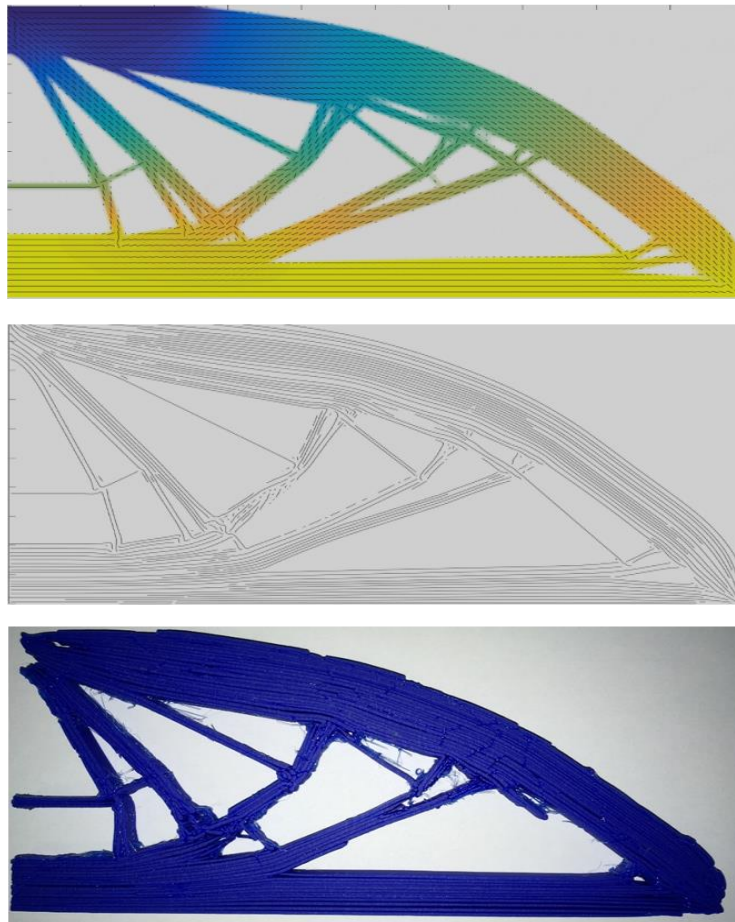


Figure 5.1: Proof-of-Concept Part Production Process

Note that the minor inaccuracies in the final part may be resolved by applying a higher minimum member size in the sensitivity filter. Observe that structures produced in this way are proof-of-concept parts that show a viable way of manufacturing topology optimization results, but the thermal loading experienced in the printing process does not match the steady-state thermal analysis in the model, as discussed below in Section 5.3.2. Thus, while the parts produced have the same structure as the topology optimized results, they may perform differently under loading.

5.3 Future Work

This work has advanced the state of the art in modeling the full complexity of the additive manufacturing process, but significant work remains before a fully accurate model can be completed. Below are the next steps that the authors think is most relevant, although the list is far from exhaustive.

5.3.1 Three-Dimensional Code

The models used in this work were all two-dimensional. This allowed for easy presentation of results and reasonably computationally efficient models. To design structures for actual usage, however, three-dimensional structures are much more useful. Many previous works have used three dimensional models, including prior research at Baylor [75], and the methods developed here can be extended to optimize over such structures with minor changes in the methods. The primary necessary alteration is replacing the two-dimensional meshes with three-dimensional meshes. The algorithm itself need not be changed, although note that element orientations can take on more complex distributions in three-space, and depending on the additive manufacturing

method considered, may have different restrictions. In particular, standard three-axis fused-filament fabrication devices can only extrude beads in the x-y plane but printing systems using more axes of movement can allow for print orientation in the direction of an arbitrary vector in three-space.

5.3.2 Transient Thermal Loads

The steady-state thermal loading here allows for a design-dependent temperature field that generates thermal stresses for the mechanical analysis. Such weakly coupled design-dependent loading is a step beyond previous research, but it does not fully capture the complexity of the additive manufacturing process. To fully represent the cooling process, transient thermal loading must be used. This transient thermal loading is significantly more computationally intensive, and the design sensitivity derivations will need to be derived in this new system to model the time-dependent loading. Additional factors, such as stress relation, must be included as well.

The model used here, while simplified from the full complexity of the fused-filament fabrication cooling process, can still be applied directly in real-world applications. The weakly coupled model represents structures undergoing steady-state thermal and mechanical loading, such as an automotive engine mount or aircraft exhaust panel under constant operating conditions. Any component experiencing mechanical loading and a temperature change can be optimized using the method described above, regardless of whether it is additively manufactured.

5.3.3 Toolpath Optimization

The transient thermal loading required to fully consider the additive manufacturing process is dependent not only on the location of the material and the orientation of its properties. The order that the material is deposited determines how it heats nearby material, and what boundary conditions each element experiences, and modeling this can be extremely complex.

As discussed above, the structural results can be produced by generating a series of toolpaths that follow the element orientations. The order that the toolpaths are printed in each layer will determine the thermal loading, so the ordering of the set of toolpaths must be considered as design variables. Optimizing this ordering may be challenging, as the toolpaths are defined in terms of other design variables, and it may be beneficial to sacrifice some mechanical strength by deviating toolpaths from the orientation field to improve the cooling process. Modeling this full system will take significant modification from the method presented here.

5.3.4 Physical Testing of Components

The results presented here are purely computational, and physical testing has yet to be done to verify them. As the thermal loading considered does not fully capture the additive manufacturing production process, no accurate testing can yet be done. While the authors are confident in presenting the work here as an optimization method, conducting physical testing will ensure that the model is accurate and captures the complexity of the system. Several simplifying assumptions were used in this model, such as geometric and material linearity, that toolpath breaks do not affect the performance,

and that material orientation has no constraints on derivative magnitude. Physical testing will indicate whether any additional factors need to be included.

APPENDIX

APPENDIX

Code Used

The following code was used to perform the tests present in the work. Separate codes were used for the OC and GCMMA optimizations, and they are presented sequentially. Below is the OC code. It began from Sigmund's 99-line compliance minimization code [22], but nearly every component has been significantly modified.

```
%% Optimality Criterion Topology Optimization Code
format compact
%% Initialization
clear
clc
close all
video = 0;
% Open Video
if video == 1
v = VideoWriter('conj_grad_test3');
open(v)
end
% Changeable variables
%Opt_Var = 'Strain_Energy';
Opt_Var = 'Compliance';
nelx = 200; % Number of cells in the x-direction
nely = 100; % Number of cells in the y-direction
%fixed_densities = 1:nely:10*(nely+1);
fixed_densities = [];
volfrac = .5; % volume fraction
penal_m = 3; % Mechanical density penalty
penal_h = 3; % Thermal density penalty

% Constants
Erat = 10; % Ratio of in-line modulus to perpendicular modulus
xl = .10; % length of x-side in m
length = xl/nelx; %length of one unit cell edge in meters
E = 1.79E9; %Young's Modulus in weakest direction
alpha = 7E-5; %1/C Coefficient of thermal expansion
alphanat = 1.2; % Ratio of coefficients of thermal expansion
ksmall= 0.13; % Conduction coefficient, for ABS plastic, min value
krat = 2; % Ratio of in-line conduction coefficient to perpendicular conduction
coefficient
rmin = nelx/82;
% Element Properties
x(1:nely,1:nelx) = volfrac; %All units have same base density
x(fixed_densities) = 1; % All elements that are fixed are set to solid
angle(1:nely,1:nelx) = 0; % all orientations are set to zero
%angle = rand(nely,nelx)*pi; % all orientations are randomly assigned
temp(1:nely,1:nelx) = 0;
vmstress(1:nely,1:nelx) = 0;

loop = 0;
change = 1;
xold = zeros(nely,nelx);
c_record = [];
```

```

SE_record = [];
change_rec = [];

%% START ITERATION
while change > 0.001 && loop < 2000
    tic;
    % Increment counters
    loop = loop + 1;
    xrealold = xold;
    xold = x;
    % FEA
    [T,K_ff,freedofs]=thermal_FEA(nelx,nely,x,angle,penal_h,ksmall,krat,length,1);
    [thermal_forces, DF_DT] =
thermal_stresses(T,x,angle,nely,nelx,alpha,alpharat,length,E,Erat,penal_m);
    [U,U_th,U_m]=mechanical_FEA(nelx,nely,x,angle,penal_m,E,Erat,thermal_forces,length);
    lambda = zeros(1,(nelx+1)*(nely+1));
    lambda(:,freedofs) = (U'*DF_DT(:,freedofs))/K_ff;
    % OBJECTIVE FUNCTION AND SENSITIVITY ANALYSIS
    c = 0;
    SE = 0;
    dc= zeros(nely,nelx);
    d_SE = zeros(nely,nelx);
    for ely = 1:nely
        for elx = 1:nelx
            n1 = (nely+1)*(elx-1)+ely; %
            n2 = (nely+1)* elx +ely; %
            % DOF selected for mechanical analysis
            edof = [2*n1-1;2*n1; 2*n2-1;2*n2; 2*n2+1;2*n2+2; 2*n1+1;2*n1+2];
            edof_T = [n1;n2;n2+1;n1+1];
            Ue = U(edof,1); % nodes are ccw from bottom left
            Ue_m = U_m(edof,1);
            Ue_t = U_th(edof,1);
            % DOF selected for thermal analysis
            T_i = T([n1;n2;n2+1;n1+1],1); % ccw from bottom left
            % Mechanical element created
            KE = lk(angle(ely,elx),E,Erat,length);
            KE2 = lk(angle(ely,elx) + 0.001,E,Erat,length);
            dKE_da = (KE2 - KE)/0.001;
            % Thermal element created
            KE_th = lk_th(angle(ely,elx),ksmall,krat,length);
            KE_th2 = lk_th(angle(ely,elx) + 0.001,ksmall,krat,length);
            dKE_th_da = (KE_th2 - KE_th)/.001;
            % Compliance summed
            c = c + 1/2*x(ely,elx)^penal_m*Ue'*KE*Ue;
            % Strain Energy
            SE = SE + 1/2*x(ely,elx)^penal_m*(Ue'*KE*Ue - 2*Ue'*KE*Ue_t + Ue_t'*KE*Ue_t);
            % Derivative of compliance with respect to density computed
            TL =
thermoload(x(ely,elx),angle(ely,elx),E,Erat,alpha,alpharat,T_i,length,penal_m);
            dTL_dxi = TL*penal_m/x(ely,elx); %
            dTL_dai = (thermoload(x(ely,elx),angle(ely,elx) +
.001,E,Erat,alpha,alpharat,T_i,length,penal_m) - TL)/.001;
            DF_Dxi = ksmall/ksmall*lambda(edof_T)*KE_th*T_i;
            dc(ely,elx) = penal_m*x(ely,elx)^(penal_m-1)*Ue'*KE*Ue - 2*Ue'*dTL_dxi +
2*penal_h*x(ely,elx)^(penal_h-1)*DF_Dxi;
            % Derivative of strain energy with respect to density computed
            d_SE(ely,elx) = -0.5*penal_m*x(ely,elx)^(penal_m-1)*(-Ue'*KE*Ue +
2*Ue_t'*KE*Ue - Ue_t'*KE*Ue_t);
            % Angle optimization:
            nangle = mod(a_opt(angle(ely,elx),E,Erat,Ue,Ue_t,Opt_Var,length),pi);
            ml = abs(angle(ely,elx) - nangle)*0.1;
            if abs(angle(ely,elx) - nangle) < pi/2
                %disp('Case Normal')
                angle(ely,elx) = min(angle(ely,elx) + ml,max(angle(ely,elx)-ml,nangle));
            % Nothing funky happens with mod, move toward nangle
            elseif angle(ely,elx) < nangle
                %disp('Case Go Below Zero')
                angle(ely,elx) = mod(min(angle(ely,elx) + ml,max(angle(ely,elx)-
ml,nangle-pi)),pi); % Fastest way is to move down to get to nangle
            else
                %disp('Case Go Above Pi')

```

```

        angle(ely,elx) = mod(min(angle(ely,elx) + ml,max(angle(ely,elx)-
ml,nangle+pi)),pi); % Fastest way is to move up to get to nangle
    end
    % Stress Determination
    [strain,stress,vm]=stress1(angle(ely,elx),E,Erat,Ue,length);
    vmstress(ely,elx) = vm;
end
end
% Plot Goals
figure(2)
c_record(end+1) = c;
SE_record(end+1) = SE;
if size(c_record,2) > 10
    subplot(5,3,13)
    plot(c_record(10:end))
    title('Compliance')
    subplot(5,3,14)
    plot(SE_record(10:end))
    title('Strain Energy')
    subplot(5,3,15)
    plot(change_rec(10:end))
    title('Total Change')
end

% FILTERING OF SENSITIVITIES
switch Opt_Var
case 'Compliance'
    dc = check(nelx,nely,rmin,x,dc); %mesh-independence check
case 'Strain_Energy'
    d_SE = check(nelx,nely,rmin,x,d_SE); %mesh-independence check
end

% DESIGN UPDATE BY THE OPTIMALITY CRITERIA METHOD
% OC Method
maxneg = max(max(abs(dc.*(dc <= 0))));
if maxneg > 0
    dc = dc.*(dc > 0);
end

switch Opt_Var
case 'Compliance'
    x = OC_new(nelx,nely,x,volfrac,dc,fixed_densities); % Updates density using
current density and derivative
case 'Strain_Energy'
    x = OC_new(nelx,nely,x,volfrac,d_SE,fixed_densities); % Updates density using
current density and derivative
end
time = toc;
% PRINT RESULTS
change = max(max(abs(x-xold))); % There must be a better parameter than this
change_rec(end+1) = sum(sum(abs(x-xold)));
skipchange = max(max(abs(x-xrealold)));
disp([' It.: ' sprintf('%4i',loop) ' Compliance: ' sprintf('%10.5f',c) ...
' Strain Energy: ' sprintf('%10.5f',SE) ...
' Vol.: ' sprintf('%6.5f',sum(sum(x))/(nelx*nely)) ...
' ch.: ' sprintf('%6.3f',change) sprintf('%6.3f',skipchange) ' Time: '
sprintf('%2.0f',floor(time/60)) 'm ' sprintf('%2.2f',mod(time,60)) 's' ...
' Total Change: ' sprintf('%6.3f',sum(sum(abs(x-xold))))])
% Plot densities
temp = reshape(T,nely+1,nelx+1);
el temp = .25*(temp(1:end-1,1:end-1)+temp(2:end,1:end-1)+temp(1:end-
1,2:end)+temp(2:end,2:end));

if video == 1
    figure(7)
else
    subplot(5,3,[1,2,3,4,5,6])
end

I = imagesc([flip(el_temp)' el_temp]);

```

```

colormap parula
colorbar
set(I, 'AlphaData', [flip(x)' x]);
hold on
Xlen = 1:2*nex;
Ylen = 1:nely;
[Xset,Yset] = meshgrid(Xlen,Ylen);
xvec = sin(pi/2 - angle).*x; % switched from usual because angle is measured from
y-axis
yvec = cos(pi/2 - angle).*x; % This is because y comes first in the ordered pairs
for density
xvec = [flip(-xvec)' xvec];
yvec = [flip(yvec)' yvec];
spacing = ceil(max(nex,nely)/100);
quiver(Xset(1:spacing:end,1:spacing:end),Yset(1:spacing:end,1:spacing:end), ...
.5*spacing*xvec(1:spacing:end,1:spacing:end),.5*spacing*yvec(1:spacing:end,1:spacing:end)
), 'MaxheadSize',0, 'Color',[0 0 0], 'AutoScale','off')
quiver(Xset(1:spacing:end,1:spacing:end),Yset(1:spacing:end,1:spacing:end), ...
-.5*spacing*xvec(1:spacing:end,1:spacing:end),-
.5*spacing*yvec(1:spacing:end,1:spacing:end), 'MaxheadSize',0, 'Color',[0 0
0], 'AutoScale','off')

axis equal
axis tight
axis([1 2*nex 1 nely])
title('Part Design')
hold off
pause(.2)

disps = (U(1:2:end).^2 + U(2:2:end).^2).^5;
disps = reshape(disps,nely+1,nex+1);
if video == 1
figure(4)
else
subplot(5,3,[7,8,9,10,11,12])
end
disps = 1/4*(disps(1:end-1,1:end-1) + disps(1:end-1,2:end) + disps(2:end,1:end-1) +
disps(2:end,2:end));
colormap parula
J = imagesc([flip(vmstress)',vmstress]);
set(J, 'AlphaData', [flip(x)' x]);
colorbar
axis equal
axis tight
title('Von Mises Stress')
colormap winter
pause(0.2)
hold off
%keyboard
if video == 1
figure(7)
pause(.2)
if loop == 1
pause(2)
end
frame = getframe;
writeVideo(v,frame);
writeVideo(v,frame);
writeVideo(v,frame);
writeVideo(v,frame);
writeVideo(v,frame);
pause(.2)
end
end
if video == 1
close(v)
end

```

```

function [U_th, K_ff,
freedofs]=thermal_FEA(nelx,nely,x,angle,penal,ksmall,krat,length,inv_need)
% Material Properties
F = sparse((nely+1)*(nelx+1),1); % F has units of W/m^2
U_th = sparse((nely+1)*(nelx+1),1); % Temperature has units of K
kval = zeros(1,16*nelx*nely);
kx = zeros(1,16*nelx*nely);
ky = zeros(1,16*nelx*nely);
int = 1;
for elx = 1:nelx %makes stiffness matrix
    for ely = 1:nely
        n1 = (nely+1)*(elx-1)+ely;
        n2 = (nely+1)* elx +ely;
        edof = [n1;n2;n2+1;n1+1];
        [KE_th] = lk_th(angle(ely,elx),ksmall,krat,length);
        kval(16*(int-1)+1:16*int) = (0.001+0.999*x(ely,elx)^penal)*KE_th;
        kx(16*(int-1)+1:16*int) = [edof edof edof edof];
        ky(16*(int-1)+1:16*int) = repelem(edof,4);
        int = int+1;
    end
end
K = sparse(kx,ky,kval);
% DEFINE LOADS AND SUPPORTS (HALF MBB-BEAM) this is where
% F represents the heat flux in
%F(1:nely) = 1e-8; % Center line, flux set to zero for symmetry
F(end-nely:end) = 0; % Outside vertical edge heat flux in
%F(nelx+1:nely+1:(nely+1)*(nelx+1)) = 100; % Bottom Edge
%F((nelx+1):nely+1:(nely+1)*(nelx+1)) = 10; % Bottom Edge, right half
%F(1:nely+1:(nely+1)*(nelx+1)) = 1; % top edge
%%%
F(1) = 3e-6;
%%%
%F((nely+1)*(nelx+1)) = 3e-6;
fixeddofs = [];
fixeddofs = union(fixeddofs,[nely+1:nely+1:(nelx+1)*(nely+1)]); % bottom edge
U_th([nely+1:nely+1:(nelx+1)*(nely+1)],:)= 0;

%fixeddofs = union(fixeddofs,[1:nely+1]); % Center edge (symmetry line)
%U_th([1:nely+1],:)= 0;

%fixeddofs = union(fixeddofs,1:floor(nely/2)+1); % Top half of center edge
%U_th(fixeddofs,:)= 0;

%fixeddofs = union(fixeddofs,[(nely+1)*nelx+1:(nelx+1)*(nely+1)]); % Right edge
%U_th([(nely+1)*nelx+1:(nelx+1)*(nely+1)],:)= 0;

%fixeddofs = union(fixeddofs,[(nely+1)*nelx+1+floor(nelx/2):(nelx+1)*(nely+1)]); % Bottom
half of right edge
%U_th([(nely+1)*nelx+1+floor(nelx/2):(nelx+1)*(nely+1)],:)= 0;

%fixeddofs = union(fixeddofs,[1:nely+1:(nely+1)*(nelx+1)]); % Top edge
%U_th([1:nely+1:(nely+1)*(nelx+1)],:)= 10000;

%fixeddofs = union(fixeddofs,(nelx+1)*(nely+1));
%U_th((nelx+1)*(nely+1)) = 0;
%fixeddofs = (nelx+1)*(nely+1);
%RU_th(fixeddofs) = 0;
% U_th(1) = 0;
% U_th((nelx+1)*(nely+1)) = 0;
alldofs = 1:(nely+1)*(nelx+1);
freedofs = setdiff(alldofs,fixeddofs);
%F(1,1) = 5E-5;
% fixeddofs = union(1:2:2*(nely+1),2*(nelx+1)*(nely+1));
% SOLVING
if inv_need == 1
    U_th(freedofs,:) = K(freedofs,freedofs)\ (F(freedofs,:)-
K(freedofs,fixeddofs)*U_th(fixeddofs,:));
else

```

```

        U_th(freedofs,:) = K(freedofs,freedofs)\ (F(freedofs,:) -
K(freedofs,fixeddofs)*U_th(fixeddofs,:));
end
K_ff = K(freedofs,freedofs);

function [KE]=lk_th(angle,ksmall,krat,length)
% Based on the two-point Gauss Quadrature for thermal systems.
Ky =ksmall;
Kx = ksmall*krat;
varset = 1/sqrt(3)*[1 1;1 -1;-1 1;-1 -1];
KE = zeros(4,4);
c = cos(angle)^2;
s = sin(angle)^2;
cs = cos(angle)*sin(angle);
rDr = [Kx*c+Ky*s,cs*(Ky-Kx),0;cs*(Ky-Kx),Kx*s+Ky*c,0;0,0,0];
for j = 1:4
    nu = varset(j,1);
    eta = varset(j,2);
    B = 1/4*[-1+nu 1-nu 1+nu -1-nu; -1+eta -1-eta 1+eta 1-eta; 0 0 0 0];
    KE = KE + B'*rDr*B;
end
end

function [ TL, DF_DT ] =
thermal_stresses(t,density,angle,nely,nelx,alpha,alpharat,length,E,Erat,penal)
%Given a two-dimensional temperature distribution, this function computes
%the thermal forces.
% Inputs
% -t is the y-by-x temperature matrix
% -scale is the length of one unit cell in meters
TL = zeros(2*(nely+1)*(nelx+1),1);
DF_DT_x = zeros(1,32*nelx*nely);
DF_DT_y = zeros(1,32*nelx*nely);
DF_DT_val = zeros(1,32*nelx*nely);
int = 1;
for i = 1:nelx
    for j = 1:nely
        n1 = (nely+1)*(i-1)+j;
        n2 = (nely+1)* i +j;
        edof = [2*n1-1 2*n1 2*n2-1 2*n2 2*n2+1 2*n2+2 2*n1+1 2*n1+2]; % For reference
        edof_T = [n1;n2;n2+1;n1+1]; % For reference
        TL(edof) = TL(edof) +
        thermoload(density(j,i),angle(j,i),E,Erat,alpha,alpharat,t(edof_T),length,penal);
        DF_DT_val(32*(int-1)+1:32*int) =
        dTL_dT(density(j,i),angle(j,i),E,Erat,alpha,alpharat,length,penal);
        DF_DT_x(32*(int-1)+1:32*int) = [edof edof edof edof];
        DF_DT_y(32*(int-1)+1:32*int) = repelem(edof_T,8);
        int = int+1;
    end
end
DF_DT = sparse(DF_DT_x,DF_DT_y,DF_DT_val);
end

function TL = thermoload(density,angle,E,Erat,alpha,alpharat,temps,length,penal)
% Based on the two-point Gauss Quadrature
Ey = E;
Ex = Erat*E;
nuxy = .36;
nuyx = nuxy*Ey/Ex;

varset = 1/sqrt(3)*[1 1;1 -1;-1 1;-1 -1];
TL = zeros(8,1);
D = [Ex/(1-nuxy*nuyx) nuxy*Ey/(1-nuxy*nuyx) 0; nuxy*Ey/(1-nuxy*nuyx) Ey/(1-nuxy*nuyx) 0;
0 0 Ex/(2*(1+nuxy))];
rotation = [cos(angle)^2 sin(angle)^2 -2*sin(angle)*cos(angle); ...
            sin(angle)^2 cos(angle)^2 2*sin(angle)*cos(angle);
```



```

        cos(angle)*sin(angle) -cos(angle)*sin(angle) cos(angle)^2 - sin(angle)^2];
rDr = rotation*D*rotation';
% Anisotropic coefficient of thermal expansion
ax = alpha*alphanat;
ay = alpha;
c = cos(angle);
s = sin(angle);
alphaset = [ax*c^2+ay*s^2;ax*s^2+ay*s^2;c*s*(ax-ay)];
for j = 1:4
    % Get Temperature
    nu = varset(j,1);
    eta = varset(j,2);
    T = 1/4*[(1-nu)*(1-eta) (1-eta)*(1+nu) (1+eta)*(1+nu) (1+eta)*(1-nu)]*temps;
    B = 1/4*[-1+nu 0 1-nu 0 1+nu 0 -1-nu 0; 0 -1+eta 0 -1-eta 0 1+eta 0 1-eta; ...
        -1+eta -1+nu -1-eta 1-nu 1+eta 1+nu 1-eta -1-nu];

    TL = TL + length^2/4*density^penal*B'*rDr*[alphaset]*T; %
end
end

function der = dTL_dT(density,angle,E,Erat,alpha,alphanat,length,penal)
% Based on the two-point Gauss Quadrature
Ey = E;
Ex = Erat*E;
nuxy = .36;
nuyx = nuxy*Ey/Ex;

varset = 1/sqrt(3)*[1 1;1 -1;-1 1;-1 -1];
der = zeros(8,4);
D = [Ex/(1-nuxy*nuyx) nuxy*Ey/(1-nuxy*nuyx) 0; nuxy*Ey/(1-nuxy*nuyx) Ey/(1-nuxy*nuyx) 0;
0 0 Ex/(2*(1+nuxy))];
rotation = [cos(angle)^2 sin(angle)^2 -2*sin(angle)*cos(angle); ...
    sin(angle)^2 cos(angle)^2 2*sin(angle)*cos(angle); ...
    cos(angle)*sin(angle) -cos(angle)*sin(angle) cos(angle)^2 - sin(angle)^2];
rDr = rotation*D*rotation';

ax = alpha*alphanat;
ay = alpha;
c = cos(angle);
s = sin(angle);
alphaset = [ax*c^2+ay*s^2;ax*s^2+ay*s^2;c*s*(ax-ay)];
for j = 1:4
    % Get Temperature
    x = varset(j,1);
    y = varset(j,2);
    %NT = 1/4*[(1-x)*(1-y) (1+y)*(1-x) (1+y)*(1+x) (1-y)*(1+x)];
    NT = 1/4*[(1-x)*(1-y) (1-y)*(1+x) (1+y)*(1+x) (1+y)*(1-x)];
    %
    nu = varset(j,1);
    eta = varset(j,2);
    B = 1/4*[-1+nu 0 1-nu 0 1+nu 0 -1-nu 0; 0 -1+eta 0 -1-eta 0 1+eta 0 1-eta; ...
        -1+eta -1+nu -1-eta 1-nu 1+eta 1+nu 1-eta -1-nu];

    der = der + (length/2)^2*density^penal*B'*rDr*[alphaset]*NT;
end

end

function [U, U_th,
U_m]=mechanical_FEA(nelx,nely,x,angle,penal,E,Erat,thermal_forces,length)
F = sparse(2*(nely+1)*(nelx+1),1);
U = zeros(2*(nely+1)*(nelx+1),1);
U_th = zeros(2*(nely+1)*(nelx+1),1);
U_m = zeros(2*(nely+1)*(nelx+1),1);

```

```

kval = zeros(1,64*nex*nely);
kx = zeros(1,64*nex*nely);
ky = zeros(1,64*nex*nely);
int = 1;
for elx = 1:nex %makes stiffness matrix
    for ely = 1:nely
        n1 = (nely+1)*(elx-1)+ely;
        n2 = (nely+1)* elx +ely;
        edof = [2*n1-1 2*n1 2*n2-1 2*n2 2*n2+1 2*n2+2 2*n1+1 2*n1+2];
        KE = lk(angle(ely,elx),E,Erat,length);
        kval(64*(int-1)+1:64*int) = x(ely,elx)^penal*KE;
        kx(64*(int-1)+1:64*int) = [edof edof edof edof edof edof edof edof];
        ky(64*(int-1)+1:64*int) = repelem(edof,8);
        int = int+1;
    end
end
K = sparse(kx,ky,kval);
% DEFINE LOADS AND SUPPORTS (HALF MBB-BEAM)
F(2,1) = F(2,1) -500; %
%F(2:2*nely+2:10*nely+12) = F(2:2*nely+2:10*nely+12) - 100/5;
%fixeddofs = union(1:2:2*(nely+1),[2*(nex+1)*(nely+1),2*(nex+1)*(nely+1)-1]);
fixeddofs = union(1:2:2*(nely+1),[2*(nex+1)*(nely+1)]);
alldofs = 1:2*(nely+1)*(nex+1);
freedofs = setdiff(alldofs,fixeddofs);
freedofs2 = setdiff(alldofs,[1,2]);
% SOLVING

U(freedofs,:) = K(freedofs,freedofs)\(F(freedofs,:) + thermal_forces(freedofs,:));
U_m(freedofs,:) = K(freedofs,freedofs)\F(freedofs,:);
U_th(freedofs2,:) = K(freedofs2,freedofs2)\thermal_forces(freedofs2,:);

U(fixeddofs,:)= 0;

function [KE]=lk(angle,E,Erat,length)
% Based on the two-point Gauss Quadrature
Ey = E;
Ex = Erat*E;
nuxy = .36;
nuyx = nuxy*Ey/Ex;

varset = 1/sqrt(3)*[1 1;1 -1;-1 1;-1 -1];
KE = zeros(8,8);
D = [Ex/(1-nuxy*nuyx) nuxy*Ey/(1-nuxy*nuyx) 0; nuxy*Ey/(1-nuxy*nuyx) Ey/(1-nuxy*nuyx) 0;
0 0 Ex/(2*(1+nuxy))];
rotation = [cos(angle)^2 sin(angle)^2 -2*sin(angle)*cos(angle); ...
            sin(angle)^2 cos(angle)^2 2*sin(angle)*cos(angle);
            cos(angle)*sin(angle) -cos(angle)*sin(angle) cos(angle)^2 - sin(angle)^2];
rDr = rotation*D*rotation';
for j = 1:4
    nu = varset(j,1);
    eta = varset(j,2);
B = 1/4*[-1+nu 0 1-nu 0 1+nu 0 -1-nu 0; 0 -1+eta 0 -1-eta 0 1+eta 0 1-eta; ...
-1+eta -1+nu -1-eta 1-nu 1+eta 1+nu 1-eta -1-nu];
KE = KE + B'*rDr*B;
end
end

function [angle]=a_opt(angle,E,Erat,Ue,Ue_th,Opt_Var,length)
% We use the newton-raphson method to solve:
diff = 1;
arec = [angle];
while diff > 1E-2
    switch Opt_Var
        case 'Compliance'
            backward = -Ue'*lk2(angle-0.001,E,Erat,length)*Ue;

```

```

        center = -Ue'*lk2(angle,E,Erat,length)*Ue;
        forward = -Ue'*lk2(angle+0.001,E,Erat,length)*Ue;
        case 'Strain_Energy'
            k_b = lk2(angle-0.001,E,Erat,length);
            k_c = lk2(angle,E,Erat,length);
            k_f = lk2(angle+0.001,E,Erat,length);
            backward = -Ue'*k_b*Ue+2*Ue'*k_b*Ue_th - Ue_th'*k_b*Ue_th;
            center = -Ue'*k_c*Ue+2*Ue'*k_c*Ue_th - Ue_th'*k_c*Ue_th;
            forward = -Ue'*k_f*Ue+2*Ue'*k_f*Ue_th - Ue_th'*k_f*Ue_th;
        end
        der = (forward-backward)/0.002;
        dder = (forward-2*center+backward)/.001^2;
        anew = angle - der/dder;
        diff = (anew - angle)/anew;
        angle = anew;
        arec(end+1) = anew;
        if size(arec,2) > 20
            L = linspace(0,2*pi);
            for n = 1:100
                switch Opt_Var
                    case 'Compliance'
                        m(n) = Ue'*lk2(L(n),E,Erat,length)*Ue;
                    case 'Strain_Energy'
                        K1 = lk2(L(n),E,Erat,length);
                        m(n) = Ue'*K1*Ue - 2*Ue'*K1*Ue_th + Ue_th'*K1*Ue_th;
                    end
                end
                m_abs = abs(m);
                [~, index] = max(m_abs);
                angle = L(index);
                break
            end
        end
        a1 = angle;
        a2 = angle + pi/2;
        a3 = angle + pi/4;
        a4 = angle + 3*pi/4;
        switch Opt_Var
            case 'Compliance'
                SE1 = Ue'*lk2(a1,E,Erat,length)*Ue;
                SE2 = Ue'*lk2(a2,E,Erat,length)*Ue;
                SE3 = Ue'*lk2(a3,E,Erat,length)*Ue;
                SE4 = Ue'*lk2(a4,E,Erat,length)*Ue;
            case 'Strain_Energy'
                K1 = lk2(a1,E,Erat,length);
                K2 = lk2(a2,E,Erat,length);
                K3 = lk2(a3,E,Erat,length);
                K4 = lk2(a4,E,Erat,length);
                SE1 = Ue'*K1*Ue - 2*Ue'*K1*Ue_th + Ue_th'*K1*Ue_th;
                SE2 = Ue'*K2*Ue - 2*Ue'*K2*Ue_th + Ue_th'*K2*Ue_th;
                SE3 = Ue'*K3*Ue - 2*Ue'*K3*Ue_th + Ue_th'*K3*Ue_th;
                SE4 = Ue'*K4*Ue - 2*Ue'*K4*Ue_th + Ue_th'*K4*Ue_th;
            end
        end
        [~,ind] = max([SE1,SE2,SE3,SE4]);
        avec = [a1,a2,a3,a4];
        angle = avec(ind);
    end

function [strain,stress,vm]=stress1(angle,E,Erat,U,length)
% Based on the two-point Gauss Quadrature
Ey = E;
Ex = Erat*E;
nuxy = .36;
nuyx = nuxy*Ey/Ex;

varset = 1/sqrt(3)*[1 1;1 -1;-1 1;-1 -1];
KE = zeros(8,8);
strain = [0;0;0;0;0;0;0;0];

```

```

D = [Ex/(1-nuxy*nuyx) nuxy*Ey/(1-nuxy*nuyx) 0; nuxy*Ey/(1-nuxy*nuyx) Ey/(1-nuxy*nuyx) 0;
0 0 Ex/(2*(1+nuxy))];
rotation = [cos(angle)^2 sin(angle)^2 -2*sin(angle)*cos(angle); ...
sin(angle)^2 cos(angle)^2 2*sin(angle)*cos(angle);
cos(angle)*sin(angle) -cos(angle)*sin(angle) cos(angle)^2 - sin(angle)^2];
rDr = rotation*D*rotation';
for j = 1:4
    nu = varset(j,1);
    eta = varset(j,2);
B = 1/4*[-1+nu 0 1-nu 0 1+nu 0 -1-nu 0; 0 -1+eta 0 -1-eta 0 1+eta 0 1-eta; ...
-1+eta -1+nu -1-eta 1-nu 1+eta 1+nu 1-eta -1-nu];
KE = KE + B'*rDr*B*length^2/4;
strain = strain + B*U;
end
stress = D*strain;
vm = sqrt(stress(1)^2+stress(1)*stress(2)+stress(2)^2);
end

function [dcn]=check(nelx,nely,rmin,x,dc)
dcn=zeros(nely,nelx);
for i = 1:nelx
    for j = 1:nely
        sum=0.0;
        for k = max(i-floor(rmin),1):min(i+floor(rmin),nelx)
            for l = max(j-floor(rmin),1):min(j+floor(rmin),nely)
                fac = rmin-sqrt((i-k)^2+(j-l)^2);
                sum = sum+max(0,fac);
                dcn(j,i) = dcn(j,i) + max(0,fac)*x(l,k)*dc(l,k);
            end
        end
        dcn(j,i) = dcn(j,i)/(x(j,i)*sum);
    end
end

function [xnew,angle]=OC_new(nelx,nely,x,volfrac,dc,fixed_density)
move = 0.02;
max_dc = max(max(sqrt(abs(dc))));
%l1 = max_dc/1.2;
%l2 = -max_dc/1.2;

l1 = -1E11;
l2 = 1E11;
xnew = x;
damp = 0.5;
loop = 0;
while loop < 1000
    lmid = 0.5*(l2+l1);
    loop = loop + 1;
    xnew = max(0.001,max(x-move,min(1.,min(x+move,x.*sign(dc).*(abs(dc)).^damp./lmid))));
    xnew(fixed_density) = 1;
    if (sum(sum(xnew)) - volfrac*nelx*nely) > 0 %direction originally > and no *lmid
        l1 = lmid;
    else
        l2 = lmid;
    end
    if abs(sum(sum(xnew))/(nelx*nely) - volfrac) < 0.000001
        break
    end
end
end

```

The GCMMA code was based on Dr. Svanberg's code, and while a new objective function and gradient were generated, the overall structure of the code remains

unchanged. The new objective function is presented, along with the m-file of constants and the main loop, as some minor changes were made there. None of the subfunctions were altered from Dr. Svanberg's original files, so those are not included here. Note that the objective function uses finite element subfunctions, which are identical to the ones used above in the OC optimization.

```

penal = 3;
Erat = 10; % Ratio of in-line modulus to perpendicular modulus
xl = .10; % length of x-side in m
E = 1.79E9; %Young's Modulus in weakest direction
al = 7E-5; %1/C Coefficient of thermal expansion
alpharat = 1.2;
ksmall= 0.13; %W/m*K, for ABS plastic, min value
krat = 2; % Ratio of in-line conduction coefficient to perpendicular conduction
coefficient
rmin = 1.2;

clear
clc
format compact
% Initialization for topology optimization
nely = 100;
nelx = 200;
volfrac = 0.5;
flag = 0; % 0 for compliance, 1 for strain energy
record = [];
% Initialization for MMA
m = 2; % number of constraints?
n = 2*nely*nelx; % number of independent variables (densities and angles)
epsimin = 0.0000001; % maybe unused?
eeen = ones(n/2,1);
eeem = ones(m,1);
zeron = zeros(n,1);
zerom = zeros(m,1);

% Initialize independent variables
%xval = [volfrac*eeen; 2*pi*rand(n/2,1)]; % densities set to volfrac, angles randomly
chosen
%xval = [rand(n/2,1); 2*pi*rand(n/2,1)]; % densities set to volfrac, angles randomly
chosen
xval = [volfrac*eeen; pi*rand(n/2,1)]; % densities set to volfrac, angles randomly
chosen
xold1 = xval;
xold2 = xval;
xmin = [0.001*eeen; -10*pi*eeen]; % density has a lower bound of 0.001
xmax = [eeen; 10*pi*eeen]; % density has an upper bound of 1
low = xmin;
upp = xmax;
c = eeem*1e4; % 12 works, but not monotonic
d = eeem; % usually set to eeem
a0 = 1;
a = zerom;
outeriter = 0;
maxoutit = 500;
kkttol = 0;
%
%% MMA Loop
%%% If outeriter=0, the user should now calculate function values
%%% and gradients of the objective- and constraint functions at xval.

```

```

%%% The results should be put in f0val, df0dx, fval and dfdx:
if outeriter < 0.5
    [f0val,df0dx,unf,fval,dfdx] = topfunct_final(xval,nely,nelx,volfrac,flag);
    innerit=0;
    outvector1 = [outeriter innerit f0val fval'];
    outvector2 = xval';
end
%
%%% The iterations start:
kktnorm = kkttol+10;
outit = 0;
while kktnorm > kkttol && outit < maxoutit
    outit = outit+1;
    outeriter = outeriter+1;
    %%% The MMA subproblem is solved at the point xval:
    [xmma,ymma,zmma,lam,xsi,eta,mu,zet,s,low,upp] = ...
        mmasub(m,n,outeriter,xval,xmin,xmax,xold1,xold2, ...
            f0val,df0dx,fval,dfdx,low,upp,a0,a,c,d);
    %keyboard
    %%% Some vectors are updated:
    xold2 = xold1;
    xold1 = xval;
    xval = xmma;
    % round angles to within bounds
    xval(nelx*nely+1:end) = mod(xval(nelx*nely+1:end),2*pi);
    %%% The user should now calculate function values and gradients
    %%% of the objective- and constraint functions at xval.
    %%% The results should be put in f0val, df0dx, fval and dfdx.
    [f0val,df0dx,unf,fval,dfdx] = topfunct2(xval,nely,nelx,volfrac,flag);
    %%% The residual vector of the KKT conditions is calculated:
    [residu,kktnorm,residumax] = ...
        kktcheck(m,n,xmma,ymma,zmma,lam,xsi,eta,mu,zet,s, ...
            xmin,xmax,df0dx,fval,dfdx,a0,a,c,d);
    outvector1 = [outeriter innerit f0val fval'];
    outvector2 = xval';
    % Plotting
    x = reshape(xval(1:nely*nelx),nely,nelx);
    angle = reshape(xval(1+nely*nelx:end),nely,nelx);
    figure(1)
    I = imagesc([flip(x)'] x));
    colormap parula
    colorbar
    hold on
    Xlen = 1:2*nelx;
    Ylen = 1:nely;
    [Xset,Yset] = meshgrid(Xlen,Ylen);
    xvec = sin(pi/2 - angle).*x; % switched from usual because angle is measured from
y-axis
    yvec = cos(pi/2 - angle).*x; % This is because y comes first in the ordered pairs
for density
    xvec = [flip(-xvec)'] xvec;
    yvec = [flip(yvec)'] yvec;
    spacing = ceil(max(nelx,nely)/100);
    quiver(Xset(1:spacing:end,1:spacing:end),Yset(1:spacing:end,1:spacing:end)', ...
        .5*spacing*xvec(1:spacing:end,1:spacing:end)',.5*spacing*yvec(1:spacing:end,1:spacing:end
    )', 'MaxheadSize',0, 'Color',[0 0 0], 'AutoScale','off')
    quiver(Xset(1:spacing:end,1:spacing:end),Yset(1:spacing:end,1:spacing:end)', ...
        -.5*spacing*xvec(1:spacing:end,1:spacing:end)',-
        .5*spacing*yvec(1:spacing:end,1:spacing:end)', 'MaxheadSize',0, 'Color',[0 0
    0], 'AutoScale','off')

    axis equal
    axis tight
    axis([1 2*nelx 1 nely])
    title('Part Design')
    hold off
    pause(.2)

pause(0.2)

```

```

hold off
record = [record f0val];
fprintf('Outerit: %i ',outit)
fprintf('Volfrac: %f ',sum(sum(x))/(nelx*nely))
fprintf('Function Value %f\n',f0val)
figure(2)
plot(record)
pause(0.2)
end
%-----

function [f0val,df0dx,unfil,fval,dfdx] = topfunct_final(xval,nely,nelx,volfrac,flag)
% f0val is optimization function value
% df0dx is optimization function gradient
% fval is constraint function
% dfdx is constraint gradient
nx = length(xval);
eeen = ones(nx/2,1);
% Import constants
constants
le = xl/nelx; %length of one unit cell edge in meters
% Reshape the xval vector into a standard
x = reshape(xval(1:nely*nelx),nely,nelx);
angle = reshape(xval(nely*nelx+1:end),nely,nelx);
% copy/paste the finite element bit:
[T,K_ff,freedofs]=thermal_FEA(nelx,nely,x,angle,penal,ksmall,krat,le,1);
[thermal_forces, DF_DT] =
thermal_stresses(T,x,angle,nely,nelx,al,alpharat,le,E,Erat,penal);
[U,U_th,~]=mechanical_FEA(nelx,nely,x,angle,penal,E,Erat,thermal_forces,le);
if flag == 0
    lambda = zeros(1,(nelx+1)*(nely+1));
    lambda(:,freedofs) = (U'*DF_DT(:,freedofs))/K_ff;
end
% OBJECTIVE FUNCTION AND SENSITIVITY ANALYSIS
c = 0;
SE = 0;
dc = zeros(nely,nelx);
dc_a = zeros(nely,nelx);
d_SE = zeros(nely,nelx);
dSE_a = zeros(nely,nelx);
for ely = 1:nely
    for elx = 1:nelx
        n1 = (nely+1)*(elx-1)+ely;
        n2 = (nely+1)* elx +ely;
        % DOF selected for mechanical analysis
        edof = [2*n1-1;2*n1; 2*n2-1;2*n2; 2*n2+1;2*n2+2; 2*n1+1;2*n1+2];
        edof_T = [n1;n2;n2+1;n1+1];
        Ue = U(edof,1); % ccw from bottom left
        Ue_t = U_th(edof,1);
        %Ue_t = zeros(8,1);
        % DOF selected for thermal analysis
        T_i = T([n1;n2;n2+1;n1+1],1); % ccw from bottom left
        % Mechanical element created
        KE = lk(angle(ely,elx),E,Erat,le);
        KE2 = lk(angle(ely,elx) + 0.001,E,Erat,le);
        dKE_da = (KE2 - KE)/0.001;
        % Thermal element created
        KE_th = lk_th(angle(ely,elx),ksmall,krat,le);
        KE_th2 = lk_th(angle(ely,elx) + 0.001,ksmall,krat,le);
        dKE_th_da = (KE_th2 - KE_th)/.001;

        if flag == 0 % compliance
            c = c + 1/2*x(ely,elx)^penal*Ue'*KE*Ue;
            TL = thermoload(x(ely,elx),angle(ely,elx),E,Erat,al,alpharat,T_i,le,penal);
            dTL_dxi = TL*penal/x(ely,elx); % seems more accurate
            dTL_dai = (thermoload(x(ely,elx),angle(ely,elx) +
            .001,E,Erat,al,alpharat,T_i,le,penal) - TL)/.001;
            DF_Dxi = lambda(edof_T)*KE_th*T_i;
            dc(ely,elx) = -1*(penal*x(ely,elx)^(penal-1)*Ue'*KE*Ue - 2*Ue'*dTL_dxi +
            2*penal*x(ely,elx)^(penal-1)*DF_Dxi);
        end
    end
end

```

```

        dc_a(ely,elx) = -1*(x(ely,elx)^penal*Ue'*dKE_da*Ue - 2*Ue'*dTL_dai +
2*ksmall*x(ely,elx)^penal*lambda(edof_T)*dKE_th_da*T_i);
        elseif flag == 1 % strain energy
            SE = SE + 1/2*x(ely,elx)^penal*(Ue'*KE*Ue - 2*Ue'*KE*Ue_t + Ue_t'*KE*Ue_t);
            d_SE(ely,elx) = -1*(-0.5*penal*x(ely,elx)^(penal-1)*(-Ue'*KE*Ue +
2*Ue_t'*KE*Ue - Ue_t'*KE*Ue_t));
            dSE_a(ely,elx) = -1*(0.5*x(ely,elx)^penal*(Ue'*dKE_da*Ue - 2*Ue'*dKE_da*Ue_t
+ Ue_t'*dKE_da*Ue_t)); % MAYBE WRONG - CHECK
        end
    end
end

if flag == 0
    f0val = 5*c/1e4;
    dc_f = check(nelx,nely,rmin,x,dc); %mesh-independence check
    df0dx = [reshape(dc_f,nely*nelx,1);reshape(dc_a,nely*nelx,1)]*1e-4;
    unfil = [reshape(dc,nely*nelx,1);reshape(dc_a,nely*nelx,1)]*1e-4;
elseif flag == 1
    f0val = 5*SE/1e4;
    d_SE_f = check(nelx,nely,rmin,x,d_SE); %mesh-independence check
    df0dx = [reshape(d_SE_f,nely*nelx,1);reshape(dSE_a,nely*nelx,1)]*1e-4;
    unfil = [reshape(d_SE,nely*nelx,1);reshape(dSE_a,nely*nelx,1)]*1e-4;
end

% Constraint: volume fraction
fval1 = sum(xval(1:nely*nelx))/(0.5*nx*volfrac) - 1;
fval2 = 1-.2 - sum(xval(1:nely*nelx))/(0.5*nx*volfrac);
%keyboard
dfdx1 = [eeen' 0*eeen']/(0.5*nx*volfrac);
%keyboard
%-----
fval = 100*[fval1; fval2];
dfdx = 100*[dfdx1; -1*dfdx1];

```


BIBLIOGRAPHY

- [1] A. Siegel, “Automatic Programming of Numerically Controlled Machine Tools,” *Control Eng*, vol. 3, no. 10, pp. 65–70, Oct. 1956.
- [2] A. International, “ASTM F2792 -12a Standard Terminology for Additive Manufacturing Technologies.,” 2012.
- [3] T. Nomura *et al.*, *General Topology Optimization Method With Continuous and Discrete Orientation Design Using Isoparametric Projection*. International Journal for Numerical Methods in Engineering, 2014.
- [4] Molitch-Hou, Michael. :7 Issues to Look Out for in Metal 3D Printing.” Engineering.com, 2017. Accessed 20 Jun 2019 from <https://www.engineering.com/3DPrinting/3DPrintingArticles/ArticleID/15202/7-Issues-to-Look-Out-for-in-Metal-3D-Printing.aspx>
- [5] T. Wohlers, *Wohlers Report 2018*. Inc: Wohlers Associates, 2018.
- [6] CustomPart.net, “Fused Deposition Modeling (FDM),” 2019.
- [7] S.-H. Ahn, M. Montero, D. Odell, S. Roundy, and P. K. Wright, “Anisotropic material properties of fused deposition modeling ABS,” *Rapid Prototyp J*, vol. 8, no. 4, pp. 248–257, Oct. 2002.
- [8] A. Bellini and G. Selcuk, “Mechanical characterization of parts fabricated using fused deposition modeling,” *Rapid Prototyp J*, vol. 9, no. 4, pp. 252–264, 2003.
- [9] Rigid.ink, “3D Prints Warping of Curling? – Why It Happens and How to Prevent It.,” 2017.
- [10] C. Inc, “BAAM Specifications.”
- [11] O. R. N. Laboratory, “Shelby Cobra,” vol. 19, Jun. 2019.
- [12] B. Post, P. D. Lloyd, J. Lindahl, R. F. Lind, L. J. Love, and V. Kunc, *The Economics of Big Area Additive Manufacturing, Oak Ridge National Laboratory (ORNL), Oak Ridge, TN (United States)*. Manufacturing Demonstration Facility (MDF, 2016.

- [13] V. Kunc *et al.*, “Modeling of Large Scale Reinforced Polymer Additive Manufacturing,” *ANTEC Orlando Fla. March 23-25 2015 Soc. Plast. Eng.*, pp. 23–25, 2015.
- [14] B. G. Compton, B. K. Post, C. E. Duty, L. Love, and V. Kunc, “Thermal Analysis of Additive Manufacturing of Large-Scale Thermoplastic Polymer Composites,” *Addit. Manuf.*, pp. 77–86, 2017.
- [15] A. R. T. Perez, D. A. Roberson, and R. B. Wicker, “Fracture Surface Analysis of 3D-Printed Tensile Specimens of Novel ABS-Based Materials,” *J Fail Anal Prev*, vol. 14, no. 3, pp. 343–353, 2014.
- [16] H. L. Tekinalp *et al.*, “Highly oriented carbon fiber–polymer composites via additive manufacturing,” *Compos Sci Technol*, vol. 105, pp. 144–150, Dec. 2014.
- [17] V. K. L. J. Love, “The importance of carbon fiber to polymer additive manufacturing,” *J Mater Res*, vol. 29, no. 17, pp. 1893–1898, 2014.
- [18] F. Ning, W. Cong, J. Wei, S. Wang, and M. Z. Zhang, *Additive Manufacturing of CFRP Composites using Fused Deposition Modeling: Effects of Carbon Fiber Content and Length*. Charlotte, NC: in Proceedings of the ASME 2015 International Manufacturing Science and Engineering Conference, 2015.
- [19] F. van der Klift, Y. Koga, A. Todoroki, M. Ueda, Y. Hirano, and R. Matsuzaki, “3D Printing of Continuous Carbon Fibre Reinforced Thermo-Plastic (CFRTP) Tensile Test Specimens,” *Open J Compos Mater*, vol. 6, pp. 18–27, 2016.
- [20] B. Heller, *Effects of Nozzle Geometry and Extrudate Swell on Fiber Orientation in Fused Deposition Modeling Nozzle Flow*. Baylor University, 2015.
- [21] W. Zhong, F. Li, Z. Zhang, L. Song, and Z. Li, “Short fiber reinforced composites for fused deposition modeling,” *Mater Sci Eng A*, vol. 301, pp. 125–130, 2001.
- [22] O. Sigmund, “A 99 Line Topology Optimization Code Written in Matlab,” *Struct. Multidiscip. Optim.*, pp. 120–127, 2001.
- [23] K. Svanberg, “The Method of Moving Asymptotes – a New Method for Structural Optimization,” *Int. J. Numer. Methods Eng.*, pp. 359–373, 1987.
- [24] M. P. Bendsoe and O. T. Sigmund, *Topology Optimization: Theory, Methods, and Applications*. Germany: Springer-Verlag Berlin Heidelberg, 2003.
- [25] M. P. Bendsoe and N. Kikuchi, “Generating Optimal Topologies in Structural Design Using a Homogenization Method,” *Comput. Methods Appl. Mech. Eng.*, pp. 197–224, 1988.

- [26] Z. H. Zuo and Y. M. Xie, “A simple and compact Python code for complex 3D topology optimization,” *Adv Eng Softw*, vol. 85, pp. 1–11, Jul. 2015.
- [27] K. Suzuki and N. Kikuchi, “A homogenization method for shape and topology optimization,” *Comput Methods Appl Mech Eng*, vol. 93, no. 3, pp. 291–318, Dec. 1991.
- [28] M. P. Bendsøe, A. Díaz, and N. Kikuchi, “Topology and Generalized Layout Optimization of Elastic Structures,” in *Topology Design of Structures*, P. M. P. Bendsøe and P. C. A. M. Soares, Eds. Netherlands: Springer, 1993, pp. 159–205.
- [29] N. Kikuchi, S. Nishiwaki, J. S. O. Fonseca, and E. C. N. Silva, “Design optimization method for compliant mechanisms and material microstructure,” *Comput Methods Appl Mech Eng*, vol. 151, pp. 401–417, 1998.
- [30] V. Sundararajan, *Topology Optimization for Additive Manufacturing of Customized Meso-Structures using Homogenization and Parametric Smoothing Functions*. University of Texas at Austin: MS, 2010.
- [31] R. J. Yang and C. H. Chuang, “Optimal topology design using linear programming,” *Comput Struct*, vol. 52, no. 2, pp. 265–275, Jul. 1994.
- [32] V. Challis, *A Discrete Level-Set Topology Optimization Code Written in Matlab*. Structural and Multidisciplinary Optimization, 2010.
- [33] K. Liu and A. Tovar, “An efficient 3D topology optimization code written in Matlab,” *Struct Multidiscip Optim*, vol. 50, no. 6, pp. 1175–1196, Jun. 2014.
- [34] M. Bruyneel and C. Fleury, “Composite structures optimization using sequential convex programming,” *Adv Eng Softw*, vol. 33, no. 7–10, pp. 697–711, Jul. 2002.
- [35] Y. M. Xie and G. P. Steven, “A simple evolutionary procedure for structural optimization,” *Comput Struct*, vol. 49, no. 5, pp. 885–896, Dec. 1993.
- [36] Y. Tang, A. Kurtz, and Y. F. Zhao, “Bidirectional Evolutionary Structural Optimization (BESO) based design method for lattice structure to be fabricated by additive manufacturing,” *Comput-Aided Des*, vol. 69, pp. 91–101, Dec. 2015.
- [37] X. Huang, Y. Li, S. W. Zhou, and Y. M. Xie, “Topology Optimization of Compliant Mechanisms with Desired Structural Stiffness,” *Eng. Struct.*, vol. 79, pp. 13–21, 2014.
- [38] A. Nonlinear, “Programming Technique for the Optimization of Continuous Processing Systems,” *Manag. Sci.*, vol. 7, no. 4, pp. 379–392, Jul. 1961.

- [39] R. B. Haber, C. S. Jog, and M. P. Bendsøe, “A new approach to variable-topology shape design using a constraint on perimeter,” *Struct Optim*, vol. 11, no. 1–2, pp. 1–12, Feb. 1996.
- [40] M. Kočvara and J. Zowe, “*Free Material Optimization: An Overview*. 2002.
- [41] J. Alexanderson, N. Aage, C. Andreasen, and O. Sigmund, “Topology Optimization for Natural Convection Problems,” *Int. J. Numer. Methods Fluids DOI*, vol. 10, p. 1002, 2013.
- [42] J. Alexandersen, “Topology Optimization for Coupled Convection Problems,” Master’s Thesis, Masters Thesis DUT Mechanical Engineering, 2013.
- [43] D. Menge and S. Töws, *Topol. Optim. Heat Transf. Using Ex. Electron. Hous.*, 2018.
- [44] G. Vantyghem, V. Boel, M. Steeman, and W. De Corte, *Multi-Material Topology Optimization Involving Simultaneous Structural and Thermal Analyses*. Structural and Multidisciplinary Optimization, 2019.
- [45] P. Pederson and N. Pederson, “Strength Optimized Designs of Thermoelastic Structures,” *Struct. Multidiscip. Optim.*, pp. 681–691, 2010.
- [46] P. Pedersen and N. Pedersen, *Interpolation/Penalization Applied for Strength of 3D Thermoelastic Structures*. Structural and Mutidisciplinary Optimization, 2012.
- [47] D. J. Neiferd and R. V. Grandhi, *Level-Set Topology Optimization of Thermoelastic Structures – a Comparison of Compliance, Strain Energy, and Stress Objectives*. Multidisciplinary Analysis and Optimization Conference, 2018.
- [48] O. Sigmund, “Design of multiphysics actuators using topology optimization – Part I: One-material structures,” *Comput Methods Appl Mech Eng*, vol. 190, no. 49–50, pp. 6577–6604, Oct. 2001.
- [49] O. Sigmund, “Design of multiphysics actuators using topology optimization – Part II: Two-material structures,” *Comput Methods Appl Mech Eng*, vol. 190, no. 49–50, pp. 6605–6627, Oct. 2001.
- [50] J. Deaton, *Design of Thermal Structures Using Topology Optimization*. Wright State University: Dissertation for Doctor of Philosophy, 2009.
- [51] L. L. Beghini, A. Beghini, N. Katz, W. F. Baker, and G. H. Paulino, “Connecting Architecture and Engineering through Structural Topology Optimization,” *Eng Struct*, vol. 59, pp. 716–726, 2014.

- [52] J. S. Ou and N. Kikuchi, "Integrated optimal structural and vibration control design," *Struct Optim*, vol. 12, pp. 209–216, 1996.
- [53] N. Olhoff, "Optimal design of vibrating circular plates," *Int J Solids Struct*, vol. 6, no. 1, pp. 139–156, 1970.
- [54] A. R. Diaz and N. Kikuchi, "Solutions to shape and topology eigenvalue optimization problems using a homogenization method," *Int J Numer Methods Eng*, vol. 35, pp. 1487–1502, Oct. 1992.
- [55] J. Folgado, P. R. Fernandes, and H. Rodriguez, "Topology Optimization of Three-Dimensional Structures Under Contact Conditions," 2001.
- [56] T. E. Bruns and D. A. Tortorelli, "Topology optimization of non-linear elastic structures and compliant mechanisms," *Comput Methods Appl Mech Eng*, vol. 190, no. 26–27, pp. 3443–3459, Mar. 2001.
- [57] T. Buhl, C. B. W. Pedersen, and O. Sigmund, "Stiffness design of geometrically nonlinear structures using topology optimization," *Struct Multidiscip Optim*, vol. 19, pp. 93–104, 2000.
- [58] L. Wang, P. K. Basu, and J. P. Leiva, "Automobile Body Reinforcement by Finite Element Optimization," *Finite Elem Anal Des*, vol. 40, no. 8, pp. 879–893, 2004.
- [59] C. Soto and R. Yang, "Optimum Topology of Embossed Ribs in Stamped Plates," *ASME Des. Eng. Tech. Conf.*, vol. 1998, 1998.
- [60] Q. Xia and T. Shi, *Optimization of Composite Structures with Continuous Spatial Variation of Fiber Angle Through Shepard Interpolation*. Composite Structures, 2017.
- [61] J. H. Luo and H. C. Gea, *Optimal Orientation of Orthotropic Materials Using an Energy Based Method*. Structural Optimization, 1998.
- [62] T. T. Yap, "Adaptive Angle Set Method: A New Strategy for Combined Topology and Fiber Angle Optimization," Master's Thesis, Masters Thesis Delft University of Technology, 2014.
- [63] D. Jiang, R. Hoglund, and D. E. Smith, *Continuous Fiber Angle Topology Optimization for Polymer Composite Deposition Additive Manufacturing Applications*. Fibers, 2019.
- [64] E. Ulu, E. Korkmaz, K. Yay, O. B. Ozdoganlar, and L. B. Kara, "Enhancing the Structural Performance of Additively Manufactured Objects Through Build Orientation Optimization," *J Mech Des*, vol. 137, p. 11, 2015.

- [65] H. C. Cheng, N. Kikuchi, and Z. D. Ma, “An improved approach for determining the optimal orientation of orthotropic material,” *Struct Optim*, vol. 8, no. 2–3, pp. 101–112, Oct. 1994.
- [66] Z. Wu, Y. Sogabe, and Y. Arimitsu, *A Simple Method for Topology Optimization using Orthotropic Material Properties*. Ehime University, Japan: Department of Mechanical Engineering, 2001.
- [67] J. Alamo and F. da Silva, “Adapting the SIMP Model for Topology Optimization of Biomechanical Structures,” *12th Pan-Am. Congr. Appl. Mech. - PACAM XII*, 2012.
- [68] M. P. Bendsøe, J. M. Guedes, R. B. Haber, P. Pedersen, and J. E. Taylor, “An analytical model to predict optimal material properties in the context of optimal structural design,” *Trans ASME*, vol. 61, pp. 930–937, 1994.
- [69] J. Stegmann and E. Lund, “Discrete material optimization of general composite shell structures,” *Int J Numer Methods Eng*, vol. 62, no. 14, pp. 2009–2027, Apr. 2005.
- [70] R. Sørensen and E. Lund, “In-plane material filters for the discrete material optimization method,” *Struct Multidiscip Optim*, vol. 52, no. 4, pp. 645–661, Jun. 2015.
- [71] J. Haslinger, M. Kocvara, G. Leugering, and L. Stingl, “Multidisciplinary free material optimization,” *SIAM J Appl Math*, vol. 70, no. 7, pp. 2709–2728, 2010.
- [72] J.-H. Zhu, W.-H. Zhang, and L. Xia, *Topology Optimization in Aircraft and Aerospace Structures Design*. Arch Comput. Methods Eng, 2015.
- [73] R. Rezaie, M. Badrossamay, A. Ghaie, and H. Moosavi, “Topology Optimization for Fused Deposition Modeling Process,” *Procedia CIRP*, vol. 6, pp. 521–526, 2013.
- [74] R. M. Hoglund, “An Anisotropic Topology Optimization Method for Carbon Fiber-Reinforced Fused Filament Fabrication,” Master’s Thesis, Masters Thesis Baylor University, 2016.
- [75] D. Jiang, “Three Dimensional Topology Optimization with Orthotropic Material Orientation Design for Additive Manufacturing Structures,” Master’s Thesis, Masters Thesis Baylor University, 2017.
- [76] J. N. Reddy, *An Introduction to the Finite Element Method, Third Edition*. Mcgraw Hill Education, 2005.

- [77] W. Zhang, J. Yang, Y. Xu, and T. Gao, “Topology Optimization of Thermoelastic Structures: Mean Compliance Minimization or Elastic Strain Energy Minimization,” *Struct. Multidiscip. Optim.*, pp. 417–429, 2014.
- [78] B. S. Lazarov and O. Sigmund, “Filters in topology optimization based on Helmholtz-type differential equations,” *Int J Numer Methods Eng*, vol. 86, pp. 765–781, 2011.
- [79] A. Díaz and O. Sigmund, “Checkerboard Patterns in Layout Optimization,” *Struct Optim*, vol. 10, no. 1, pp. 40–45, 1995.
- [80] C. S. Jog and R. B. Haber, “Stability of finite element models for distributed-parameter optimization and topology design,” *Comput. Methods Appl. Mech. Eng.*, vol. 130, no. 3–4, pp. 203–226, 1996.
- [81] O. Sigmund and J. Petersson, “Numerical instabilities in topology optimization: A survey on procedures dealing with checkerboards, mesh-dependencies and local minima,” *Struct Optim*, vol. 16, no. 1, pp. 68–75, Aug. 1998.
- [82] O. Sigmund, *Morphology-Based Black and White Filter for Topology Optimization*. Structural and Multidisciplinary Optimization, 2007.
- [83] J. Petersson and O. Sigmund, “Slope Constrained Topology Optimization,” *Int J Numer Methods Eng*, vol. 41, no. 8, pp. 1417–1434, 1998.
- [84] J. K. Guest, J. H. Prévost, and T. Belytschko, “Achieving minimum length scale in topology optimization using nodal design variables and projection functions,” *Int J Numer Methods Eng*, vol. 61, no. 2, pp. 238–254, Sep. 2004.
- [85] L. Ambrosio and G. Buttazzo, “An Optimal Design Problem with Perimeter Penalization,” *G Calc Var*, vol. 1, no. 55, p. 1993, 1993.
- [86] F. Niu, S. Xu, and G. Cheng, “A general formulation of structural topology optimization for maximizing structural stiffness,” *Struct Multidisc Optim*, vol. 43, pp. 561–572, 2011.
- [87] Jones, Robert M., *Mechanics of Composite Materials*, 2nd ed. Ann Arbor, MI: Taylor and Francis.
- [88] P. Dechaumphai and E. Thornton, *Enhanced Thermal-Structural Analysis by Integrated Finite Elements*. Flight Dynamics Laboratory, 1984.